

Observation of Quantum Jumps in Superconducting Artificial Atoms with a Josephson Parametric Amplifier



Raffael Rabl

September 2018

Supervised by Prof. Dr. Gerhard Kirchmair
Institute of Experimental Physics
University of Innsbruck
Austria

Abstract

A two-level quantum system coupled to a thermal bath will occasionally exhibit abrupt transitions between ground and excited state. This thesis describes, how these quantum jumps can be directly observed in a superconducting artificial atom coupled to a superconducting microwave cavity. The cavity provides protection against environmental sources of decoherence. In the regime of strong dispersive coupling, the cavity also serves as a channel for high fidelity readout. Continuous probing of the cavity, allows to monitor the quantum state of the superconducting artificial atom. The measurement can be expected to be QND (quantum nondemolition) in the sense that it projects the state of the superconducting atom into the eigenstate corresponding to the measurement outcome and the system is not disturbed by the measurement. With the help of a Josephson Parametric Amplifier (JPC), a fast ultralow-noise parametric amplifier, measurement rates exceeding the internal transition rates have been achieved in this project and the quantum jumps are clearly resolved in the measured traces. This thesis offers a comprehensive introduction to the JPC, including various performance test measurements and a detailed guide about operating the amplifier. An increase in the signal-to-noise ratio of the total measurement chain of up to 12 dB at a JPC gain between 15dB and 20dB has been observed. In this setup, a 1% ground state detection fidelity was achieved at a readout power of 6 resonator photons, an integration time of $t_{avg} = 640$ ns and a low JPC gain of $G_{JPC} = 15$ dB. An even higher readout fidelity can be achieved with higher JPC gains, accepting a certain amount of amplifier saturation and resulting squeezing of the measurement signal. Probing the cavity at a slightly different frequency allows to distinguish three different results, namely the superconducting atom being in the ground, excited or any higher state. The temperature of the superconducting atom derived from the population distribution is roughly 80 mK and appears to be independent of the probe power. At probe powers above 5 resonator photons, non thermal population distributions have been observed, indicating a breakdown of the measurement's 'QNDness' for higher probe powers. This assumption is further supported by the observed abrupt drop in the excited state lifetime T_1 at a probe power of approximately 20 photons. At low probe powers, a Purcell-limited lifetime of $T_1 \approx 16 \mu\text{s}$ has been observed.

Acknowledgements

I would like to thank my advisor Gerhard Kirchmair for giving me the opportunity to carry out this thesis and the excellent supervision during the whole time. One can always count on Gerhard dropping by your office at the end of a long day and grabbing the closest empty chair, ready for a lengthy discussion. He has the ability to explain complex topics in simple terms, inspiring his students and team members with his contagious enthusiasm. Thanks to Oscar Gargiulo for introducing me to the world of qubits and cavities and Christian Schneider for putting my questions above his own work at any time. Fruitful discussions as well as good times at the soccer field and evening group beer events with Stefan Oleschko, David Zöpfl and Max Zanner were highly appreciated. Mathieu Juan was fantastically helpful, sharing his wisdom and experience regarding both physical and climbing problems. Thanks to Phani Muppalla for introducing me to the lab in my first week, I will always remember it. I want to thank Aleksei Sharafiev for the shared adventures, starting off with an simple question and ending up hours later with a blackboard full of equations and sketches. I am grateful to my amazing family, for they have been and always will be supporting and encouraging me in all my decisions. My gratitude goes to Magda Bodziony for always being at my side and enjoying the ups and downs of my years of study with me. Last but not least, I want to thank my fellow students Georg Gruber, Paul Heidler and Lukas Kirchner for helping me grow, not only as a physicist, but also as a man.

Contents

1	Introduction	1
2	Concepts	3
2.1	Cavity QED	3
2.1.1	Short History	3
2.1.2	Jaynes-Cummings-Model	4
2.2	Quantum Circuits	8
2.2.1	The LC Resonator	8
2.2.2	Josephson Junctions	10
2.2.3	Transmon - The Artificial Atom	12
2.3	Cavity QED with Quantum Circuits	13
2.3.1	Rectangular 3D Microwave Cavities	14
2.3.2	Transmon Coupled to a 3D Microwave Cavity	20
2.3.3	Dispersive Readout of a Three-level Transmon	24
2.4	Summary	25
3	Characterising the System	26
3.1	Cavity Spectroscopy	26
3.1.1	Entering the Quantum World: From High to Low Power	27
3.1.2	Driving the Transmon	29
3.2	Summary of System Parameters	33
4	Cranking up the Contrast: The Josephson Parametric Converter	34
4.1	Overview	34
4.2	Operational Principle	35
4.2.1	The Josephson Ring Modulator	35
4.2.2	Scattering Matrix and Added Noise	41
4.3	Specifications	46
4.4	Testing the JPC SN004	47
4.4.1	Tunable Range	48
4.4.2	Gain vs. Pump Power	49
4.4.3	Gain vs. Pump Frequency	50
4.4.4	Gain vs. Signal Power	51
4.4.5	SNR Improvement	52
4.5	Tuning Procedure	55
4.5.1	In Short	55

4.5.2	Step 1: Setting the Bias Current	56
4.5.3	Step 2: The Pump	58
5	Observing Quantum Jumps	61
5.1	Overview	61
5.2	Experimental Setup	63
5.3	Heterodyne Detection	65
5.3.1	Analogue Down Conversion	66
5.3.2	Digital IQ Demodulation	67
5.4	Probe Power Calibration	69
5.5	First Measurements	71
5.6	Analysing IQ-data	73
5.6.1	2D Histograms	73
5.6.2	Gaussian Fits	73
5.6.3	Temperature	76
5.7	Improving the Contrast	78
5.7.1	Readout Power Sweep	79
5.7.2	JPC Gain Sweep	80
5.7.3	Readout Time Sweep	82
5.7.4	Summary	83
5.8	Quantum Jumps	85
5.8.1	Jump Traces	85
5.8.2	Qubit Lifetime Estimation	87
5.9	Summary	89
6	Conclusion & Outlook	90
Appendix A	Additional Plots	92
A.1	Logarithmic projected histograms	92
A.2	Non thermal transmon population at high readout powers	92
A.3	Reject counts for T_1 power sweep	92
A.4	Ground state lifetimes vs. power	93
A.5	Resolving four states in the IQ plane	93
A.6	Linear and logarithmic plot of squeezed data	94
A.7	JPC SN010 Fluxmaps	97
A.8	Flip book full image	97
Appendix B	JPC Pictures	99

Nomenclature

Abbreviations

cavity QED	Cavity quantum electrodynamics
circuit QED	Circuit quantum electrodynamics
HEMT	High electron mobility transistor
JPC	Josephson Parametric Converter
JRM	Josephson ring modulator
NVR	Noise visibility ratio
QED	Quantum electrodynamics
QND	Quantum nondemolition (measurement)
Qubit	Quantum bit
RWA	Rotating wave approximation
VNA	Vector network analyser
ADC	Analogue to digital converter
FWHM	Full width (at) half maximum
HO	Harmonic oscillator
IF	Intermediate frequency

Circuit QED

$ g\rangle$	Transmon ground state
$ e\rangle$	Transmon excited state
$ f\rangle$	Transmon second excited state
$\omega_{01}/(2\pi)$	Isolated qubit transition frequency
$\omega_{ge}/(2\pi)$	Transmon $ g\rangle \leftrightarrow e\rangle$ transition frequency (qubit frequency)
$\omega_{ef}/(2\pi)$	Transmon $ e\rangle \leftrightarrow f\rangle$ transition frequency

$\omega_r/(2\pi)$	Isolated cavity frequency
$\omega_r^g/(2\pi)$	Cavity frequency when transmon in $ g\rangle$
$\omega_r^e/(2\pi)$	Cavity frequency when transmon in $ e\rangle$
$\omega_r^f/(2\pi)$	Cavity frequency when transmon in $ f\rangle$
$\Delta/(2\pi)$	Detuning between cavity and transmon $ g\rangle \leftrightarrow e\rangle$ transition
$\alpha/(2\pi)$	Anharmonicity
$\chi_e/(2\pi)$	Excited state dispersive shift
$\chi_f/(2\pi)$	Second excited state dispersive shift
$\gamma/(2\pi)$	Qubit linewidth (measured FWHM)
$\gamma_\phi/(2\pi)$	Pure qubit dephasing
$\gamma_1/(2\pi)$	Qubit decay rate
$\gamma_P/(2\pi)$	Purcell limit
T_1	Qubit decay time
T_2	Qubit dephasing time
a	Annihilation ladder operator (HO)
a^\dagger	Creation ladder operator (HO)
σ^+	Qubit excitation operator
σ^-	Qubit deexcitation operator
$g/(2\pi)$	Coupling strength dipole interaction
H_{JC}	Jaynes-Cummings Hamiltonian
$H_{\text{Disp}}^{3\text{lv}}$	Three level transmon-cavity Hamiltonian in the dispersive limit

Quantum circuits

Φ	Generalized (branch) flux
Φ_{ext}	External magnetic flux

ϕ	Node flux
$\tilde{\phi}$	Superconducting phase difference
φ	Reduced (branch) flux
Q	Generalized charge
I	Current
U	Voltage
C	Capacitance
L	Inductance

Resonators

$\kappa/(2\pi)$	Cavity decay rate
f_{vna}	VNA probe frequency
Q_c	Coupling quality factor
Q_{int}	Internal quality factor
Q_l	Loaded quality factor
S_{11}	Scattering parameter reflection
S_{21}	Scattering parameter transmission

Constants

\hbar	Reduced Planck constant
Φ_0	Reduced flux quantum $\hbar/2e$
c	Speed of light
e	Electron charge
k_B	Boltzmann constant

JPC

ω_a	JPC signal mode frequency
------------	---------------------------

ω_b	JPC idler mode frequency
ω_c	JPC pump mode frequency
ω_i	JPC idler input frequency
ω_p	JPC pump input frequency
ω_s	JPC signal input frequency
BW	-3 dB bandwidth
G_{JPC}	JPC gain
X	JPC signal mode
Y	JPC idler mode
Z	JPC pump mode

IQ measurements

$\text{ref}_0(t)$	Reference at IF frequency
$\text{ref}_{90}(t)$	90° phase shifted reference at IF frequency
$\text{sig}(t)$	Signal at IF frequency
f_2	Two-state probe frequency
f_3	Three-state probe frequency
I	In-phase quadrature
Q	Out-of-phase quadrature
n	Readout power in terms of resonator photons
t_{avg}	IQ integration time
p_{mis}	Miscount probability

1 Introduction

Superconducting circuits are a promising platform for both quantum computation [1] and simulation [2]. Unlike natural quantum systems, such as electrons, atoms, ions or photons, superconducting qubits are man-made and their intrinsic properties can be varied across a wide range during fabrication. Thus, they are commonly referred to as artificial atoms. Superconducting qubits can be coupled to resonant circuits as well as measurement and control circuitry in a straightforward way. Typical transition frequencies are in the regime of microwaves, with corresponding wavelengths on the order of centimetres. Well developed control hardware is available from telecommunication industries, in that wavelength range. The first superconducting qubit was realized in 1999 [3]. Since then, various designs with improved stability have been developed. Coherence times of $100 \mu\text{s}$ have been demonstrated in a transmon inside a high Q 3D cavity resonator [4]. More than 3000 single and 200 two-qubit gates can be performed in that timespan [5]. Strong coupling between resonators and superconducting qubits is achieved regularly in both 3D and on-chip architectures [6][7]. Resonators not only provide protection against outside noise sources, they also provide a channel to measure the quantum state of the artificial atom. In the dispersive limit of the interaction, the qubit state can be determined by probing the resonator. Low power probe signals are used in order to minimize disturbance of the system, allowing for QND measurements of the qubit. The noise added by commercial cryogenic microwave amplifiers is considerably larger than the low power signal coming back from the resonator, resulting in a low single shot readout fidelity. Repeated measurements are necessary to resolve the state of the qubit. With the recent advance of quantum limited microwave amplifiers, fast single shot readout has become feasible [8][9][10]. The improve in signal-to-noise ratio allows direct observation of quantum jumps in continuous measurements [11].

The goal of this thesis project is the implementation of a continuous qubit readout scheme with the help of a Josephson Parametric Converter (JPC). This ultra-low noise amplifier greatly improves the SNR (signal to noise ratio) of the measurement chain. Measurement rates faster than the qubit's internal transition rates are feasible, allowing to resolve the qubit's quantum jumps in time. This thesis is organised in four main parts. Section 2 covers the fundamental concepts that are helpful for the understanding of the subjects discussed in this paper. After introducing the basic building blocks of circuit QED, the treatment of a superconducting qubit coupled to a 3D microwave cavity is outlined. The coupled system is described with the methods of cavity QED. Section 3 presents experimental methods and results of the coupled cavity-qubit system and a summary of the key system parameters.

The operational principle of the JPC is discussed in sec. 4. Besides a comprehensive analysis of the amplifier performance, the JPC tuning procedure is elaborated in detail. Finally, sec. 5 presents the results of the continuous dispersive readout scheme. After a description of the experimental setup and the methods of IQ demodulation, the first successful measurements resolving two respectively three states of the superconducting artificial atom are shown. Various measures for the contrast and measurement quality are derived from the distribution of the data in the IQ plane. The optimal working point is determined by varying experimental parameters such as integration time, probe power and JPC gain. Examples of quantum jump traces are presented for different experimental configurations. The qubit relaxation time is deduced from the temporal distribution of the quantum jump events and compared to the result of an independent experiment based on a pulsed measurement scheme.

2 Concepts

This introductory chapter presents the key concepts, that the reader might find insightful when reading this thesis. Section 2.1 provides a short introduction to the field of cavity quantum electrodynamics (**cavity QED**), followed by a recapitulation of the textbook results of the Jaynes-Cummings-model. The basic building blocks of circuit QED are discussed in sec. 2.2. The simple example of an electronic LC circuit is used to develop the methods of circuit quantisation, before introducing the superstar of this field - the Josephson junction. This element provides a highly non-linear response, while causing almost no dissipation, allowing for the design of remarkable quantum circuits. Most notably, Josephson junctions can be used to construct artificial atoms - quantum systems whose intrinsic parameters are controllable over a wide range during the fabrication process. Finally, sec. 2.3 relates, how quantum circuits can be used to realize a strongly coupled cavity QED system. With the beforehand introduced methods, a single mode of a 3D rectangular microwave resonator can be described as a quantized electronic LC oscillator. A highly stable and noise insensitive design for a superconducting artificial atom is introduced - the transmon. The cavity mode and the transmon exhibit a strong dipole coupling. This thesis is focused on the strong dispersive limit of this interaction, and how it can be exploited to realise a quantum non-demolition (**QND**) readout scheme of the transmon's quantum state.

2.1 Cavity QED

2.1.1 Short History

The theory of quantum electrodynamics (**QED**) describes the interaction between matter and light. Matter is comprised by atoms whereas the basic excitations of the electromagnetic field are called photons. The quantized nature of both atoms and the field gives rise to remarkable phenomena, that deviate strongly from the predictions of classical electrodynamics. Prominent results of QED are the electronic structure of atoms and molecules, the radiation spectrum of a body due to its temperature and the spontaneous emission of a photon by an atom.

The interaction between an atom and an electromagnetic field confined inside a cavity is the topic of **cavity QED**. The cavity simplifies the dynamics of the system by reducing the degrees of freedom and provides protection against the noise of the outside environment.

Probing the cavity with an external electromagnetic field offers a channel for control and readout.

Early theoretical considerations proposed an increased spontaneous emission rate of an atom coupled to a resonant mode, as stated by Purcell in 1946 [12]. Conversely, coupling to a far detuned mode was expected to inhibit the spontaneous decay and increase the lifetime of the atom (Kleppner 1981 [13]). Cavity QED was first tested experimentally in the early 1980s by Serge Haroche and his team at the Ecole Normale Supérieure in Paris. Purcell's and Kleppner's predictions were quickly confirmed [14] and the group started to conduct more sophisticated experiments with Rydberg atoms travelling through a microwave cavity. Observing the atoms after traversing allowed them to infer the state of the cavity light field, with a precision high enough to determine the number of cavity photons [15]. This approach meets the criteria of a quantum nondemolition (**QND**) measurement - the cavity field is preserved after the measurement. Since that time, cavity QED is a growing field of research with the preliminary peak of Haroche and Weinstein receiving the Nobel price for their work in 2012.

2.1.2 Jaynes-Cummings-Model

This model describes the interaction between a two-level-system with a single mode of the electromagnetic field. Fig. 1 shows a sketch of the coupled system. The atom is enclosed by the cavity, which defines the shape and the frequency of the field mode.

An isolated atom with only ground $|g\rangle$ and excited state $|e\rangle$ is described by the Hamiltonian

$$H_{\text{a}} = \frac{\hbar\omega_a}{2}\sigma_z. \quad (1)$$

The projection operator reads $\sigma_z = |g\rangle\langle g| + |e\rangle\langle e|$ and $\hbar\omega_a$ denotes the energy difference between the states. Such a two-level-system can be used for storing or processing of quantum information. It is then referred to as a quantum bit (**qubit**). A single mode of the electromagnetic field behaves like a harmonic oscillator

$$H_{\text{field}} = \hbar\omega_r a^\dagger a \quad (2)$$

with the photon energy $\hbar\omega_r$ and the creation and annihilation operators a^\dagger and a . A linear dipole interaction between these systems is modelled by

$$H_{\text{int}} = \hbar g (a^\dagger + a) (\sigma^- + \sigma^+), \quad (3)$$

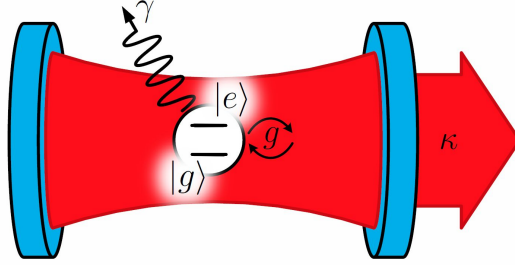


Figure 1: Cavity QED building blocks. An atom with two levels $|g\rangle$ and $|e\rangle$ is coupled to a single field mode inside a cavity. The coupling constant g describes the strength of the dipole interaction. The decay rates γ and κ model the energy loss of the atom and the cavity respectively. Fig. adapted with permission from Stefan Oleschko.

where $\sigma^- = |g\rangle\langle e|$ and $\sigma^+ = |e\rangle\langle g|$ describe transitions of the two-level-system. The strength of the interaction is specified by the coupling constant g . It depends on the dipole moment of the atomic transition and the orientation and shape of the field mode. A thorough discussion of this interaction is given in [16]. The term H_{int} can be simplified using an unitary transformation and performing the rotating wave approximation (**RWA**) following [17]. This leads to the famous Jaynes-Cummings Hamiltonian

$$H_{\text{JC}} = \hbar\omega_r a^\dagger a + \frac{\hbar\omega_a}{2} \sigma_z + \hbar g (a^\dagger \sigma^- + a \sigma^+) \quad (4)$$

for the coupled system. Intuitively, this interaction corresponds to an excitation transfer between the cavity mode and the atom. The behaviour of the system is governed by the detuning $\Delta = \omega_r - \omega_a$ between atom and cavity mode and the ratio Δ/g . The diagonalization of H_{JC} yields an interesting result. For a fixed number of excitations n , the distribution of the photons between atom and cavity is not definite. Instead, one excitation is sort of ‘shared’ between the atom and the field, forming the so called ‘dressed states’. The resonant case $\Delta = 0$ and the dispersive limit $\Delta > g$ are discussed below. Fig. 2 shows the level scheme for both cases.

Resonant JC-model $\Delta = 0$

On resonance $\Delta = 0$, the dressed states take the form

$$|n, \pm\rangle = \frac{1}{\sqrt{2}} (|g, n\rangle \pm |e, n-1\rangle) \quad (5)$$

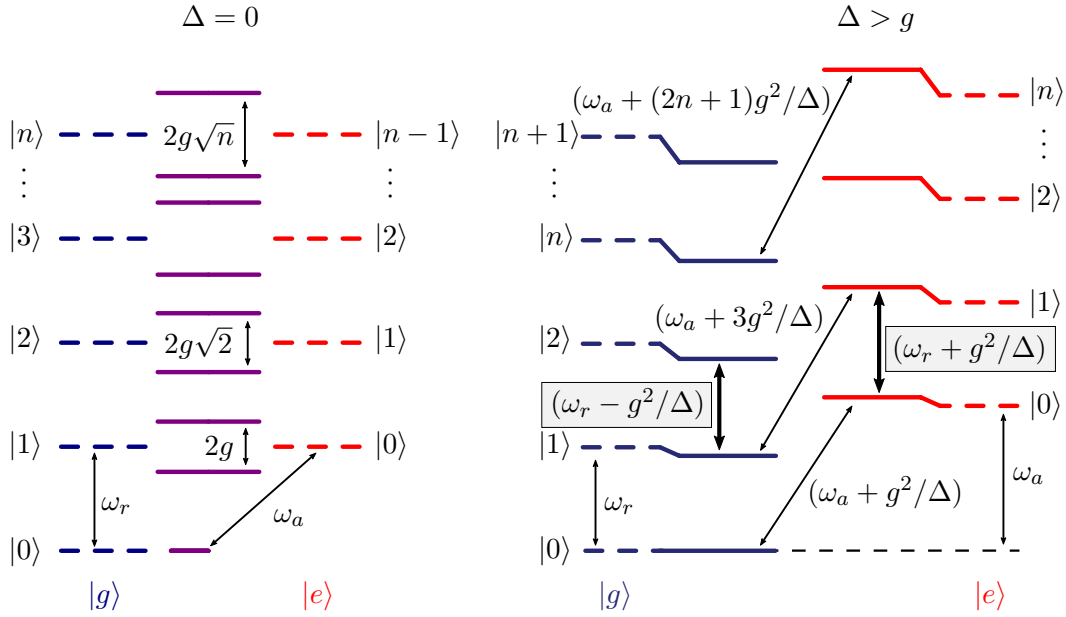


Figure 2: Energy levels of the Jaynes-Cummings Hamiltonian. **Left:** Resonant case $\Delta = \omega_r - \omega_a = 0$. The degeneracy of the uncoupled states $|g, n+1\rangle$ (drawn in blue) and $|e, n\rangle$ (red) are lifted by the interaction (purple). The splitting between the dressed states $|n, +\rangle$ and $|n, -\rangle$ grows with \sqrt{n} . **Right:** Dispersive limit $\Delta > g$. The dressed states closely resemble the qubit states and contain only a small photonic component. A special feature of the dispersive interaction is the dependence of the cavity resonance frequency on the state of the qubit (grey boxes). This allows to dispersively measure the quantum state of the qubit by probing the cavity. The relevant cavity transitions are highlighted with bold black arrows. Figure adapted from [18].

and the respective eigenenergies are

$$E_{n,\pm} = \hbar\omega_r \left(n + \frac{1}{2} \right) \pm \hbar g \sqrt{n}. \quad (6)$$

The level scheme of the resonant dressed states is sketched in the left panel of fig. 2. The splitting between two dressed states with the same number of excitations $|n, +\rangle$ and $|n, -\rangle$ is

$$\Delta E_n = 2g\sqrt{n}. \quad (7)$$

Calculating the time evolution of an initial state with fixed number of excitations in the mode and the atom e.g. $|e, 0\rangle$ (an eigenstate of the isolated atom and cavity, but not of the coupled system), reveals that the system undergoes coherent rabi oscillations between $|e, 0\rangle$ and $|g, 1\rangle$ [16].

Dispersive limit $\Delta > g$

In the dispersive limit, the Jaynes-Cummings Hamiltonian can be approximated by [19]

$$H_{\text{JC}}^{\text{Disp}} = \hbar\omega_r a^\dagger a + \frac{\hbar\omega_a}{2} \sigma_z + \frac{\hbar g^2}{\Delta} a^\dagger a \sigma_z. \quad (8)$$

This is discussed more thoroughly in sec. 2.3.2 at the example of a microwave cavity coupled to a superconducting artificial atom. In contrast to the resonant case, the dressed states $|\pm\rangle$ do not consist of an equal superposition of $|g, n\rangle$ and $|e, n-1\rangle$ in the dispersive limit of the interaction. Instead, the dressed states closely resemble the qubit states and contain only a small photonic component [19]

$$\begin{aligned} |n, -\rangle &= |g, n\rangle - \frac{g\sqrt{n}}{\Delta} |e, n-1\rangle \\ |n, +\rangle &= \frac{g\sqrt{n}}{\Delta} |g, n\rangle + |e, n-1\rangle, \end{aligned} \quad (9)$$

assuming low excitation numbers $n < n_{\text{crit}} = \Delta^2/(4g^2)$. In the same limit, the eigenenergies of the dressed states can be approximated by [18]

$$E_{n,\pm}^{\text{Disp}} \approx \hbar\omega_r \left(n + \frac{1}{2} \right) \pm \hbar\Delta + \hbar n \frac{g^2}{\Delta}. \quad (10)$$

The energy level scheme of the dispersive coupling regime is shown in the right panel of fig. 2. In this thesis, I am focussing on a special feature of the dispersive interaction. Depending on the state of the qubit, the resonance frequency of the cavity mode is either $\omega_r - g^2/\Delta$ or $\omega_r + g^2/\Delta$ (grey highlight boxes in fig. 2). Therefore, the quantum state of the qubit can be determined simply by measuring the resonance frequency of the cavity. This method is usually referred to as **dispersive readout**. In order to resolve the qubit dependent shift of the cavity frequency, the dispersive shift

$$\chi = 2g^2/\Delta \quad (11)$$

has to be larger than the linewidths of both cavity and qubit.

One has to keep in mind, that any real system will never be entirely isolated. Real (open) systems are subjected to various sources of decoherence and energy exchange. Possible loss mechanisms for the resonator mode are dissipation in the cavity walls or coupling to modes outside of the cavity. The atom can decay radiatively into other modes or via coupling to the substrate that keeps it in place (in case of an superconducting artificial



atom). However, this inevitable loss of energy can be taken into account by introducing the decay rates κ and γ for cavity and atom. In well isolated systems, these parameters can be estimated by modelling the coupling to the outside world. For the most part however, they are phenomenological figures that are determined experimentally. The loss rates have a strong influence on the coherent behaviour described by the Jaynes-Cummings model. If one of the loss rates exceeds the coupling strength g the coherent Rabi oscillations are quickly suppressed as the energy decays out of the system. Due to the small photonic component of the dressed qubit states in the dispersive regime, the excited qubit state can also decay via emitting a photon from the cavity [18]. This decay channel inherited from the coupling limits the qubit lifetime, see *Purcell-limit* in sec. 2.3.2.

2.2 Quantum Circuits

This section gives an introduction to the field of superconducting quantum circuits. A circuit can be described by defining the conjugate variables flux Φ and charge Q for each network node. In a mechanical system of coupled mass points, the analogous variables would be the position and the momentum. These ideas are illustrated by the example of a quantised electronic LC resonator in sec. 2.2.1. Replacing the inductance in an LC circuit by a Josephson junction (sec. 2.2.2) alters the potential landscape. In the resulting anharmonic potential, the degeneracy of the transitions between the individual levels is lifted. Controlling the participation ratio of capacitively and inductively stored energy via gate and shunt capacitances allows the design of a noise insensitive and stable artificial atom - the transmon (sec. 2.2.3).

2.2.1 The LC Resonator

The quantization of a superconducting circuit follows a well trodden path. First of all, the circuit's degrees of freedom are identified. Definition of the corresponding generalized coordinates and their conjugate momenta allows the denotation of the Hamilton function. The quantization is done by moving from coordinates to operators and imposing a commutation relation. A thorough description of the formalism is given in [20].

The idea is outlined here with the simplest possible example - the resonant LC circuit. It consists of a capacitor C and an inductor L which are connected on both ends, as sketched

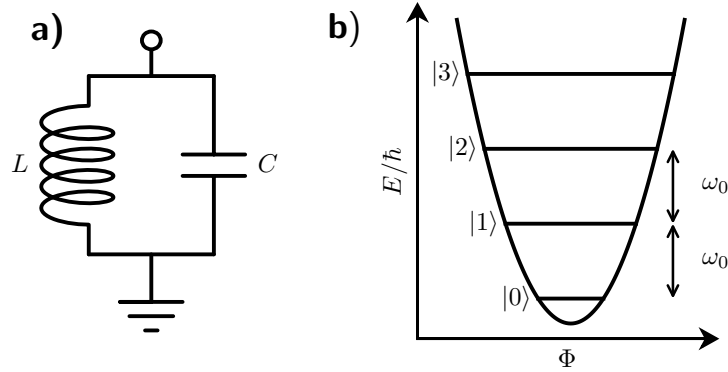


Figure 3: **(a)** Circuit diagram of an electrical LC-resonator. Quantisation of the system results in a quantum harmonic oscillator **(b)** with frequency ω_0 . The eigenstates are the Fock-states $|n\rangle$ with definite photon number n and the energy difference between two neighbouring levels is always $\hbar\omega_0$.

in fig. 3. The relations between current I and voltage U in these elements read

$$I = C\dot{U} \quad \text{and} \quad U = L\dot{I} \quad (12)$$

for capacitor and inductor respectively. Energy is either stored in the electric field of the capacitor $E_C = CU^2/2$ or the magnetic field of the inductor $E_L = LI^2/2$. Classically, the system's energy periodically oscillates between those elements with resonance frequency $\omega_0 = 1/\sqrt{LC}$. In analogy to the position of a one-dimensional pendulum, the system has only one degree of freedom. The conventional choice for a position-like coordinate in a superconducting circuit is the so-called node flux. In this example, it coincides with the magnetic flux in the inductor $\Phi = LI$. The charge in the capacitor $Q = CU$ plays the role of the conjugate momentum. The quantization is brought to completion by moving from continuous variables to operators

$$\begin{aligned} \Phi &\rightarrow \hat{\Phi} \\ Q &\rightarrow \hat{Q} \end{aligned}$$

and imposing the usual commutation relation

$$[\hat{\Phi}, \hat{Q}] = i\hbar. \quad (13)$$

Please note, that the hats over operators are omitted from here on. Rewriting the observ-



ables Φ and Q in terms of the harmonic ladder operators

$$\Phi = i\sqrt{\frac{\hbar L\omega_0}{2}}(a - a^\dagger) \quad \text{and} \quad Q = i\sqrt{\frac{\hbar C\omega_0}{2}}(a + a^\dagger), \quad (14)$$

satisfying $[a, a^\dagger] = 1$, allows the Hamiltonian to be written as

$$H_{\text{LC}} = \frac{\Phi^2}{2L} + \frac{Q^2}{2C} = \hbar\omega_0 \left(a^\dagger a + \frac{1}{2} \right). \quad (15)$$

This result is simply a quantum harmonic oscillator with frequency ω_0 . Fig. 3 shows the energy landscape of the system. With its equidistant level-spacing the harmonic oscillator is the most 'classical' quantum system and the expectation values of the observables Φ and Q behave just like their classical counterparts. The eigenstates of H_{LC} are the Fock states $|n\rangle$ with definite photon number $n = \langle a^\dagger a \rangle$. The following sections introduce the Josephson junction and show, how its nonlinearity allows the design of artificial quantum systems with individually addressable energy levels.

2.2.2 Josephson Junctions

In a conductive metal, the charge is transported by electrons. Each of them carries the elementary charge e . During the transition to the superconducting phase, the electrons pairwise condense into bosonic cooper pairs of charge $2e$. They are highly phase-correlated and can be collectively described by a single wave function

$$\Psi(r, t) = \sqrt{n(r, t)} e^{i\phi(r, t)}. \quad (16)$$

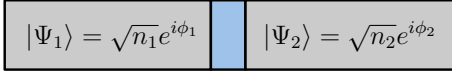
Here $n(r, t)$ denotes the number of condensed cooper pairs and ϕ is the so-called order-parameter of the system [21].

Two superconductors separated by a layer of insulator are called a Josephson junction. Fig. 4 shows an illustration of a such an SIS-element. Its remarkable properties were predicted by Josephson in 1962 [22]. He discovered, that the system's behaviour is solely governed by the difference between the phases of the superconducting wave functions on each side of the insulator

$$\tilde{\phi} = \phi_2 - \phi_1. \quad (17)$$

The generalized flux

$$\Phi = \Phi_0 \tilde{\phi} \quad (18)$$



$$|\Psi_1\rangle = \sqrt{n_1}e^{i\phi_1} \quad |\Psi_2\rangle = \sqrt{n_2}e^{i\phi_2}$$

Figure 4: Sketch of a Josephson junction. A superconductor (grey) is separated by a thin insulator (blue). The Cooper-pairs in each of the two parts of the superconductor are collectively described by the wavefunctions $|\Psi_1\rangle$ and $|\Psi_2\rangle$. The macroscopic behaviour is governed by the phase difference $\tilde{\phi} = \phi_2 - \phi_1$.

is defined by renormalizing the phase difference $\tilde{\phi}$ with the reduced magnetic flux quantum $\Phi_0 = \hbar/(2e)$. The Josephson-equations describe the voltage across

$$U(t) = \dot{\Phi}(t) \quad (19)$$

and the current through a junction

$$I(t) = I_c \sin\left(\frac{\Phi(t)}{\Phi_0}\right). \quad (20)$$

The scaling in these relations is given by Φ_0 and the critical current I_c , which depends on the material and the geometry of the junction.

There are several ways to explore the nonlinear current-voltage-relation of a Josephson junction. For example, application of a constant voltage U_0 results in a linearly increasing phase (eq. 19). According to eq. 20, an oscillating current will flow across the junction with a frequency depending on U_0 . This is the so-called *DC-Josephson-Effect*. Today's most accurate voltage standards are based on this intrinsic connection between voltage and frequency in a Josephson junction [23].

Combination of eq. 19 and the time derivative of eq. 20 reads

$$U(t) = \frac{\Phi_0}{I_c \cos(\Phi(t)/\Phi_0)} \dot{\Phi}(t). \quad (21)$$

This resembles the constitutive equation of an inductive element $U = L\dot{I}$ with the nonlinear Josephson inductance

$$L_J(\Phi) = \frac{\Phi_0}{I_c \cos(\Phi/\Phi_0)}. \quad (22)$$

To think of a Josephson junction as a nonlinear inductor gives a good intuition about many of its applications.

In addition to the Josephson inductance, the capacitance C_J formed by the surfaces of the superconductor has to be taken into account. Fig. 5 shows the electronic symbol



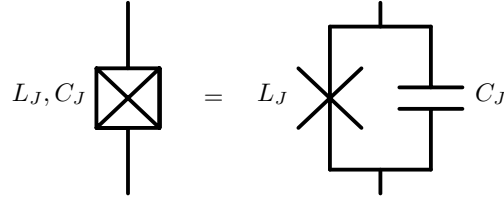


Figure 5: Electronic symbol of a Josephson junction. The capacitance C_J and the nonlinear inductance $L_J = L_J(\Phi)$ are combined in a single symbol.

of a Josephson-junction. On first glance, the model circuit resembles the LC-resonator, discussed in the previous section. As before, the energy stored in the capacitor depends linearly on the charge difference. However, the nonlinear Josephson inductance causes a fundamentally different behaviour. The inductive energy varies periodically with the flux Φ . The relative ratio of these energy contributions is the key to the design of a stable artificial atom, as is shown in the following section.

2.2.3 Transmon - The Artificial Atom

A dissipationless Josephson junction can be modelled as the nonlinear Josephson inductance L_J in parallel with the capacitance C_J . The inductive and the capacitive energy are captured in E_J and E_C respectively, the exact definitions are given in [24]. These energy contributions can be controlled by adding a shunt capacitance C_S in parallel to the junction and a gate capacitance C_G . The circuit diagram is shown in fig. 6. The nonlinear inductance modifies the parabolic potential of a linear LC-oscillator, resulting in a cosine-shaped potential. The degeneracy of the transitions is lifted and the energy levels become individually addressable. This allows the definition of a quantum bit (**qubit**), by restricting the space of states to the lowest two levels $\{|g\rangle, |e\rangle\}$. Unwanted transitions out of the qubit subspace can be modelled by taking into account the third level $|f\rangle$. The Hamiltonian of an isolated three-level transmon reads

$$H_{\text{transmon}} = \hbar\omega_0 |g\rangle \langle g| + \hbar\omega_1 |e\rangle \langle e| + \hbar\omega_2 |f\rangle \langle f|. \quad (23)$$

The transition frequencies for $|g\rangle \leftrightarrow |e\rangle$ and $|e\rangle \leftrightarrow |f\rangle$ are

$$\omega_{01} = \omega_1 - \omega_0 \quad \text{and} \quad \omega_{12} = \omega_2 - \omega_1. \quad (24)$$

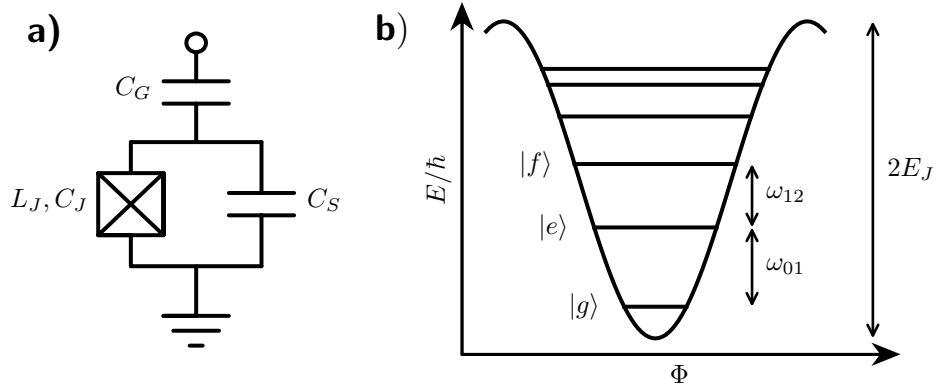


Figure 6: **(a)** Circuit diagram of the transmon. Shunt and gate capacitor control the relative contribution of inductive and capacitive energy of the Josephson junction. The transmon-regime $E_J/E_C \approx 50$ offers reduced charge noise and improved stability. The resulting periodic potential **(b)** can be approximated by an anharmonic oscillator with anharmonicity $\alpha = \omega_{12} - \omega_{01}$ for low energies. The total potential depth corresponds to roughly $2E_J$.

The transition frequency between ground and excited state is set by the energy contributions E_J and E_C via

$$\hbar\omega_{01} = \sqrt{8E_J E_C} \quad (25)$$

In the transmon-regime $E_J/E_C > 50$, the energy fluctuation due to charge noise is suppressed, allowing for a stable operation of the qubit [24]. When the linewidth γ is smaller than the anharmonicity

$$\alpha = \omega_{12} - \omega_{01} \approx -E_C, \quad (26)$$

the states are resolvable as individual peaks in the spectrum.

The transition frequencies of a transmon are typically in the range of 4 GHz to 10 GHz. Coupling such an artificial atom to a 3D microwave cavity presents a cavity QED system in the microwave regime, as discussed in the following section.

2.3 Cavity QED with Quantum Circuits

This section combines the above concepts and relates, how a transmon in a three dimensional microwave cavity can be treated as a cavity QED system. Sec. 2.3.1 provides a detailed description of the cavity. The cavity mode and its representation as a quantized harmonic LC oscillator are presented in the first part of this section. The second part



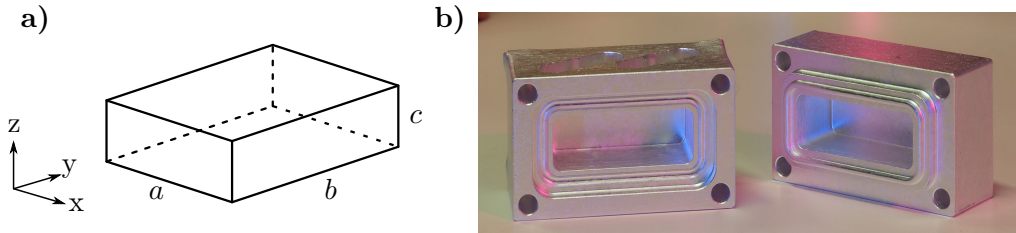


Figure 7: Rectangular 3D cavity. **Left:** Sketch of the hollow inside of the cavity with labels of the relevant dimensions. **Right:** Photograph of the two halves of the aluminium cavity which was used in this experiment. RF couplers are not attached, two ports for attachment are visible on top of the left half.

treats the coupling between the cavity and a transmission line, introducing the powerful concept of internal and external (coupling) quality factors. Finally, the coupling between cavity and transmon is discussed in sec. 2.3.2. The dispersive regime of the interaction is introduced by the simplified model of a two-level transmon. Sec. 2.3.3 presents the expanded model and the three-level transmon Hamiltonian. It covers the essential physics necessary to understand the results presented in the experimental part of this thesis.

2.3.1 Rectangular 3D Microwave Cavities

A rectangular microwave cavity is a hollow cuboid inside a solid block of bulk metal. It is typically fabricated by cutting the block in half and milling out the hollow inner part of the cavity. The two halves are put back together and screwed tight. Fig. 7 shows a sketch of the cavity and a photo of two halves of an aluminium cavity. A comprehensive analysis of various types of 3D microwave cavities and their applications in superconducting circuits is found in [25].

Cavity Mode

The conductive metal walls impose strong boundary conditions on the electromagnetic field inside the cavity. The spatial and temporal shape of the cavity modes is defined by the solutions of Maxwell's equations. Let the dimensions of the rectangular cavity be a , b and c in direction of the x -, y - and z -axis respectively. The resonance frequencies of the sustained modes are

$$f_{lmn} = \frac{c}{2} \sqrt{\frac{l^2}{a^2} + \frac{m^2}{b^2} + \frac{n^2}{c^2}} \quad (27)$$

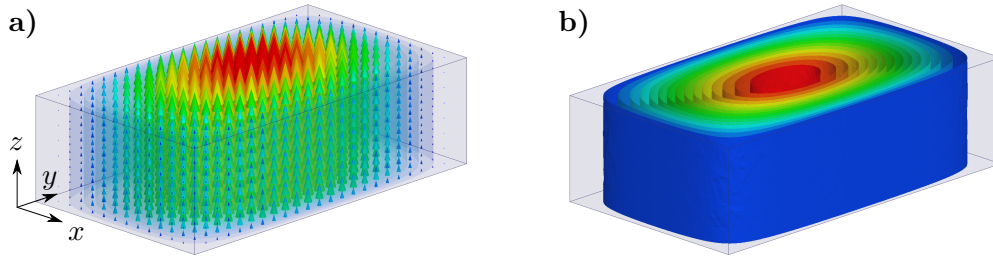


Figure 8: Electric field of the \mathbf{TE}_{110} mode of a rectangular microwave cavity. The magnitude of the field is encoded in the color going from blue (weak field) to red (strong field). The cavity was simulated with *HFFS*. **(a)** Vector plot. The only non-zero component of the E-field goes along the z -axis. It oscillates with the resonance frequency f_{110} . **(b)** Magnitude of the field. The magnitude is constant in z and decreases from its maximum value in the center to 0 at the walls in x - and y -direction. The mode is also termed ‘sushi roll’, referring to the shape of the equipotential surfaces.

with the speed of light c . The indices l , m and n denote the number of anti-nodes of the standing electric field inside the cavity along the x -, y - and z -axis respectively. Only one of these indices may be 0 at a time, in order to not violate the boundary conditions [26]. Typical desired resonance frequencies in circuit QED are about 10 GHz, which corresponds to length scales a, b, c on the order of centimetres. Let the cavity have the smallest extent in z -direction $c < a, b$. In that case, the cavity mode with the lowest frequency is $(l, m, n) = (1, 1, 0)$. The spatial shape of the \mathbf{TE}_{110} mode (transverse electric) is sketched in fig. 8.

Its electric field is orientated in parallel with the z -axis, the components in x and y direction are 0. The magnitude is constant along z . Looking at the x - y -plane, the magnitude is strongest in the cavity center and falls off to 0 at the walls following a sinusoidal function. The charge in the bulk metal follows the electric field with a 90° phase shift. It periodically flows back and forth between the cavity top and bottom. This behaviour resembles the oscillating current in a resonant LC -circuit. Hence, the cavity’s \mathbf{TE}_{110} mode is well modelled by an LC -resonator with resonance frequency $\omega_r = 1/\sqrt{LC} = 2\pi f_{110}$. This equivalent circuit model allows an intuitive picture of the coupling between a cavity and a coaxial transmission line, as is discussed in the next subsection.

In terms of quantum mechanics, a single mode of the cavity is simply described as a harmonic oscillator

$$H_{\text{cav}} = \hbar\omega_r \left(a^\dagger a + \frac{1}{2} \right) \quad (28)$$

with the bosonic ladder operators a^\dagger and a that add or remove a photon from the mode. This Hamiltonian only describes the coherent behaviour of a lossless mode. In any real



system, the energy will always decay over time due to various loss mechanisms. There are several channels for internal loss in 3D microwave resonators. Dielectrics inside the cavity (e.g. air instead of vacuum, a sapphire chip carrying a qubit or residual oxide layers on the walls) lead to dielectric loss of the energy stored in the electric field. Conductor loss relates to the energy dissipated due to finite conductivity of the metallic cavity walls that carry the current. The border, where the cavity is cut open during fabrication, is potentially a region of even higher resistivity. However, this so-called seam loss can be reduced by lining the seam with indium before the two halves of the cavity are bolted together [27]. These internal loss channels are combined in the decay rate κ_{int} . The exponential energy decay in the time domain $\sim e^{-\kappa_{\text{int}}t}$ corresponds to a Lorentzian frequency spectrum centred at ω_r with a width of κ_{int} . The quality factor Q relates the decay rate to the frequency and allows the comparison of the energy storing capabilities of resonators operating at different frequencies. It is defined as

$$Q = 2\pi \frac{\text{Total energy stored}}{\text{Energy lost per cycle}}. \quad (29)$$

It can be roughly imagined as the number of times a photon is reflected back and forth before it is lost. When considering only internal losses, the quality factor is simply $Q = Q_{\text{int}} = \omega_r / \kappa_{\text{int}}$. However, Q_{int} can never be directly observed in the experiment. Performing spectroscopic measurement of the cavity requires a connection to a measurement device. This coupling inevitably adds an additional decay channel that lowers the quality factor of the resonator.

Coupling to the outside world

In order to probe the cavity one needs to establish a connection to the outside world. The first choice to transport microwave signals to the cavity and back is a coaxial cable. Its center conductor is cylindrically surrounded by the grounded outer conductor with a dielectricum (typically polyethylene) in between. Signals are transported in form of *TEM* waves, both the electric and the magnetic fields are transverse to the propagation direction. The connection is made by drilling a hole in the cavity wall and attaching the cable via an SMA flange. Fig. 9 shows the schematics of this setup. The cylindrical hole in the cavity wall forms a short waveguide section. Signals below the waveguide's cutoff frequency do not propagate freely, but instead decay exponentially

$$\vec{E}(x, y, z) = \vec{E}(x, y, z = 0)e^{-\beta z} \quad (30)$$

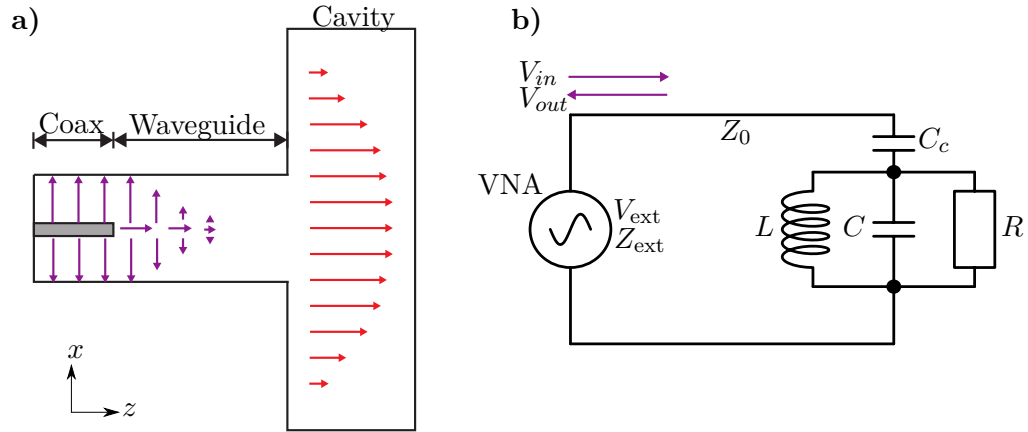


Figure 9: Coupling the resonator to a coaxial feedline. **(a)** Cut through the x - z -plane of the 3D structure. A signal propagates along the coaxial cable in form of a TEM -wave. In the waveguide section, the intensity of the field decreases exponentially in direction of the Z -axis. The coupling strength is defined by the overlap of the decaying field with the TE_{110} mode in the resonator. It can be controlled by designing the length of the waveguide section accordingly. **(b)** Equivalent circuit diagram. The cavity is represented by a parallel LCR resonator and the coaxial cable by a transmission line with characteristic impedance Z_0 . A coupling capacitance C_c models the coupling through the waveguide section. The quantity of interest is the reflection coefficient S_{11} , that relates voltage signals going in and out of the resonator $V_{out} = S_{11}V_{in}$. External measurement circuitry (typically a VNA) is modelled by a source V_{ext} with internal impedance Z_{ext} . Image adapted from [25].

with the propagation constant β . The overlap between this evanescent field and the cavity mode defines the coupling of the coaxial cable and the cavity. Due to the exponential decay, the coupling strength depends crucially on the length of the waveguide section. This is used in the experiment to control the coupling by adjusting the pin-length at the end of the coaxial cable. A comprehensive analysis of the energy transfer in terms of electrodynamics is done in [25]. The main results agree with what one would intuitively expect - the cavity is most susceptible to absorb energy close to its resonance frequency. Also, the connection to a measurement apparatus introduces an additional decay channel, that reduces the total quality factor of the resonator.

To get a better understanding of the coupled system, it helps to look at the equivalent electronic circuit depicted in fig. 9. The distributed three-dimensional structure is modelled with a network of lumped elements. The lossy cavity mode is represented by a parallel LCR resonator. External measurement circuitry (in most cases a vector network analyser VNA) is modelled by the AC source V_{ext} with internal impedance Z_{ext} . It is connected to the



cavity via a transmission line with a characteristic impedance of Z_0 that is usually matched to the source. The coupling is modelled by the coupling capacitance C_c . Let us assume the source emits a signal of the form $V_{in} = V_0 e^{i\omega t}$. Travelling along the transmission line, the incoming signal encounters an impedance change at the resonator from Z_0 to $Z_{in} = 1/i\omega C_c + Z_{LCR}$, where

$$Z_{LCR} = \left(\frac{1}{i\omega L} + i\omega C + \frac{1}{R} \right)^{-1} \quad (31)$$

is the input impedance of the LCR circuit. The sudden change in impedance causes reflection of the incoming signal $V_{out} = S_{11} V_{in}$ with the complex reflection parameter

$$S_{11} = \frac{Z_{in} - Z_0}{Z_{in} + Z_0}. \quad (32)$$

The scattering parameters of a resonator connected to an external load, can be significantly different compared to an unloaded resonator. A well-written summary is found in [28]. The key result is, that the additional circuitry results in a larger decay rate $\kappa = \omega_r / Q_l$. The loaded quality factor Q_l has two contributions

$$\frac{1}{Q_l} = \frac{1}{Q_{\text{int}}} + \frac{1}{Q_c}, \quad (33)$$

with the coupling quality factor Q_c accounting for the losses due to the external measurement apparatus. If either the internal or the coupling losses exceed the other, the overall Q_l of resonator is dominated by the strongest decay channel. The different regimes, set by the relative ratios of Q_{int} and Q_c are listed in tab. 1. According to [29], the complex

$Q_c \approx Q_{\text{int}}$	critically coupled
$Q_c \gg Q_{\text{int}}$	under-coupled
$Q_c \ll Q_{\text{int}}$	over-coupled

Table 1: Naming convention for the different coupling regimes of a loaded resonator.

reflection parameter of the cavity reads

$$S_{11} = \frac{2Q_l/Q_c}{1 - 2iQ_l \frac{\omega - \omega_r}{\omega_r}} - 1. \quad (34)$$

It depends not only on the total quality of the loaded resonator Q_l , but also on the relative contributions of Q_{int} and Q_c . Taking a power spectrum with a vector network analyzer (**VNA**) corresponds to measuring $|S_{11}|^2 = P_{out}/P_{in}$. The spectrum has the shape of a

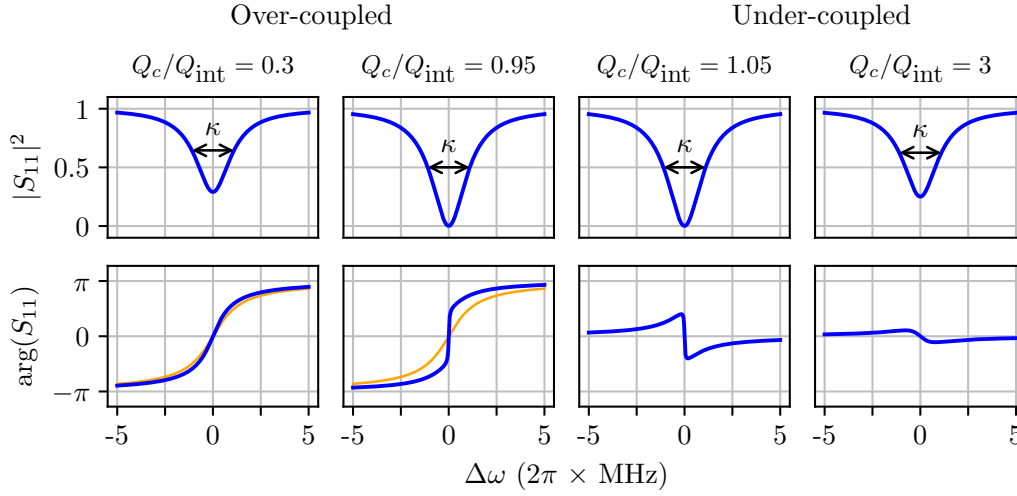


Figure 10: Reflection coefficient S_{11} of the loaded rectangular microwave resonator in different coupling regimes. The data is computed numerically following eq. 34 and plotted as a function of the detuning $\Delta\omega = \omega - \omega_r$. Fixed parameters are $\omega_r = 2\pi \times 8.8$ GHz and $Q_l = 4000$, corresponding to a decay rate of $\kappa = 2\pi \times 2.2$ MHz. **Top row:** The magnitude $|S_{11}|^2$ is only affected slightly by the ratio Q_c/Q_{int} . Only the depth of the dip changes, decay rate κ and the resonance frequency ω_r are independent. **Bottom row:** In the over-coupled regime, the phase response undergoes a 2π phase shift. It is well approximated by eq. 36 (orange), especially for a highly over-coupled resonator $Q_c \ll Q_{\text{int}}$. There is no permanent phase shift in the response of an under-coupled resonator, only a discontinuity around resonance.

Lorentzian

$$|S_{11}|^2 = 1 - \frac{\kappa^2 Q_l^2 / (4Q_c^2)}{(\kappa/2)^2 + (\omega - \omega_r)^2}, \quad (35)$$

centred at ω_r with a full-width-half-maximum (**FWHM**) of κ . The width depends solely on the loaded quality factor, the constituents Q_{int} and Q_c only influence the depth of the dip. Off-resonance, the incident power is fully reflected back from the resonator $|S_{11}|^2 \approx 1$. The analytic expression for the phase $\theta(\omega) = \arg(S_{11})$ is quite unsightly, and therefore not reproduced here. In the over-coupled regime, it can be approximated by

$$\theta(\omega) = 2 \arctan \left(2Q_l \left(1 - \frac{\omega}{\omega_r} \right) \right). \quad (36)$$

Fig. 10 shows the cavity response in the different coupling regimes. The magnitude $|S_{11}|^2$ is only slightly affected by the ratio Q_c/Q_{int} . The depth of the dip changes, whereas ω_r and κ remain unaffected. However, the cavity's phase response depends strongly on the



internal and coupling quality factor. In the over-coupled regime, the phase undergoes a full 2π phase shift and approximately follows eq. 36. As soon as $Q_c \geq Q_{\text{int}}$ the 2π phase-shift disappears. Only a discontinuity around f_r remains, which is flattening out for higher relative values of Q_c .

2.3.2 Transmon Coupled to a 3D Microwave Cavity

A transmon placed inside a 3D microwave cavity results in a dipole interaction between the systems [18]. Strongest coupling is achieved, when the transmon's 'antenna' (the gate capacitor) is in parallel with the electric field of the cavity mode. A sketch of this configuration is shown in fig. 11. This section is divided into two parts. The first part describes the dispersive limit of the interaction, followed by a discussion of the transmon linewidth and its limiting factors.

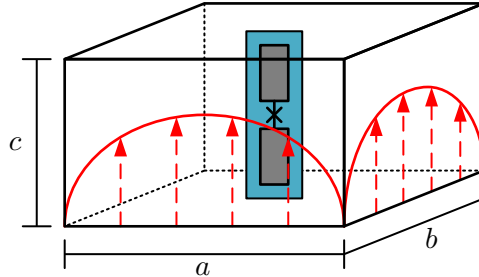


Figure 11: Transmon inside a 3D rectangular cavity. The transmon (grey) is held in place by a sapphire substrate (blue). The electric field of the cavity mode is indicated in red. The coupling between transmon and cavity mode is largest, when the transmon's antenna is arranged in parallel with the electric field of the mode.

Hamiltonian and spectrum

The cavity mediated coupling between two neighbouring transmon states i and j is described by the coupling strength g_{ij} . The detuning between a specific transmon transition $|i\rangle \leftrightarrow |j\rangle$ and the cavity is denoted as $\Delta_{ij} = \omega_{ij} - \omega_r$ with the transition frequencies $\omega_{ij} = \omega_j - \omega_i$. This section deals with the restricted case of a two-level transmon, treating it as a qubit with states $|g\rangle$ and $|e\rangle$. The model can be easily expanded to include three or more states, as shown below in sec. 2.3.3. Considering only the energy conserving terms

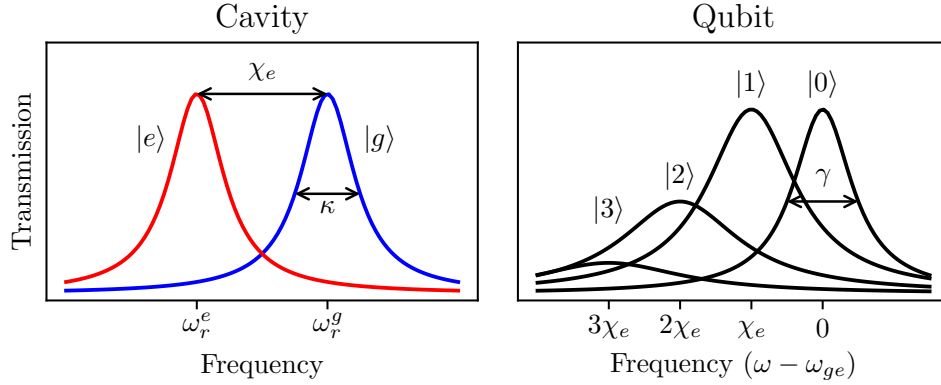


Figure 12: Cavity and qubit spectra in the dispersive limit of the Jaynes-Cummings model. **Left:** When the qubit is in the excited state $|e\rangle$, the cavity resonance frequency ω_r^g is shifted to $\omega_r^e = \omega_r^g + \chi_e$. The individual peaks are resolved, when the dispersive shift exceeds the cavity linewidth $\chi_e > \kappa$. This enables dispersive readout of the qubit via probing the cavity. **Right:** The qubit transition frequency ω_{ge} is shifted by $n\chi_e$, where n denotes the number of photons in the cavity. The plotted qubit spectrum corresponds to the poissonian photon distribution of a coherent state with an average photon number $\langle n \rangle = 1$. The photon number peaks are resolved when $\chi_e > \gamma$. Peaks broaden with $n\kappa$ plus additional effects due to measurement induced dephasing and charge noise [30]. Plot parameters are $-\chi_e = \gamma = 2\kappa$.

of the dipole interaction brings us back to the Jaynes-Cummings Hamiltonian [18]

$$H_{\text{JC}} = \hbar\omega_r a^\dagger a + \hbar\omega_0 |g\rangle \langle g| + \hbar\omega_1 |e\rangle \langle e| + \hbar g_{0,1} \left(a^\dagger |g\rangle \langle e| + a |e\rangle \langle g| \right). \quad (37)$$

Resolving the photon number peaks in the qubit spectrum marks the threshold of strong dispersive cavity QED. The precondition $\chi_e > \gamma$ can be met with a transmon-cavity architecture, as demonstrated by Schuster et al. in 2006 [31]. In the dispersive regime, where $4 \langle a^\dagger a \rangle (g_{01}/\Delta_{01})^2 \ll 1$ this Hamiltonian can be approximated by

$$H_{\text{Disp}}^{2\text{lvl}} = \hbar\omega_r^g a^\dagger a + \hbar\omega_e |e\rangle \langle e| + \chi_e a^\dagger a |e\rangle \langle e| \quad (38)$$

as shown in [32] with the convention $\omega_0 = 0$. The approximation holds up to a critical cavity photon number of

$$n_{\text{crit}} = \frac{1}{4} \frac{\Delta_{01}^2}{g_{01}^2}. \quad (39)$$

Including not only two, but all the transmon's states in the calculation, results in a renormalization of the cavity $\omega_r^g = \omega_r - \chi_{01}$. Also, the qubit transition frequency is Lamb-shifted



to $\omega_{ge} = \omega_{01} + \chi_{01}$. The partial dispersive shifts read

$$\chi_{ij} = \frac{g_{ij}^2}{\Delta_{ij}} \quad (40)$$

and the dispersive shift, connected to the excited state of the transmon qubit, is given by

$$\chi_e = 2\chi_{01} - \chi_{12}. \quad (41)$$

There are two equivalent perspectives to interpret the dispersive interaction. Note that the dispersive shift can be positive or negative, depending on the sign of Δ . Thinking about the qubit, it is clear that the photons in the cavity shift the qubit transition frequency by χ_e per photon, a typical example of the *AC stark effect*. Likewise, the resonance frequency of the cavity is shifted by χ_e , when the qubit is in the excited state $|e\rangle$. The shifted cavity frequency is denoted by

$$\omega_r^e = \omega_r^g + \chi_e. \quad (42)$$

Fig. 12 shows the dispersive spectra of the qubit and the cavity.

The qubit dependent dispersive cavity-shift is resolved when $\chi_e \geq \kappa$. In this regime, the state of the qubit can be measured by determining the cavity resonance frequency. This can be done by applying an external microwave signal. After interacting with the qubit-cavity-system, the probe signal conveys the information about the qubit state. Probing at either ω_r^g or ω_r^e imprints the information in the signals amplitude. Alternatively, a probe signal at $(\omega_r^g + \omega_r^e)/2$ experiences a qubit dependent phase shift. The contrast of such a measurement is highest, when the cavity is narrow and the dispersive shift large $\chi_e \gg \kappa$. However, a small decay rate κ limits the rate at which the probe field can escape the cavity and extract information about the qubit state. In terms of fast readout and highest possible contrast, the condition for optimal readout is

$$\chi_e = \kappa, \quad (43)$$

according to [18] and [33]. The probe power should be sufficiently low to firstly preserve the dispersive interaction and secondly, keep measurement induced dephasing (line broadening) at a minimum [30]. The following section 2.3.3 expands this idea of **dispersive readout** to a three level transmon instead of a qubit.

Transmon linewidth

The spectroscopic linewidth of the transmon is determined by its dephasing time $T_2 = 1/\gamma_2$. As discussed in [34], the dephasing rate γ_2 is related to the experimentally observed FWHM linewidth $\Delta f = \gamma/(2\pi)$ via

$$\gamma_2 = \frac{1}{2}\gamma. \quad (44)$$

Both the qubit decay rate $\gamma_1 = 1/T_1$ and the ‘pure dephasing’ γ_ϕ contribute to the dephasing rate

$$\gamma_2 = \frac{1}{2}\gamma_1 + \gamma_\phi. \quad (45)$$

Possible sources for dephasing are charge and flux noise as well as the interaction with the substrate [24]. Quasi particle tunneling is also suspected to cause dephasing [35]. Photon number fluctuations in the cavity cause dephasing by shifting the qubit frequency. Measurement induced dephasing can cause additional broadening of the line and strong deviations from the simple Lorentzian line-shape [30].

An upper limit of the qubit lifetime T_1 is given by the Purcell limit $T_1^{\max} = 1/\gamma_P$. The **Purcell-effect** [12] describes the effect of the cavity decay rate κ on the lifetime of the qubit. The reason for this additional decay channel is simply the dressing of the eigenstates of the coupled system. In the resonant case $\Delta = 0$, the system’s lowest excitation consists of an equally weighted superposition of the single photon state and the excited qubit state (see sec. 2.1.2). In the dispersive limit, the excited qubit state contains only a very small photonic component (normalization omitted)

$$|e\rangle = |e'\rangle \otimes |0'\rangle + \lambda |g'\rangle \otimes |1'\rangle, \quad (46)$$

with $\lambda \ll 1$ and the isolated basis states $\{|g'\rangle, |e'\rangle\}$ and $\{|0'\rangle, |1'\rangle, \dots\}$. As a result, the spontaneous emission rate for the excited qubit state will acquire the additional contribution

$$\gamma_P = \frac{g_{01}^2}{\Delta_{01}^2} \kappa. \quad (47)$$

The Purcell-limit can be the limiting factor of the qubit lifetime. It can be overcome by using Purcell-filters [36, 36].



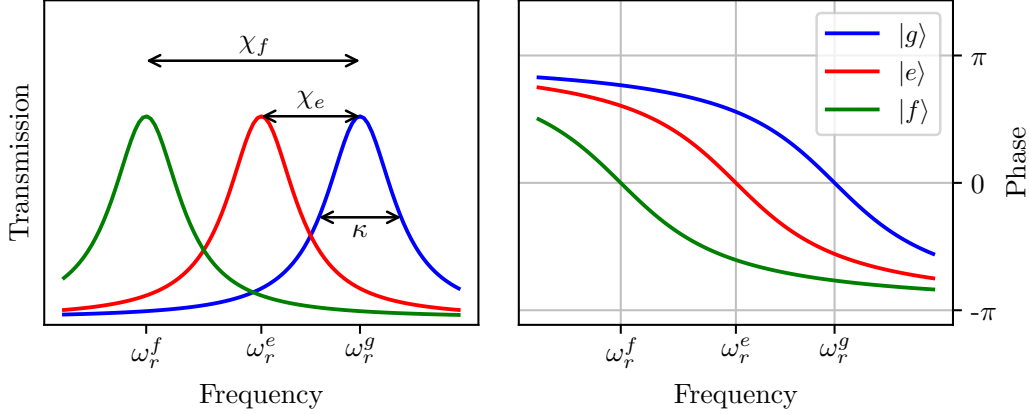


Figure 13: Three-level transmon dispersively coupled to a cavity, amplitude (**left**) and phase response (**right**). The cavity resonance frequency depends on the state of the qubit. If the transmon is in $|g\rangle$, $|e\rangle$ or $|f\rangle$ the cavity is resonant at ω_r^g , ω_r^e or ω_r^f respectively. Thus, the problem of determining the transmon's quantum state reduces to the problem of measuring the cavity resonance frequency. Plot parameters are $\chi_e = -\kappa$ and $\chi_f = -2.2\kappa$.

2.3.3 Dispersive Readout of a Three-level Transmon

In this section, the model is expanded to cover the third state of the transmon $|f\rangle$. The Hamiltonian reads

$$H_{\text{Disp}}^{\text{3lvl}} = \hbar\omega_r^g a^\dagger a + \hbar\omega_e |e\rangle \langle e| + \hbar\omega_f |f\rangle \langle f| + \chi_e a^\dagger a |e\rangle \langle e| + \chi_f a^\dagger a |f\rangle \langle f| \quad (48)$$

with $\chi_f = 2\chi_{12} - \chi_{23} \approx 2\chi_e$. The frequency of the transmon transition $|e\rangle \leftrightarrow |f\rangle$ is $\omega_{ef} = \omega_f - \omega_e$. When the transmon is in the state $|f\rangle$, the conditional cavity resonance frequency is

$$\omega_r^f = \omega_r^g + \chi_f. \quad (49)$$

The cavity spectrum is shown in fig. 13 for both amplitude and phase. Probing the cavity at ω_r^e gives the highest contrast to distinguish all three transmon states. The lamb shift of the second transmon transition $|e\rangle \leftrightarrow |f\rangle$ in terms of the isolated transition frequency ω_{12} reads [19]

$$\omega_{ef} = \omega_{12} + \chi_{12} - \chi_{01} \approx \omega_{12}. \quad (50)$$

Consequently, the anharmonicity defined in eq. 26 is well approximated by the difference of the lamb shifted transition frequencies of the coupled system

$$\alpha = \omega_{12} - \omega_{01} \approx \omega_{ef} - \omega_{ge}. \quad (51)$$

This definition is typically preferred as the ω_{ef} and ω_{ge} are directly observable in an experiment with a coupled cavity-qubit system. The qubit dependent cavity spectrum with the actual experimental parameters measured in this experiment is shown in sec. 5.1.

2.4 Summary

Section 2 outlined the application of superconducting circuits as a platform for cavity QED. A transmon artificial atom can be strongly coupled to a single field mode inside a 3D microwave cavity. The discussion is focused on the dispersive regime of the interaction, which is utilized in this project to perform QND readout of the transmon state. The dispersive three-level transmon Hamiltonian H_{Disp}^{3lv} captures the relevant system dynamics. Key experimental parameters are the transmon dependent cavity frequencies $\omega_r^g, \omega_r^e, \omega_r^f$, the dispersive shifts χ_e and χ_f and the cavity linewidth κ . The dispersive readout scheme is used to either distinguish the $|g\rangle$ state or both $|g\rangle$ and $|e\rangle$ from the higher transmon levels. Optimal ground state readout contrast is achieved for $\chi_e = \kappa$, assuming an over-coupled cavity. As we will see in the following section, this goal was not met in the design of the system, as the engineered coupling quality factor Q_c ended up almost equal to the cavity's internal quality factor Q_{int} .



3 Characterising the System

The main goal of this section is the determination of the qubit transition frequency ω_{ge} and the conditional cavity frequencies ω_r^g , ω_r^e and ω_r^f . Decay rates γ and κ for cavity and qubit are also measured. These quantities are determined by looking at the complex microwave response of the cavity, measured with a vector network analyser. Additional drive signals are activated on demand, in order to find the transition frequencies of the transmon.

3.1 Cavity Spectroscopy

Spectra are taken with a vector network analyser (**VNA**). This high precision instrument emits a microwave signal with probe frequency $\omega = 2\pi f$ and voltage amplitude $V_{\text{in}}(\omega)$ at port ‘1’. After interacting with the device under test, the returning signal’s phase and amplitude $V_{\text{out}}(\omega)$ are recorded at port ‘2’. The complex scattering parameter $S_{21}(\omega)$ describes the relative amplitude

$$S_{21}(\omega) = V_{\text{out}}(\omega)/V_{\text{in}}(\omega) \quad (52)$$

of outgoing and incoming signal. The phase information is incorporated in the argument

$$\text{phase}(\omega) = \arg(S_{21}(\omega)). \quad (53)$$

In many cases, the scattered power magnitude $|S_{21}(\omega)|^2$ is of interest. It is often stated in units of decibel **dB**

$$|S_{21}(\omega)|^2 [\text{dB}] = 10 \log_{10} (|S_{21}(\omega)|^2). \quad (54)$$

When measuring scattering parameters with a VNA, the probe frequency is changed in discrete steps to cover the desired frequency range, where the number of steps defines the frequency resolution. Noise reduction is achieved by either averaging a series of measurements or reducing the intermediate frequency (**IF**) bandwidth. This parameter is related to the VNA’s internal signal processing and filtering. A narrow IF bandwidth means less noise contribution from frequencies other than the one that is currently measured. However, it is inversely proportional to the measurement time and should be adjusted carefully to the experimental requirements. The scattering parameter $S_{11}(\omega)$ compares the incoming wave to the reflected wave at the same port. A comprehensive introduction on microwave networks and scattering parameters is found in [26].

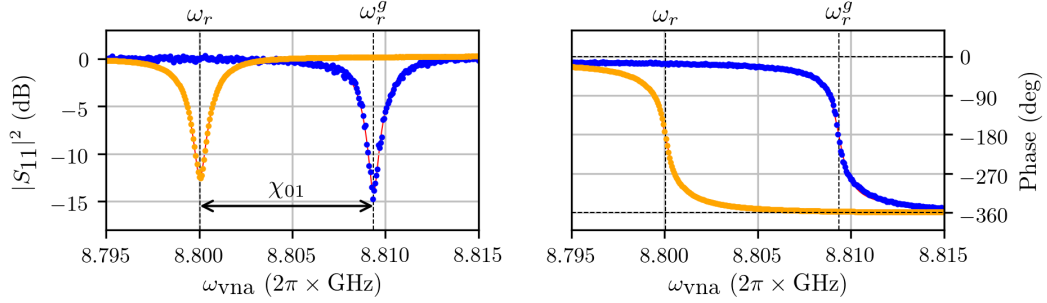


Figure 14: Two reflection spectra of the cavity taken with high (orange) and low (blue) probe power, corresponding to roughly $\langle n^{\text{high}} \rangle \approx 14000$ and $\langle n^{\text{low}} \rangle \approx 5$ cavity photons. The plots show magnitude (**left**) and phase (**right**) of S_{11} . Results of the circle fit are drawn in red. Probing the cavity with only a few photons reveals the effect of the coupling between transmon and cavity. The resonance is found at the lamb shifted frequency ω_r^g . Conversely, the quantum mechanical interaction are completely ‘washed out’ in the high power measurement, resulting in the uncoupled resonance frequency $\omega_r^g = \omega_r - \chi_{01}$.

3.1.1 Entering the Quantum World: From High to Low Power

The nonlinearity of the coupled system is revealed, when taking a spectrum with different probe powers. Fig. 14 shows the response in magnitude and phase of two reflection measurements with $\tilde{P}_{\text{in}}^{\text{low}} = -124$ dBm (blue) and $\tilde{P}_{\text{in}}^{\text{high}} = -89$ dBm (orange). The low and high power measurements yield a significantly different result for the position of the cavity resonance. In the low power measurement, the average photon population of the cavity mode is close to 1. The resonance frequency is found at the lamb shifted cavity frequency ω_r^g (due to the interaction with the transmon). When the cavity is probed with a large number of photons, the trace of the system’s interaction on the quantum level disappears. Currents above the junctions critical current I_c , result in a breakdown of the superconductivity, effectively making the qubit disappear. Therefore, the measurement results the uncoupled resonance frequency $\omega_r = \omega_r^g + \chi_{01}$.

Let us have a closer look on the measured data. The magnitude (when plotted linearly) follows a Lorentzian line shape, whereas the phase response is shaped like an arctangent. Both amplitude and phase information can be processed together by fitting eq. 34 to the complex response S_{11} . This is done by performing a circle fit routine, which was implemented by Zöpfl and Schneider. Detailed information is found in [37]. The resulting fit is drawn in red in the graph and the important parameters are listed in tab. 2. The circle fit not only calculates the loaded coupling Q_l , but also its constituents Q_c and Q_{int} . Detailed knowledge about the internal and coupling quality factors allows to make an



$\omega_r^g/2\pi$	8.809 47(1) GHz
$\omega_r/2\pi$	8.800 017(5) GHz
$\chi_{01}/2\pi$	-9.46(1) MHz
Q_l	3847(20)
Q_c	6461(25)
Q_{int}	9510(170)

Table 2: Summary of the experimental parameters of the coupled cavity-transmon system. Cavity resonance frequencies and the dispersive shift are extracted from a circle fit to the complex cavity response in a high ($\langle n^{\text{high}} \rangle \approx 18000$) and low ($\langle n^{\text{low}} \rangle \approx 5$) power measurement. Quality factors are derived from the low power data.

estimate of the average number of photons in the resonator. According to [38], an upper bound is given by

$$\langle n \rangle = \frac{2}{\hbar\omega^2} \frac{Q_l^2}{Q_c} \tilde{P}_{\text{in}}, \quad (55)$$

when the cavity is driven on resonance ω with power \tilde{P}_{in} at the input port of the cavity. The measurement powers translate to $\langle n^{\text{low}} \rangle \approx 5$ and $\langle n^{\text{high}} \rangle \approx 18000$. Despite being a rough estimate, these numbers confirm the explanation given above. The low-power measurement reflects the system’s quantum behaviour whereas the many photons of the high-power measurement encounter an almost entirely classical microwave resonator.

As discussed in sec. 2.3.2, the optimal setup for dispersive readout is an over-coupled resonator with $\kappa \approx \chi_e$. However, the fit of the resonator response reveals a very similar internal and coupling quality factor $Q_{int} \approx Q_c$. The reason is simply that the coupling pin of the cavity’s second port was not chosen short enough. It still couples comparatively well, providing a channel for energy decay and thus lowering the cavity’s internal quality factor. The cavity is much closer to being critically coupled instead of over-coupled. As a consequence, the phase response of the cavity is sharper than anticipated (compare fig. 10). Therefore, the expected phase difference between the $|g\rangle$ and the $|f\rangle$ state is close to 2π . Lower contrast of the dispersive readout has to be expected. Compensation is to some extent possible via higher readout powers or longer averaging times, accepting a decrease in the ‘QNDness’ of the measurement or a lower temporal resolution respectively.

3.1.2 Driving the Transmon

Qubit transition frequency

From the model of the coupled system we expect the information about the state of the transmon to be incorporated in the position of the cavity. In last section's low-power measurement, the cavity resonance was found at ω_r^g . There is no hint of a second peak in the spectrum, that would correspond to the qubit's excited state. Consequently, the transmon seems to be almost completely in the ground state $|g\rangle$. A short back-of-the-envelope calculation is enough to check, if this result makes sense. Assuming a thermal state for the transmon, the population of the first excited state is expected to be a factor of

$$e^{-\hbar\omega_{ge}/(k_B T)} \quad (56)$$

smaller, than the ground state population. Here k_B and T denote the Boltzmann-constant and the temperature respectively. A conservative estimate of a transition frequency of 5 GHz and a temperature of $T = 100$ mK results in a relative excited state population of 10%. Resolving a dip with only that fraction of the depth of the ground state resonance is hard, especially when expecting a dispersive shift on the order of the cavity width κ .

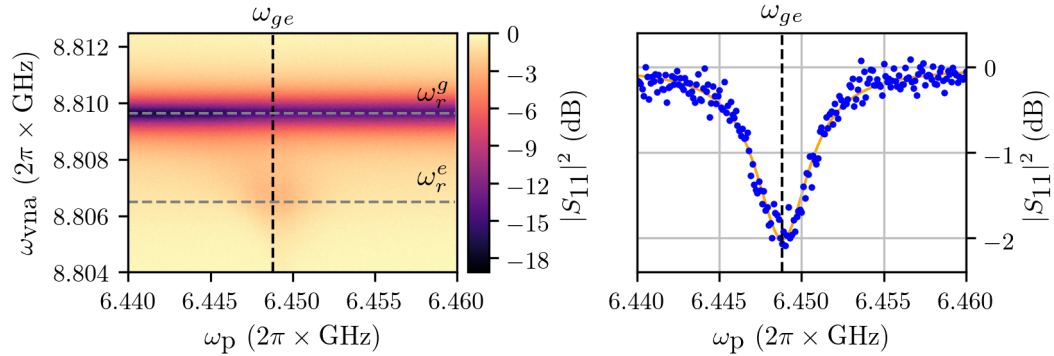


Figure 15: Two-tone measurement in order to find the qubit transition frequency ω_{ge} . VNA reflection spectra are recorded, while an additional drive signal with varying frequencies is applied. When the drive hits the qubit resonance at ω_{ge} , the additional peak, corresponding to the transmon's ground state, appears in the cavity spectrum. **Left:** Surface plot. The vertical line indicates ω_{ge} , the horizontal lines at ω_r^g and ω_r^e mark the state dependent position of the cavity. The separation corresponds to the dispersive shift χ_e . **Right:** Horizontal cut along ω_r^e . A Lorentzian fit (red) allows the determination of ω_{ge} and the effective qubit decay rate γ .

The dip can be made more prominent by shifting some of the transmon's population



into the excited state. Driving the qubit at the transition frequency ω_{ge} will cause Rabi-oscillations. In addition to the coherent evolution there will be competing processes, due to the connection to the surrounding bath. For low temperatures, the main effect will be energy relaxation. However, for a continuous drive with power p_{ge} there will be a stationary state, where the various rates of excitation and decay balance out. The resulting average population of the transmon's states is constant in time (as long as the drive is turned on) and may look significantly different than the thermal distribution. The transition saturates at a drive power p_{ge}^{sat} , that corresponds to an even probability of 50% for finding the qubit in $|g\rangle$ or in $|e\rangle$. At this point the contribution of the bath is negligible and the evolution is dominated by stimulated emission and absorption of drive photons. These processes occurring with the same rates sets the natural limit of half of the population being in the excited state.

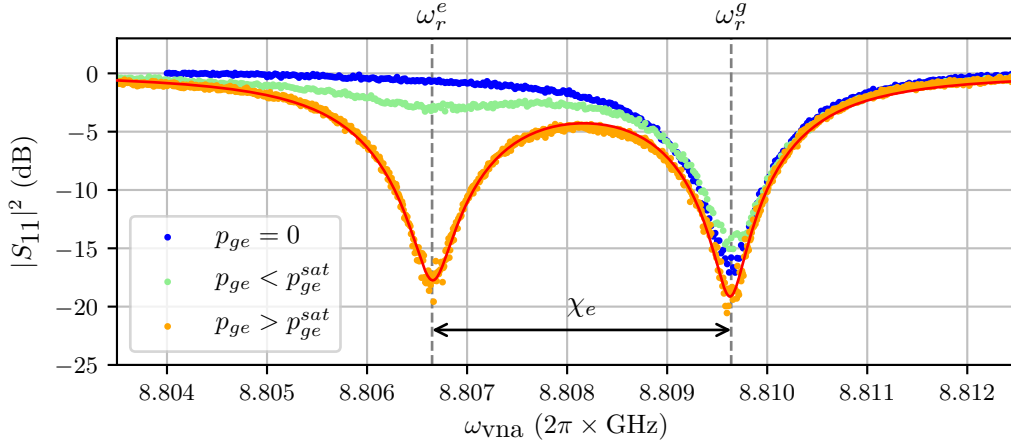


Figure 16: Cavity spectra while driving the qubit on resonance $\omega_p = \omega_{ge}$. As the drive power is increased, the cavity peak at ω_r^e becomes more and more prominent. Blue data presents a reference, where the drive is turned off. Green and orange correspond to driving the transition below respectively above the saturation intensity p_{ge}^{sat} . The dispersive shift χ_e is determined by fitting the sum of two Lorentzian profiles with a common width κ to the saturated spectrum (fit shown in red).

In order to find the transition frequency ω_{ge} a two-tone measurement is performed. That is done by applying an external probe signal and iterating its frequency f_p in small discrete steps. At each step a reflection spectrum of the cavity is taken with the VNA. The data is shown in fig. 15. When the probe hits the transition frequency $f_p = \omega_{ge}/(2\pi)$ the cavity dip corresponding to the transmon state $|e\rangle$ appears. A horizontal cut through the contour plot reveals the spectrum of the qubit's ge -transition. A Lorentzian fit of the linear data is used to extract the resonance frequency and the linewidth. The displayed data was measured

at a slightly too strong VNA probe and qubit drive power. Thus, the qubit transition is subjected to both an AC stark shift and power broadening. A more careful analysis described in sec. 5.4 results in $\omega_{ge} = 2\pi \times 6.449\,96(3)$ GHz and $\gamma = 2\pi \times 1.001(4)$ MHz using the lowest possible drive and VNA probe power that still produces a usable spectrum. The corresponding dephasing time $T_2 = 300(100)$ ns agrees well with typical values from the literature [6] [39]. As suggested in [34], an uncertainty of 30% is assumed for this method. The low power results are listed in the summary in tab. 3.

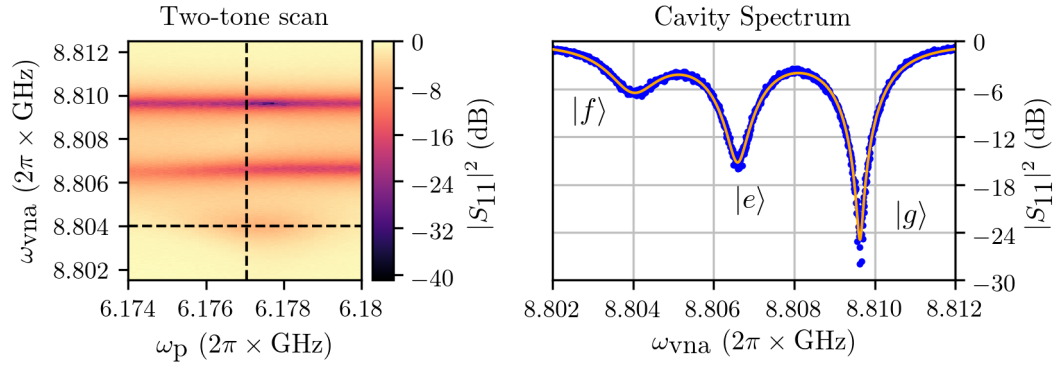


Figure 17: Two-tone scan while resonantly driving the ge -transition in saturation. The transmon’s $|f\rangle$ state gets populated, when the second drive signal hits ω_{ef} . Consequently, the third peak appears in the averaged cavity spectrum. **(Left)** Surface plot of the reflected magnitude with the frequency of the second drive on the x -axis. **(Right)** Vertical cut along ω_{ef} . The fit was obtained by fitting the sum of three Lorentzian profiles of the same width to the linear data (red). Cavity dips corresponding to the transmon states are labelled with $|g\rangle$, $|e\rangle$ and $|f\rangle$ respectively.

Note that the dephasing time presented in this section might still be underestimated. A measurement at even lower VNA and qubit drive power might have been possible using a higher number of averages and a lower IF frequency. The conventional method to determine T_2 is to perform a Ramsey type experiment, using a sequence of a $\pi/2$ excitation and a readout pulse after a varying delay time. In fact, a Ramsey measurement of the same transmon qubit a few months later resulted in a coherence time of several μ s.

Dispersive shift

With the knowledge about the qubit transition frequency, the dispersive shift χ_e can be determined. Fig. 16 shows, how an external drive at ω_{ge} with power p_{ge} affects the cavity spectrum. Data plotted in green corresponds to a weak drive, whereas the orange data corresponds to driving the transmon well in saturation $p_{ge} > p_{ge}^{sat}$. The blue data points



present a reference without the additional drive signal. Let us assume the drive renders the transmon in a mixed state with 50% probability of being in $|g\rangle$ or $|e\rangle$. Measuring the position of the cavity resonance frequency corresponds to a projective measurement of the qubit state. Therefore, a single measurement will result with equal probability in either finding the cavity at ω_r^g or ω_r^e . However, it is hardly possible to perform a VNA-measurement, that is accurate enough to resolve the qubit's state and is still faster than the rate at which the qubit changes its state (more on that topic follows in sec. 5). The presented data was acquired following the contrary approach. In order to minimize the noise of the signal, a number of 100 individual spectra were taken with high accuracy (low IF bandwidth). Both possible measurement results reoccur countless times, causing the cavity dips at ω_r^g or ω_r^e to appear side by side in the final averaged spectrum.

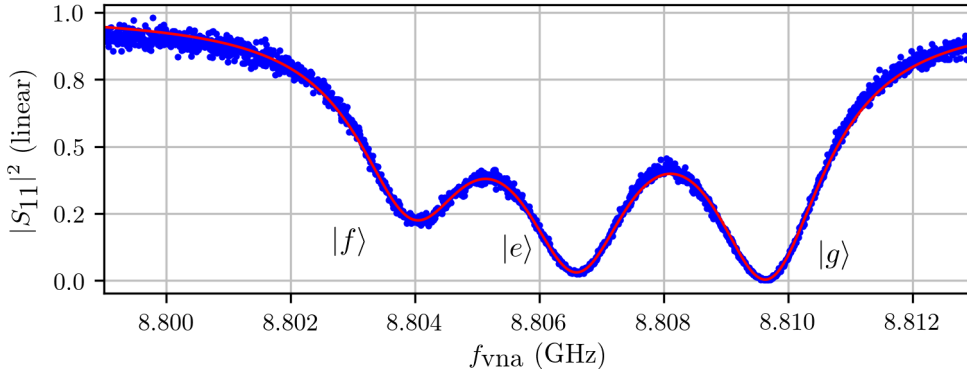


Figure 18: Averaged cavity spectrum while the transmon's three lowest states are populated (blue dots). Same data as in fig. 17, but showing the reflected magnitude using a linear scale $|S_{11}|^2 = |P_{out}/P_{in}|$. A sum of three Lorentzian profiles with a common decay rate κ was used for the fit (red line).

One can go a step further and try to populate the transmon's second excited state $|f\rangle$. It is possible to do this, by driving the $|g\rangle \leftrightarrow |e\rangle$ transition in saturation and adding an additional drive signal with a frequency ω_{ef} , corresponding to the energy difference between between first $|e\rangle$ and second excited state $|f\rangle$. A two-tone measurement as described above, but this time with the resonant ge -drive constantly running and repumping the excited state, does the trick in finding the transition frequency. A third dip appears in the cavity spectrum when the additional drive signal hits $\omega_{ef} = 2\pi \times 6.177\,31(2)$ GHz, see fig. 17. This shifted cavity dip corresponds to the transmon's $|f\rangle$ state and is centred at ω_r^f , shifted by $\chi_e + \chi_f \approx 2\chi_e$ from the ground state cavity resonance. The transmon interacting with the two external drives ends up in a stationary state, where all the system's transition rates are in equilibrium and the average population of each state stays constant. The

mean occupation is reflected in the cavity spectrum, which comprises of 100 individually recorded VNA-traces itself. To give an idea about the visual difference between linear and logarithmic depiction of the reflected magnitude $|S_{11}|^2$, the spectrum shown in fig. 17 is plotted again in fig. 18, using a linear scale. In the linear representation, the resonance has the form of a Lorentzian as given in eq. 35. Throughout this thesis, the linear data was used for analysis and fitting, but the logarithmic data is presented in the graphs. The key parameters describing the coupled cavity-transmon system are extracted from fitting a three-peaked Lorentzian (with common width $\kappa/(2\pi)$) to the linear data shown in fig. 18.

3.2 Summary of System Parameters

The key parameters of the coupled transmon cavity system are collected in tab. 3. The dispersive shift χ_e and the cavity decay rate κ are close to the optimal dispersive readout condition eq. 43. However, the cavity being critically coupled instead of over-coupled is expected to lower the contrast. The qubit linewidth is similar to κ and χ . Therefore, the number splitting of the qubit transition is most likely not resolved in the experiment.

Description	Symbol	Value
Cavity when transmon in $ g\rangle$	$\omega_c^g/2\pi$	8.809 641(2) GHz
Cavity when transmon in $ e\rangle$	$\omega_c^e/2\pi$	8.806 588(3) GHz
Cavity when transmon in $ f\rangle$	$\omega_c^f/2\pi$	8.803 983(3) GHz
$ e\rangle$ state dispersive shift	$\chi_e/2\pi$	-3.053(4) MHz
$ f\rangle$ state dispersive shift	$\chi_f/2\pi$	-5.658(4) MHz
Coupling rate	$g_{01}/2\pi$	149.09(8) MHz
Cavity decay rate	$\kappa/2\pi$	2.096(5) MHz
Transmon $ g\rangle \leftrightarrow e\rangle$ transition	$\omega_{ge}/2\pi$	6.449 96(3) GHz
Transmon $ e\rangle \leftrightarrow f\rangle$ transition	$\omega_{ef}/2\pi$	6.177 31(2) GHz
Anharmonicity	$\alpha/2\pi$	-272.65(4) MHz
Qubit linewidth (FWHM)	$\gamma/2\pi$	1.001(4) MHz
Dephasing time	T_2	300(100) ns

Table 3: Experimentally determined parameters of the transmon-cavity-system. Note that the qubit frequency ω_{ge} and dephasing rate γ_2 are determined in a low power measurement described in sec. 5.4. The dephasing time is derived from the qubit linewidth and not in the usual way from a Ramsey type experiment. T_2 might be underestimated, as the linewidth is easily subjected to broadening from either the qubit drive or the VNA probe signal.



4 Cranking up the Contrast: The Josephson Parametric Converter

This chapter is organized in five parts. Sec. 4.1 gives an introduction on which qualities are desired in a ‘good’ amplifier and how the added noise propagates along a measurement chain containing several staged amplifiers. The operational principle of the shunted microstrip JPC is explained in sec. 4.2. Two JPCs with serial numbers SN004 and SN010 are available to our research group. Their nominal tunable ranges and specifications as stated by the manufacturer are reproduced in sec. 4.3. The JPC SN004 was tested comprehensively, the results are presented in sec. 4.4. The delicate JPC tuning procedure is described in sec. 4.5. As the assembled JPC is rarely extracted from its surrounding mu metal shield, a photograph of the chip-housing and the immediate wiring is attached in the appendix in fig. 66.

4.1 Overview

Amplifiers play an important role in any experiment carrying out high precision measurements. Their purpose is to raise the level of a weak input signal to a macroscopic level in order to overcome the noise levels of any following processing hardware. Fig. 19 shows the basic scheme of operation of a linear amplifier. Incoming signal and noise are amplified with a gain G (assuming they lie within the amplifiers linear bandwidth). In addition to the gain, the amplifier also adds an additional amount of noise to the output signal. Thus, the SNR is reduced during the process of amplification.

Signal processing electronics at room temperature is generally quite noisy. Weak signals from measuring physics experiments at cryogenic temperatures can not be measured directly. In cryogenic experiments, this challenge can be overcome by using RF amplifiers called high electron mobility transistors (**HEMTs**). These devices are operated inside the cryostat at 4K and provide a gain of up to 40 dB over a range of ~ 10 GHz. However, HEMTs add many tens of noise photons. Measurement signals with powers on the level of single photons (per resonator bandwidth) can only be resolved with a large number of averages. This is where the JPC can prove its value. The noise added by a JPC is close to the quantum limit of half a photon. Used as a preamplifier before the HEMT, the JPC’s gain of ~ 20 dB is already enough to raise the signal power above the noise level of the HEMT, improving the SNR of the total measurement chain. Propagation of noise in a chain of amplifiers is discussed in more detail in sec. 4.4.4.

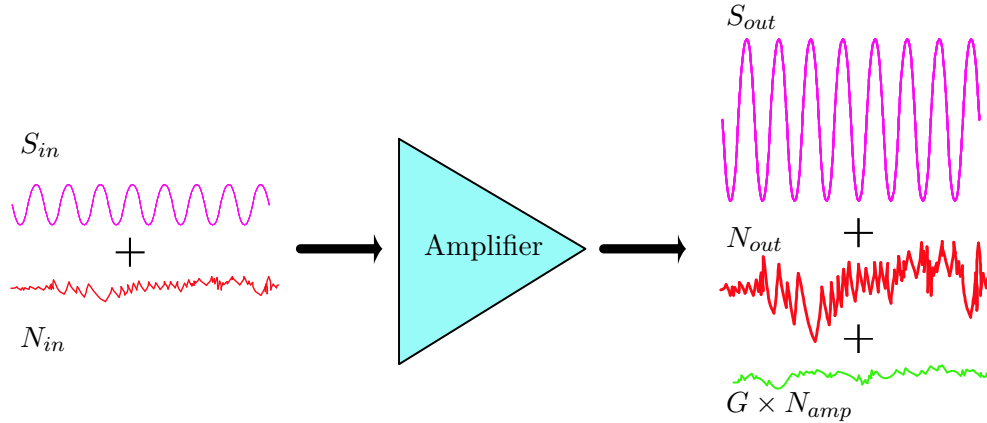


Figure 19: Basic operational principle of a linear amplifier with voltage gain G . Input signal S_{in} and noise N_{in} are amplified by the same amount $S_{out} = GS_{in}$ and $N_{out} = GN_{in}$. In addition to the amplification, the amplifier also adds noise $G \times N_{amp}$. As a consequence, linear amplification always reduces the input SNR. Image adapted from [40].

4.2 Operational Principle

4.2.1 The Josephson Ring Modulator

The Josephson ring modulator (JRM) consists of four nominally identical Josephson-Junctions that are arranged in a Wheatstone configuration as shown in fig. 20 (left). The idea of realising a mixing device by arranging non-linear elements in said configuration is not entirely new. In fact, a ring of four diodes is widely used in commercial RF mixers of all sorts [26]. To understand how the mixing of signals with powers corresponding to single photons comes about in a JRM, the circuit has to be analysed in the framework of circuit QED. The key ideas of the model are presented here, closely following [41] and [42]. For the sake of compactness, the basic variables of circuit QED that have already been stated in chapter 2.2, are reproduced in the first paragraph of the following section. The discussion of the JRM is organized in two parts, where the unshunted and the shunted JRM are discussed separately.

Unshunted JRM

The circuit diagram of the unshunted JRM is depicted on the left side of fig. 20. In order to describe the JRM, a set of independent variables describing the circuit has to be identified. A favourable choice are the node fluxes $\phi_i = \int_{-\infty}^t u_i(t') dt'$, that correspond to the time



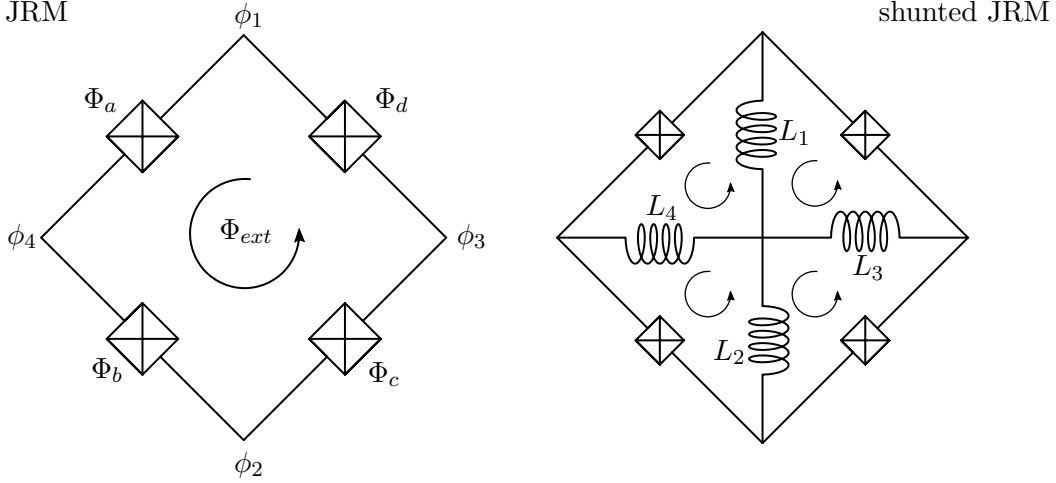


Figure 20: **Left:** The Josephson ring modulator (JRM) comprises of four identical Josephson-junctions in Wheatstone-bridge configuration. Node and branch fluxes are denoted as $\phi_{1,2,3,4}$, and $\Phi_{a,b,c,d}$. The branch fluxes are coupled through the highly non-linear junctions, allowing the device to be utilized as a non dissipative three-wave-mixer operating on the level of single photons. **Right:** Inductively shunted JRM. This design improves stability and frequency tunability when performing three-wave-mixing. Flux quantization for each of the four closed loops has to be taken into account.

integrated electric potentials at node $i \in \{1, 2, 3, 4\}$. The branch fluxes Φ_k through each junction $k \in \{a, b, c, d\}$ are defined in the usual way as the difference of the node fluxes enclosing that element, for example

$$\Phi_a = \phi_1 - \phi_2. \quad (57)$$

A DC biased coil provides experimental control over the device by introducing an external flux Φ_{ext} . In a superconducting loop, the total flux can only assume values that are multiples of the flux quantum Φ_0 . Consequently, the JRM's ring structure imposes the boundary condition

$$\Phi_a + \Phi_b + \Phi_c + \Phi_d = \Phi_{ext} + n\Phi_0 \quad (58)$$

on the branch fluxes. Assuming Φ_{ext} to be a known quantity, this effectively decreases the system's number of degrees of freedom to three. The four nominally equal junctions in the JRM are characterized by their Josephson energy E_J . The energy of an individual junction k depends not only on its coordinate Φ_k , but there is an additional contribution due to the external and the trapped flux. Due to the symmetry of the circuit, this contribution

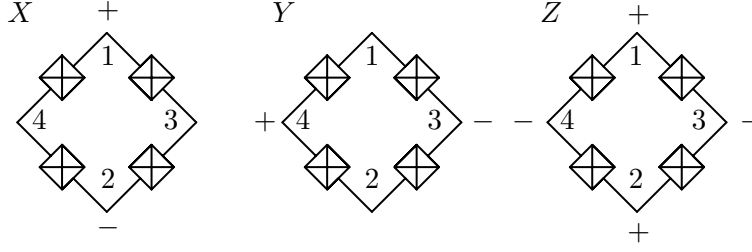


Figure 21: Normal modes parametrizing the JRM. The coupled modes X , Y and Z are used for three-wave-mixing. The fourth mode (not shown) is uncoupled and plays no part in the mixing process. The differential modes X and Y are called ‘signal’ and ‘idler’ whereas the common mode Z is referred to as ‘pump’.

is uniformly split up between the junctions. The energy of a single junction reads

$$E_k = -E_J \cos \left(\varphi_k + \frac{\varphi_{ext} + 2\pi n}{4} \right), \quad (59)$$

introducing the reduced variables $\varphi = \Phi/\Phi_0$ that go in units of radian. The total energy of the unshunted JRM is simply the sum of the energies of each individual junction

$$E_{JRM} = -E_J \sum_k \cos \left(\varphi_k + \frac{\varphi_{ext} + 2\pi n}{4} \right). \quad (60)$$

At this point of the derivation a redefinition of the basic variables ϕ_k is advisable

$$\begin{aligned} \Phi_X &= \phi_1 - \phi_2 \\ \Phi_Y &= \phi_4 - \phi_3 \\ \Phi_Z &= \phi_1 + \phi_2 - \phi_3 - \phi_4 \\ \Phi_W &= \phi_1 + \phi_2 + \phi_3 + \phi_4. \end{aligned} \quad (61)$$

The system dynamics relevant for three-wave-mixing is described by the modes X , Y and Z . This becomes clear when expressing the branch fluxes $\Phi_{a,b,c,d}$ in terms of the $\Phi_{X,Y,Z,W}$. The common mode W falls out of the equation and is effectively decoupled. A sketch of the modes is shown in fig. 21. In terms of the reduced fluxes $\varphi_{X,Y,Z} = \Phi_{X,Y,Z}/\Phi_0$ the energy of the JRM reads

$$\begin{aligned} E_{JRM} = -4E_J \left(\cos \frac{\varphi_X}{2} \cos \frac{\varphi_Y}{2} \cos \frac{\varphi_Z}{2} \cos \left(\frac{\varphi_{ext} + 2\pi n}{4} \right) + \right. \\ \left. \sin \frac{\varphi_X}{2} \sin \frac{\varphi_Y}{2} \sin \frac{\varphi_Z}{2} \sin \left(\frac{\varphi_{ext} + 2\pi n}{4} \right) \right). \end{aligned} \quad (62)$$



This expression already indicates how the JRM's strong non-linearity that is introduced by the junctions brings about mixing processes of the modes X , Y and Z . A Taylor expansion assuming weak excitations $\varphi_X, \varphi_Y, \varphi_Z \ll 1$ leads to

$$E_{JRM} = \lambda \varphi_X \varphi_Y \varphi_Z \sin\left(\frac{\varphi_{ext} + 2\pi n}{4}\right) + \mu (\varphi_X^2 + \varphi_Y^2 + \varphi_Z^2) \cos\left(\frac{\varphi_{ext} + 2\pi n}{4}\right) \quad (63)$$

with $\lambda = -2\pi^3 E_J$ and $\mu = \pi^2 E_J$. The expression contains the sought-after pure nonlinear coupling term $\varphi_X \varphi_Y \varphi_Z$, showing that the JRM is capable of three-wave-mixing. The additional term that is quadratic in the fluxes only renormalizes the mode frequencies. Unwanted terms (such as $\varphi_X \varphi_Y^2$) which would contaminate the mixing process are eliminated by the Wheatstone-bridge geometry of the JRM.

The number of flux quanta n threading the ring is still present in the final energy expression eq. 63, resulting in certain practical limits of the four junction JRM. There are four possible solutions corresponding to $n = 1, 2, 3, 4$. Which one of them is energetically favourable depends on the externally applied flux φ_{ext} . States with neighbouring n are degenerate only when $\Phi_{ext} \bmod \Phi_0 = \pi/2$, different configurations render the system energetically unstable [42]. Consequently, biasing the device such that the sine term (and thus the mixing) in eq. 63 is maximal, is not possible. Still, three-wave mixing with an unshunted JRM has been shown experimentally [42]. As expected, the abrupt transitions and hysteretic behaviour depending on the sweep-direction of the flux have been observed. The strong condition on the bias flux greatly limits the tunability of the device, reducing its practical relevance as a cryogenic RF amplifier.

Shunted JRM

The drawbacks of the original design can be overcome with a slight modification of the JRM. Fig. 20 (right) shows the circuit diagram of the so-called shunted JRM. Four identical shunt inductors connect the nodes of the ring, creating four loops with only one junction per loop. This leads to different boundary conditions for the branch fluxes. The trapped flux in each individual loop has to be taken into account and the branch fluxes Φ_{L_i} across the inductors $i \in 1, 2, 3, 4$ introduce additional degrees of freedom. For example, the boundary condition of loop a reads

$$\Phi_a - \Phi_{L_1} + \Phi_{L_4} = \frac{\Phi_{ext}}{4} + n_a \Phi_0, \quad (64)$$

with fluxes Φ_{L_i} across the inductors $i \in 1, 2, 3, 4$ and n_a as the number of flux quanta in

the loop. Similar equations hold for the remaining loops.

Using the same parametrization for the branch fluxes as described above in eq. 61 allows to derive an expression for the energy of the shunted JRM in terms of the modes X , Y and Z . In the limit of low excitations $\varphi_X, \varphi_Y, \varphi_Z \ll 1$ one finds

$$E_{JRM}^{shunted} = -E_J \sin\left(\frac{\varphi_{ext}}{4}\right) \varphi_X \varphi_Y \varphi_Z + \dots \quad (65)$$

The calculation and the full expression is found in [41] (eqn. 2.66). Again, the result contains the desired mixing term. Comparing eq. 63 and eq. 65 reveals the key advantage of the shunted JRM - the quantum numbers n_i associated with the trapped flux in the loops do not appear in the final equation. The degeneracy is lifted and the shunted JRM can be stably operated in a definite state, allowing the mixing term to be exploited over a far greater range.

In order to gain control about the relevant modes of the JRM, the ring is embedded in a resonant circuit, as shown in fig. 22. The sketched stripline resonators define the resonance frequencies $\omega_{a,b,c}$ and the (internal) quality factors of the modes X, Y, Z . They are typically realised on chip as coplanar stripline resonators. The differential modes X and Y are called ‘signal’ and ‘idler’ whereas the common mode Z is referred to as ‘pump’. Amplifiers which are based on this design are called ‘non-degenerate’, as signal and idler mode are spatially separated. The JRM can convert a pump photon at $\omega_c = \omega_a + \omega_b$ into two photons with frequencies ω_a and ω_b . This process is illustrated with the formalism of an ideal three-wave-mixing Hamiltonian in the subsection below.

Ideal mixing Hamiltonian

The JRM is embedded in a resonant circuit, resulting in a well defined frequency and decay rate for the modes X, Y, Z . Each mode can be individually described as a harmonic oscillator

$$\varphi_X = X_{ZPF} (a + a^\dagger) \quad (66)$$

with zero-point-fluctuations X_{ZPF} and the photon creation and annihilation operators a^\dagger and a . Modes Y and Z are defined analogously. As shown above, the JRM couples the three modes via the mixing term

$$H_{int}^{3-wave} = K \varphi_X \varphi_Y \varphi_Z, \quad (67)$$



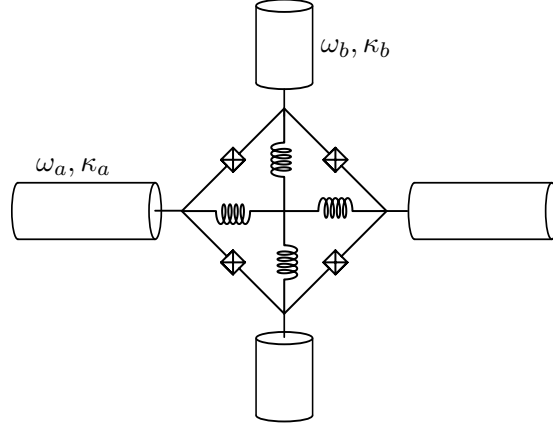


Figure 22: Shunted JRM with microstrip resonators as described in [43]. The length of the stripline resonators in combination with the effective inductance of the ring determine the resonance frequencies of the JRM modes. Resonance frequencies of signal (X) idler (Y) and pump (Z) mode are denoted ω_a , ω_b and $\omega_c = \omega_a + \omega_b$.

where the coupling strength is taken into account as K . The ideal Hamiltonian considering three harmonic oscillators interacting via $H_{\text{int}}^{3\text{-wave}}$ reads

$$H^{3\text{-wave}} = \hbar\omega_a a^\dagger a + \hbar\omega_b b^\dagger b + \hbar\omega_c c^\dagger c + \hbar g_3 \underbrace{(a + a^\dagger)}_{\varphi_X} \underbrace{(b + b^\dagger)}_{\varphi_Y} \underbrace{(c + c^\dagger)}_{\varphi_Z} \quad (68)$$

with $\hbar g_3 = K X_{\text{ZPF}} Y_{\text{ZPF}} Z_{\text{ZPF}}$. When aiming for photon conversion, the circuit surrounding the JRM is designed such, that

$$\omega_c = \omega_a + \omega_b. \quad (69)$$

Considering only the energy conserving terms of the rotating wave approximation, the Hamiltonian can be simplified to

$$H_{\text{RWA}}^{3\text{-wave}} = \hbar\omega_a a^\dagger a + \hbar\omega_b b^\dagger b + \hbar\omega_c c^\dagger c + \hbar g_3 (a^\dagger b^\dagger c + abc^\dagger) \quad (70)$$

as is shown in [43]. In this expression, the three-wave-mixing process becomes evident. The first term in the interaction part of the Hamiltonian corresponds to a pump photon with frequency ω_c being converted to two photons with frequencies ω_a and ω_b in signal and idler mode respectively. The second term describes the conjugate process of transforming one photon per signal and idler into one pump photon. When there are no photons in the idler mode, the up-conversion is physically impossible. In that way, the first term that adds photons in the signal mode can be fully utilized.

The next section relates how the JRM modes can be coupled to external transmission lines. That way, the circuit can be used as a parametric amplifier. The scattering matrix and the noise added by the amplifier are discussed.

4.2.2 Scattering Matrix and Added Noise

The previous section discussed, how the Josephson ring modulator (JRM) can be used to perform coherent three-wave-mixing between resonant modes defined by electronic stripline resonators. This section describes, how the amplification of travelling wave signals can be achieved by coupling the JRM to transmission lines. Using the formalism of input-output-theory, the scattering matrix of the JPC is derived. It provides an intuitive view of the JPC operating as a reflection amplifier. What makes the JPC so attractive, is that its added noise is close to the quantum limit of half a photon. This section is concluded by a discussion about the noise added by the JPC and its limitations regarding bandwidth and gain.

Coupling to transmission lines

The resonators that define the properties of the JRM modes are fabricated on chip in the form of coplanar stripline resonators. Fig. 23 shows a circuit digram of a possible realization. Signal and idler resonance frequencies ω_a and ω_b depend on the length of the stripline resonators and on the effective inductance $L_J(\Phi_{ext})$ of the JRM [44]. Thus, signal and idler resonator inherit the flux-tunability from the Josephson-junctions comprising the ring.

Hybrid couplers are used to address the different modes of the JRM. Hybrids are reciprocal four-port microwave devices with two input and two output ports [26]. The device acts as a power splitter, dividing incoming signals equally between the two output ports. However, the phase between the two output signals depends upon which input port is used. Signals coming in at the Δ -port acquire a relative phase-shift of 180° , whereas signals at the Σ -port are split without a relative phase-shift. The hybrid couplers allow the correct connection of the JRM's signal, idler and pump mode to transmission lines. Connecting to the Σ -port of one of the hybrids addresses the pump mode in accordance with fig. 21. Signal and idler mode are addressed via the Δ -ports.



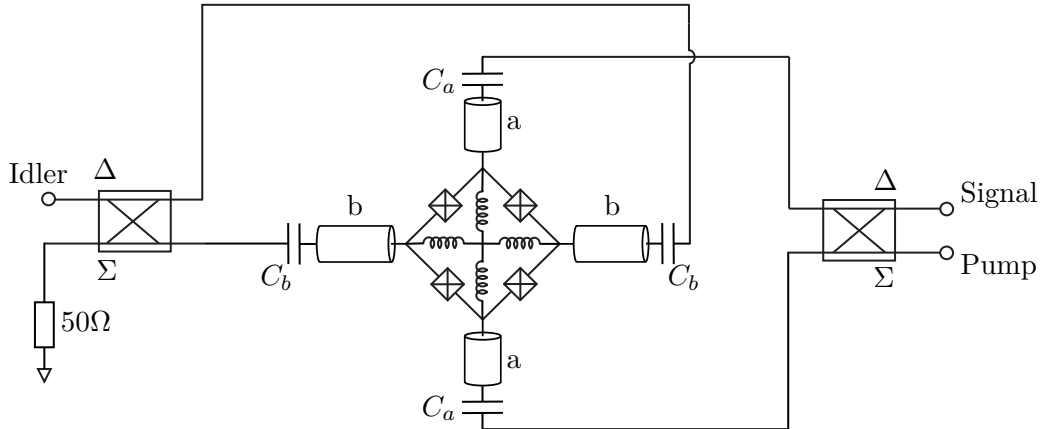


Figure 23: JPC wiring scheme. The three modes signal idler and pump are coupled to transmission lines via hybrid couplers. The couplers ensure, that the modes are addressed correctly. For example, a signal coming in at the Δ -port of the hybrid on the left, is equally divided between its output ports with a phase shift of 180° . Thus, the left and the right node of the JRM are excited in accordance with the definition of the idler mode in fig. 21. The superfluous port is terminated in a 50Ω resistance.

Scattering Matrix

The three JRM modes coupled to transmission lines represent an open quantum system. The scattering matrix of the JPC can be derived in the framework of input-output-theory. A comprehensive introduction is found in [45, 46]. Only the basic ideas are reproduced here. A transmission line is modelled as a continuous bath of harmonic oscillator modes. Each of them is coupled with equal strength κ to the resonator (Markov approximation). The bath is assumed to be sufficiently cold. This means, that, except for signals deliberately applied by the experimenter and with a known frequency, the transmission lines only introduce fluctuations and do not deposit energy in the resonators.

It is possible to define operators $a_{in}(t)$, $a_{in}^\dagger(t)$ and $a_{out}(t)$, $a_{out}^\dagger(t)$ that describe the incoming and outgoing fields, travelling along the transmission line towards or away from the resonator. To get an intuition, one should think of the connected observables, for example $\langle a_{in}^\dagger a_{in} \rangle$, not as a photon occupation number but more as a flux of photons travelling in direction of the resonator, or against it. A well written overview of travelling quantum signals is found in [47].

In order to determine the time evolution of the JRM modes a , b and c , one has to consider

the quantum Langevin equations

$$\begin{aligned}
 \dot{a}(t) &= [H, a(t)] - \kappa_a a(t) + \sqrt{\kappa_a} a_{in}(t) \\
 \dot{b}(t) &= [H, b(t)] - \kappa_b b(t) + \sqrt{\kappa_b} b_{in}(t) \\
 \dot{c}(t) &= [H, c(t)] - \kappa_c c(t) + \sqrt{\kappa_c} c_{in}(t)
 \end{aligned} \tag{71}$$

with $H = H_{\text{RWA}}^{\text{3-wave}}$ from eq. 70. They can be derived by looking at the Heisenberg equations of motion for each mode and the coupling to its bath (transmission line) individually [45]. Energy loss from the resonator modes into the bath is taken into account with a damping term proportional to $-\kappa$. Potential incoming fields are taken into account via the last term of each equation. Note that the coupling constant appears in the equation with different powers. This makes sense, as the travelling fields are defined in units of $\sqrt{\text{Hz}}$. In that way, expectation values of the travelling fields e.g. $\langle a_{in}^\dagger a_{in} \rangle$ end up in units of $\text{Hz} = \text{s}^{-1}$, representing a flux of photons. Incoming and outgoing fields in the transmission lines are related via the so-called input-output-relation [48]

$$a_{in}(t) + a_{out}(t) = \sqrt{\kappa_a} a(t). \tag{72}$$

When looking at the device's capability of performing parametric amplification, two incoming fields with frequency ω_1 and ω_2 at signal and idler port are considered. They are assumed to be resonant with the modes $\omega_1 = \omega_a$ and $\omega_2 = \omega_b$. The pump is assumed to be stiff, implying that there are sufficiently many photons in the mode for it not to get depleted through conversion of pump photons. This is modelled by replacing the operators c and c^\dagger with their expectation values $\sqrt{n_p} e^{i\omega_p t}$ oscillating with the pump frequency.

Given these assumptions, it is possible to solve the system of coupled differential equations 71 in terms of ingoing and outgoing fields, as shown in [47]. The final result

$$\begin{pmatrix} a_{out} \\ b_{out} \end{pmatrix} = \begin{pmatrix} \sqrt{G} & \sqrt{G-1} \\ \sqrt{G-1} & \sqrt{G} \end{pmatrix} \begin{pmatrix} a_{in} \\ b_{in} \end{pmatrix} \tag{73}$$

is the JPC scattering matrix with zero-detuning maximum gain G (a phase factor is omitted in the result). It is intuitive to rewrite the travelling fields as in-phase and out-of-phase quadratures

$$I_{in}^a = \frac{a_{in} + a_{in}^\dagger}{2} \tag{74}$$

and

$$Q_{in}^a = \frac{a_{in} - a_{in}^\dagger}{2i}. \tag{75}$$



Analogous definitions hold for the outgoing waves and the signals going in and out at the idler port. The advantage of the observables I and Q is, that they are directly accessible in the experiment via heterodyne detection. Rewriting the scattering matrix results

$$I_{out}^a = \sqrt{G}I_{in}^a + \sqrt{G-1}I_{in}^b \quad (76)$$

and

$$Q_{out}^a = \sqrt{G}Q_{in}^a - \sqrt{G-1}Q_{in}^b \quad (77)$$

for the quadrature fields coming out at the signal port (omitting another phase factor). For large gains $\sqrt{G-1} \approx \sqrt{G}$ predicts that the JPC essentially adds signal and idler amplitudes with power gain G . The JPC is a non-degenerate parametric amplifier (spatially separated signal and idler resonator) and performs phase-preserving amplification - both quadratures are amplified by the same gain.

When there is no input at the idler port $I_{in}^b = Q_{in}^b = 0$, eqns. 76 and 77 reduce to

$$\begin{pmatrix} I_{out}^a \\ Q_{out}^a \end{pmatrix} = \sqrt{G} \begin{pmatrix} I_{in}^a \\ Q_{in}^a \end{pmatrix} \quad (78)$$

and the JPC operates as a reflection amplifier - the incoming signal is amplified and reflected back into the same port. This is probably the most common application of a JPC. Fig. 24 shows the schematics of a JPC operated as reflection amplifier. The amplitude of

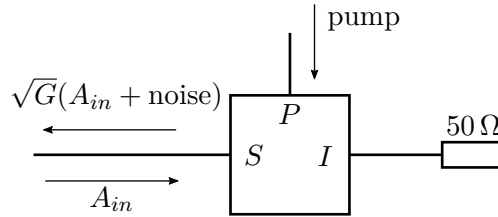


Figure 24: Schematics of a JPC operated as reflection amplifier. Signal, idler and pump ports are labelled S , I and P . An incoming signal with amplitude A_{in} is reflected by the JPC. The amplifier adds noise and amplifies with a (voltage) amplitude gain \sqrt{G} . The minimum amount of noise added by the JPC corresponds to half a photon at the signal frequency.

the incoming signal in terms of the quadratures reads $A_{in} = \sqrt{I_{in}^2 + Q_{in}^2}$. The idler port is terminated in a matched 50Ω resistor in order to dissipate the photons generated in the idler resonator. As indicated in the drawing, the JPC does not only provide amplification, but also adds noise to the output signal.

Added noise

The previous paragraph described the JPC operating as single-mode reflection amplifier. It is based on the assumption of having zero input fields at the idler port. This condition can never be completely satisfied. When the device is sufficiently cold $k_b T \ll \hbar \omega_b$ the idler resonators can be assumed to be in the ground state $\langle N_b \rangle = \langle b^\dagger b \rangle = 0$. However, the idler mode still exhibits vacuum-fluctuations corresponding to half a photon $\Delta N_b = \sqrt{\langle N_b^2 \rangle} = 1/2$. These fluctuations are converted to the signal port adding noise to the output signal. Thus, the JPC adds at least half a photon of noise to the amplified signal. This agrees with the minimum amount of noise that is added by any linear amplifier [49]. JPCs have been proven to operate close to the quantum limit, adding about 1 photon of noise [50]. The following consideration may help to provide an intuitive picture of the noise addition.

Let us assume an input signal corresponding to $N_{\text{in}}^{\text{sig}}$ photons in the signal resonator. $N_{\text{in}}^{\text{noise}}$ denotes the number of incoming noise photons. Input signal and fluctuations are converted by the JPC via

$$N_{\text{out}}^{\text{sig}} = G N_{\text{in}}^{\text{sig}} \quad (79)$$

and

$$N_{\text{out}}^{\text{noise}} = G \left(N_{\text{in}}^{\text{noise}} + N_{\text{add}}^{\text{noise}} \right). \quad (80)$$

As stated above, the smallest possible amount of added noise is $N_{\text{in}}^{\text{noise}} = 1/2$. Evaluating the signal-to-noise ratio

$$\text{SNR} = \frac{N_{\text{out}}^{\text{sig}}}{N_{\text{out}}^{\text{noise}}}. \quad (81)$$

at the input and the output of the JPC shows, that it actually decreases. This has to be true in general for any amplifier. However, using the JPC as first link in a chain of amplifiers can significantly increase the SNR of the total measurement chain. In a typical cryogenic experimental setup, the main task of the JPC is to overcome the noise of the subsequent HEMT amplifier.

Bandwidth and gain limitations

The JPC gain is maximal when the input signal is resonant with the signal resonator. Slightly detuned signals are amplified less. As derived in [42], the gain as a function of the detuning $\omega_1 - \omega_a$ has the shape of a Lorentzian

$$G(\omega_1) = \frac{\sqrt{G}}{\sqrt{1 + G \left(\frac{1}{\kappa_a} + \frac{1}{\kappa_b} \right)^2 (\omega_1 - \omega_a)^2}}. \quad (82)$$



The -3 dB bandwidth is

$$BW = \frac{B_0}{\sqrt{G}} \quad (83)$$

where

$$B_0 = \frac{2\kappa_a\kappa_b}{\kappa_a + \kappa_b}. \quad (84)$$

Typical dynamical bandwidths are on the order of 2 to 10 MHz for a gain of 20 dB [41]. However as signal and idler resonators are tunable, the JPC can be used over a far greater range. The gain center frequency can be shifted across a tunable bandwidth of a few 100 MHz.

As discussed in [41], the zero-detuning maximum gain depends on the pump power p_p via

$$\sqrt{G_0} = \frac{1 + p_0^2}{1 - p_0^2} \quad (85)$$

with the dimensionless pump power $p_0 = 2g_3\sqrt{n_p}/\sqrt{\kappa_a\kappa_b}$. The gain is expected to diverge at $p_0 = 1$, but in practise the gain remains finite and maxes out around 30 dB. However, when the JPC is operated with such high gains, higher order terms in the interaction Hamiltonian start to contribute. In the experiment, asymmetric gain curves and loss of the phase preserving amplification are typical signs of too strong pump powers.

Another practical limitation of the JPC is the dynamic range. It is stated in terms of the -1 dB compression point, which is defined at that input power, at which the amplification is reduced by 1 dB. A limiting factor of the JPC is depletion of the pump. Relaxing the condition of a stiff pump, the dynamic range can be estimated as is done in [43]. The result is not reproduced here. For the set of parameters chosen by the authors, the -1 dB compression point for a 20 dB gain lies around an input power of $p_{-1\text{dBm}} \approx -120$ dB. This calculated value agrees reasonably well with the dynamic ranges that were determined experimentally by the manufacturers of the JPCs. The main specifications of the JPCs SN004 and SN0010 are reproduced in the following section.

4.3 Specifications

The full specifications of the two JPCs SN004 and SN0010 are listed in [51] and [52]. The tunable range of the amplifiers is listed in table 4 and depicted schematically in fig. 25. For the JPC SN004 the dynamic bandwidth at a gain of 20 dB is stated as 7 MHz throughout the tunable range. The JPC SN0010's dynamic bandwidth varies between 4 and 10 MHz depending on the frequency. For both amplifiers, the -1 dB compression point ranges

	Signal		Idler	
	f_{\min}	f_{\max}	f_{\min}	f_{\max}
SN004	8.610	9.026	4.822	5.035
SN010	6.978	7.508	4.851	5.079

Table 4: Tunable range of the JPC’s. Frequencies are denoted in units of GHz. At the moment of writing this thesis, there is evidence of a shift of the tunable ranges towards lower frequencies due to aging of junctions.

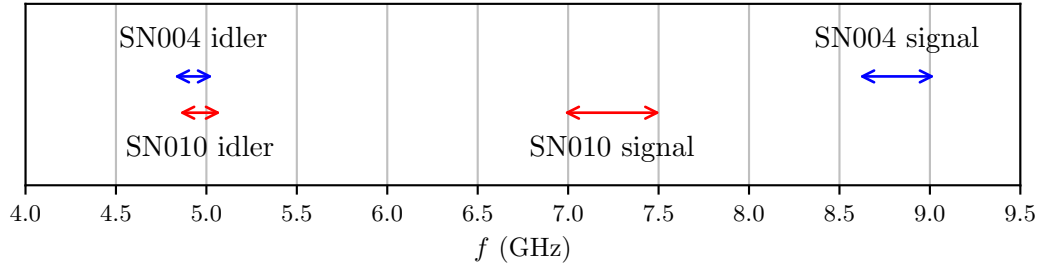


Figure 25: Tunable range of signal and idler resonator for the JPC’s SN004 and SN010 as specified in [51] and [52].

from -140 dBm to -120 dBm with a tendency of increasing towards higher gain center frequencies.

4.4 Testing the JPC SN004

In the scope of this project, both JPCs were tested on their basic functionality. Several parameters are relevant in the characterization of an amplifier. Gain, instantaneous bandwidth and tunable bandwidth are just as important as added noise and the dynamic range covered by the amplifier. In case of the JPC, many of these quantities influence each other in various ways. They also depend significantly on the actual setting of the bias current and the pump. An impressive example was demonstrated in 2017 by the Hatridge group [53]. Operating the JPC in a certain way can enhance the dynamic range by almost 5 dB or result in strong non-linear gains for signal powers close to the -1 dB compression point.

The JPC SN010 was tested once, with the conclusion of being tunable over its whole range and producing a stable gain. As the JPC SN004 was used to realize the dispersive readout scheme, it was tested thoroughly over a wide range of parameters. The key results are presented in the following section. Analysis of the gain profiles was done by fitting a



Lorentzian profile to the linear response as measured with a VNA. The gain, its center frequency and the -3 dB bandwidth are obtained from the fit parameters. An exemplary gain profile with fit function is shown in fig 26. Gain and -3 dB bandwidth are determined

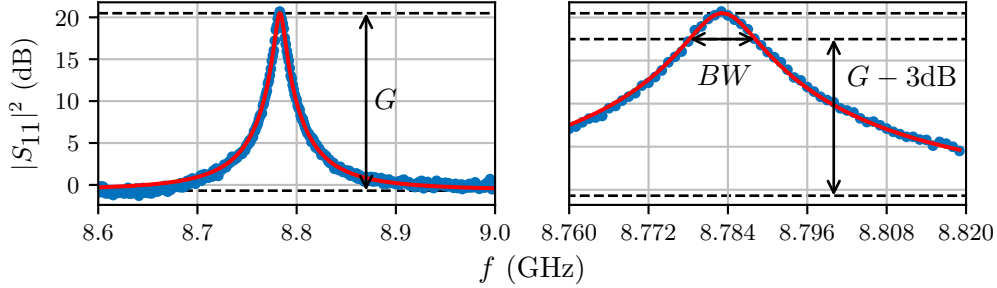


Figure 26: Typical gain curve of the JPC, measured with a VNA. The background (same measurement while the JPC is off) is subtracted. The amplification curve is characterized by the gain G , the gain center frequency f_G and the -3 dB-bandwidth BW . The parameters are determined with a Lorentzian fit of the linearized data. **Left:** JPC response over a range of 400 MHz (blue) and Lorentzian fit (red). In this example, the maximum gain amounts to $G = 20.49(1)$ dB. **Right:** Enlarged section of the same data, illustrating the -3 dB-bandwidth $BW = 9.80(1)$ MHz.

by fitting a Lorentzian profile to the linearized data. 3 dB correspond to a factor of 50% of the maximum gain.

4.4.1 Tunable Range

Examining the full tunable range of the JPC SN004 provided some interesting insights. In order to verify the specified range, the JPC was set up at a stable gain of 10 dB with different central frequencies roughly 100 MHz apart (8.7 GHz was left out undeliberately). The data is shown in fig. 27. The 20 dB gain at 9.0 GHz falls out of line apparently. In fact, in May 2018 when this measurement was performed, the typical linear dependence of the gain on the pump power could not be reproduced at that frequency. Altering the pump power would only shift the 9 GHz peak sideways and further increase its asymmetry. The possibility to produce a gain at 8.4 GHz presents another deviation from the specifications, as nominally the JPC is roughly tunable from 8.5 GHz to 9 GHz. A possible explanation for both of these observations is aging of the Josephson-Junctions comprising the main circuit of the JPC. More than two years have passed since the device was fabricated and since then it has endured more than ten cycles of warming up and cooling down again. Junction aging typically results in higher Josephson-inductances, lowering the frequency of

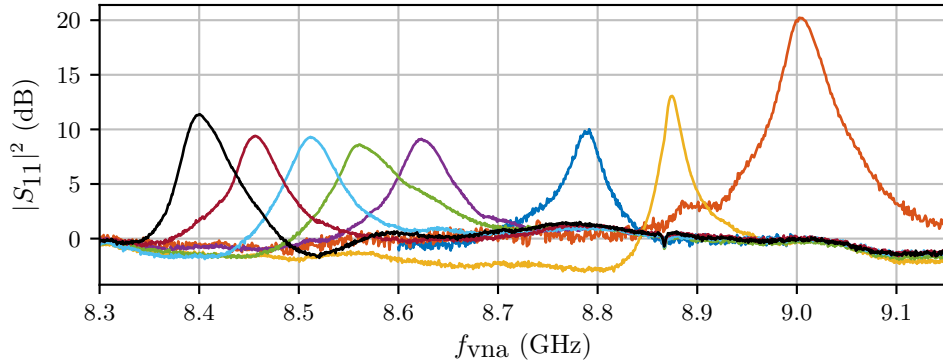


Figure 27: Snapshots of gain profiles while exploring the specified range of the JPC SN004. Setting up a gain at 9.0 GHz turned out difficult and the typical linear response to changes in the pump power could not be observed. On the other hand, a stable gain at 8.4 GHz was readily achievable. The JPC’s linear operating range appears to have shifted towards lower frequencies by about 100 MHz. The suspected reason is the aging of the circuit’s Josephson junctions.

the resonators. It seems likely, that the operating range of the signal resonator has shifted down to lower frequencies by about 100 MHz. Presumably the idler was similarly effected by the aging. In case of future problems with the choice of the right pump frequency, it might be reasonable to invest the time and take a full fluxmap of both resonators.

4.4.2 Gain vs. Pump Power

The JPC gain is highly sensitive to changes in the pump power. Fig. 28 shows a collection of JPC response functions with different pump powers. The sensitivity on pump power increases towards higher gains. A stronger pump not only increases the gain, but also shifts it to lower frequencies. According to eq. 85, the gain is expected to diverge at when the pump reaches a certain critical power value. In reality, the assumption of a perfectly stiff (undepletable) pump breaks down and the gain saturates at a certain value. Also, the Josephson-Junction based resonators can only sustain a limit amount of excitation, as their superconductivity breaks down when exposed to currents larger than their critical currents I_c . Gains as high as 35 dB were observed while testing the amplifier. In terms of SNR improvement, it is recommended to operate the JPC at a gain of approximately 20 dB (see sec. 4.4.5). Clearly, the dynamical bandwidth of the JPC decreases with increasing gain. As stated in eq. 83, a constant product of bandwidth and amplitude gain

$$BW \times \sqrt{G} = \text{const.} \quad (86)$$

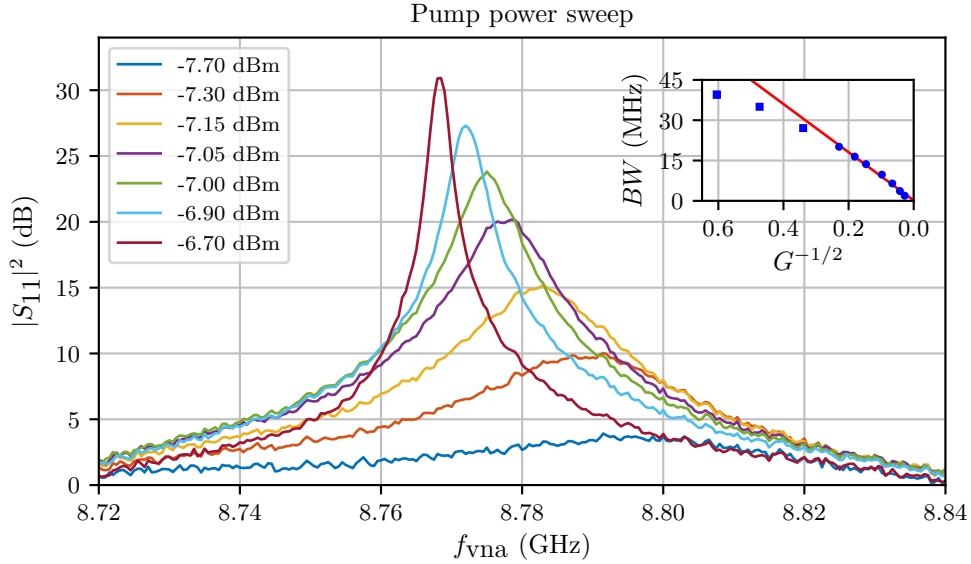


Figure 28: JPC pump power sweep. 1 dB of pump power can change the gain by as much as 25 dB and shift the center frequency by more than 20 MHz. Measured with the VNA at low probe powers of approximately -135 dBm. **Inset:** For high gains (low $G^{1/2}$), a constant gain bandwidth product is expected. This is the case for gains above 10 dB. The linear fit (red) is based on the section of the data plotted with blue dots.

is expected at high gains. The inset of fig. 28 shows, that the prediction fits quite well for gains larger than 10 dB (corresponding to $1/\sqrt{G} \approx 0.4$). Lower gains are indicated with blue squares (instead of dots).

4.4.3 Gain vs. Pump Frequency

For a fixed setting of the bias current, the JPC central gain frequency can be tuned by varying the frequency of the pump. This is done by altering the pump frequency by about 5 to 10 MHz and resweeping the power from low to high. The maximum achievable gain differs with pump frequency. Fig. 29 shows a series of JPC response curves with different pump settings and fixed bias current. A range of 50 MHz with a gain of 20 dB can be easily covered with this method. It is stated as a rule of thumb in [51], that the gain center frequency is expected to shift by half of the change in pump frequency. However, I did not find this immediately apparent in my experiments.

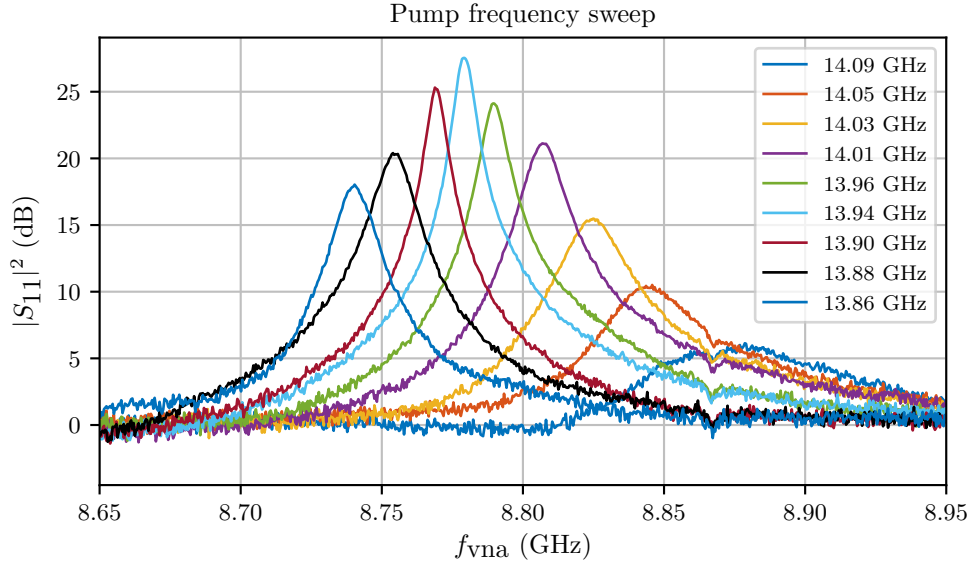


Figure 29: JPC gain curves for fixed bias current and variable pump frequencies. The pump power is optimized for each frequency. This method allows to fine tune the position of the gain curve without altering the bias current. Data was taken with a JPC set up behind a cavity-qubit system. The cavity is visible in the data as a dip around 8.86 GHz.

4.4.4 Gain vs. Signal Power

In the linear regime, the gain of an amplifier is independent of input signal strength. As with any other amplifier, the JPC's ability to perform linear amplification is limited to a certain maximum input power. Higher input levels cause the device to saturate, resulting in a reduced gain and a deviation of the symmetric Lorentzian profile. The distortion of the response is illustrated in fig. 30. Saturation effects appear as soon as the input power exceeds -130 dB and the maximum gain starts to decrease. The 1 dB compression point lies at an approximate input power of -125 dB for a small signal gain of 23 dB. This result is slightly below the nominal value of -135 dB for a 20 dB gain at 8.8 GHz [51]. The deviation is probably due to the higher gain that was used when measuring the signal power sweep. Also, the accuracy of the estimate on the 1 dB compression point is limited by the uncertainty of the power calibration (see eq. 55).

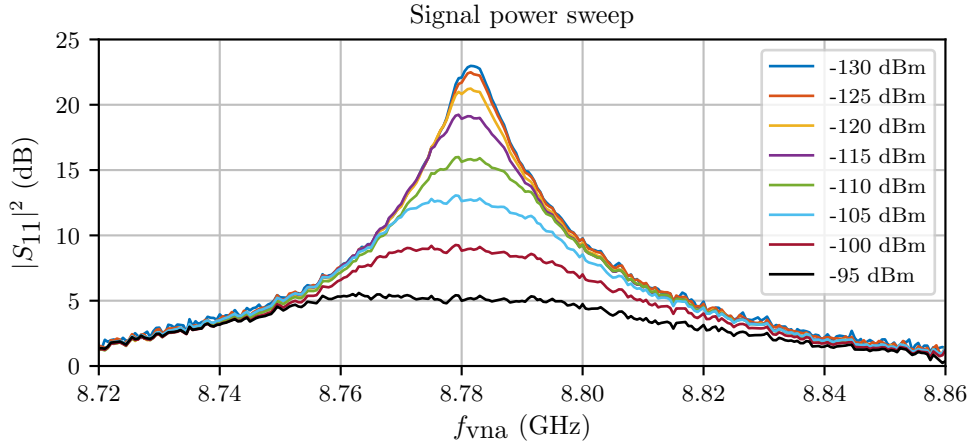


Figure 30: JPC gain curve sweep for different input signal powers. Saturation effects appear at input powers above -130 dB. The amplification is reduced and the Lorentzian profile of the gain curve is distorted.

4.4.5 SNR Improvement

When looking for a low-noise RF amplifier that can be used in cryogenic environments, the first choice are high electron mobility transistors (HEMTs). When operated at 4 K, these devices achieve gains of more than 40 dB over a broad range of up to 10 GHz while only adding noise corresponding to a temperature of less than 4 K. This equivalent noise temperature is defined as

$$S = k_B T_e \quad (87)$$

with the Boltzmann constant k_B and the noise power spectral density S in units of W/Hz. It allows to describe a noisy amplifier with the equivalent circuit of a perfect amplifier in series with a thermal noise source of temperature T_e . Note that the noise temperature of a device does not coincide with its actual temperature. Comparing the energies

$$k_B T_e = \hbar \omega N \quad (88)$$

the noise temperature can be expressed as number of noise photons N at frequency ω . Therefore, the effective noise temperature of half a photon at 8.8 GHz is roughly 80 mK. A real JPC, adding several photons of noise, still greatly outperforms a HEMT in terms of noisiness.

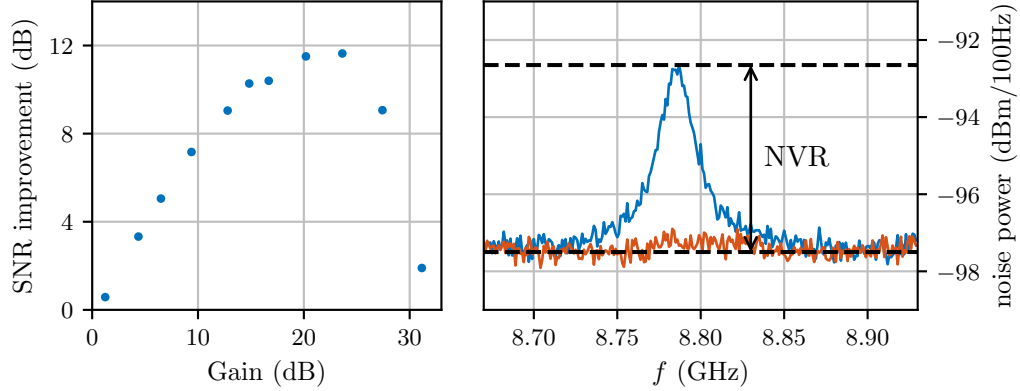


Figure 31: **Left:** SNR improvement vs. JPC gain. Highest improvement is achieved at a gain of 20 dB. **Right:** Noise spectra with JPC on (blue) and off (orange). The noise visibility ratio NVR is defined as the difference between the noise floor and the maximum of the noise added by the JPC.

In a chain of two amplifiers ‘1’ and ‘2’ the effective noise temperatures propagates as [26]

$$T_e = T_1 + \frac{T_2}{G_1}. \quad (89)$$

The noise added by the second amplifier is reduced by the gain of the first one. Thus, the total signal-to-noise ratio of the measurement chain can be enhanced by using a JPC as pre-amplifier in front of a HEMT. The improvement can be quantified as the ratio

$$\text{SNR improvement} = \frac{G}{\text{NVR}}, \quad (90)$$

between JPC gain and the noise-visibility-ratio NVR. The latter is defined as

$$\text{NVR} = \frac{GT_{JPC} + T_{sys}}{T_{sys}}, \quad (91)$$

comparing the noise at the end of the measurement chain with the JPC turned on and off. T_{sys} describes the total noise temperature of the system including the HEMT. The exact values of system and JPC noise T_{sys} and T_{JPC} are difficult to measure. A thermal noise source with definite temperature would be needed as a reference [50]. However, the NVR is comparatively simple to determine. It is reflected in the difference (in dB) of the noise spectra at the output port when the JPC is turned on and off. No input signal is applied. The noise spectra are taken with a spectrum analyser. Two traces are shown in

fig. 31 (right) for a JPC gain of 12 dB. Clearly the spectral noise power goes up when the JPC is turned on. But as long as the total gain exceeds the added noise the total SNR increases. The SNR improvement for different gains is shown in fig. 31 (left). According to the data, the ‘optimal’ operation point with maximum benefit in SNR improvement is around 20 dB. Working with higher gains seems not advisable, as the improvement actually decreases again. The findings match well with the results given in [41].

4.5 Tuning Procedure

This section describes how to set up and tune the JPC. The tuning procedure is organised in step ‘1’ (setting the DC bias current) and step ‘2’ (frequency and power of pump signal generator). The tuning process typically requires a few iterations, going back from step ‘2’ to ‘1’, if the gain profile is distorted or not centred at the desired frequency. To get a quick overview, or as a reminder for experienced users, the tuning procedure is briefly summarized in the following section 4.5.1. Step ‘1’ and ‘2’ are elaborated in more detail in sec. 4.5.2 and 4.5.3. As a reflection amplifier, the JPC is usually used in connection with a circulator. A typical experimental configuration is shown in fig. 37.

4.5.1 In Short

0. Choose a target frequency ω_s

1. Tune the JPC’s signal resonator

by adjusting the coil current. The position of the resonance is best visible in the phase response, measured with a VNA. The resonator should be a few tens of MHz above the target frequency, as the pump will shift it downwards eventually. Amplification only works on **large lobes** of the signal resonator (compare fig. 33).

2. Turn on the pump

The pump frequency for a given target frequency can be found in the tables provided by the manufacturer. Turn on the pump and slowly increase the power in steps of 1 dBm starting from the lowest possible output power. Monitor both phase and amplitude response of the signal resonator on the VNA (2 traces). As the power increases, the resonance begins to shift towards the target frequency. At some point, the gain should appear in the amplitude. Try to optimise it by adjusting the power in steps of 0.1 dBm or smaller. If the position of the gain does not meet the desired target frequency, try pushing the position of the signal resonance (look at the phase) by adjusting the pump frequency in steps of ~ 5 MHz. If the gain is lost, try to recover it by turning off the pump and slowly bringing it back, starting from low power. The JPC is well set, when the gain is approximately symmetric and the gain varies linearly with (small) changes in the pump power, without drastic changes in shape and position. Keep in mind, that the JPC is easily saturated and only provides linear amplification of signals with powers not exceeding -110 dBm, corresponding to a few tens of photons per resonator bandwidth. The VNA output power has to be

chosen accordingly. If no stable gain can be achieved at the desired frequency, one has to go back to step ‘1’ and start over with an adjusted bias current (turn off the pump at this point).

4.5.2 Step 1: Setting the Bias Current

Both the JPC’s signal and idler resonator are flux-tunable. The magnetic flux is provided by a coil that is positioned right below the circuit board and addresses both resonators at the same time. An external current source provides the bias current. The connection from the base stage, where the JPC is located, to the top of the cryostat is formed by superconducting DC-looms. The loom is connected to each stage of the cryostat via pass-throughs, ensuring thermalization. An adapter at the top of the cryostat connects to a shielded BNC cable, that is connected to the current source with an additional 50 Hz lowpass filter. This setup has proven successful in minimizing noise in the bias line, allowing for a stable operation of the JPC. In the early stage of the experiment, an unexpected oscillatory behaviour was observed in the output of the current source (measured with an oscilloscope connected in parallel to the source and the JPC). The oscillations could be eliminated by adding a resistive element in series to the current line (connecting a $50\ \Omega$ resistor to the BNC cable actually). In retrospect, the oscillations were most likely caused by an improper grounding of the cryostat and the connected instruments. The overall noise performance was considerably improved by taking a number of steps. In order to avoid potential ground loops, the cryostat was grounded with a definite ground line with a diameter of 6 mm to the main ground of the building. Externally connected current and voltage sources are set to floating mode and any RF connection to the cryostat has to have an inner and outer DC block. Replacing the power supplies of the HEMT by voltage sources was a further improvement.

The easiest way to determine the position of the resonators is to measure the phase response with a VNA. A wide range of $\sim 2\ \text{GHz}$ that covers the whole range of the resonator is recommended. The 2π phase-shift of the resonator should become visible on the VNA-display after setting the right value for the electrical delay (on the order of 60 ns to 100 ns for 6 metres of blue *minicircuits* cables) and changing the mode to ‘expanded phase’. Additional features might appear in the spectrum if the JPC is placed in the same line as an experiment. However, the JPC resonator is easily identified by making small changes of typically a few $10\ \mu\text{A}$ in the bias current. The position of the resonance should begin to move. Fig. 32 shows the phase response of the JPC SN004’s signal resonator for different

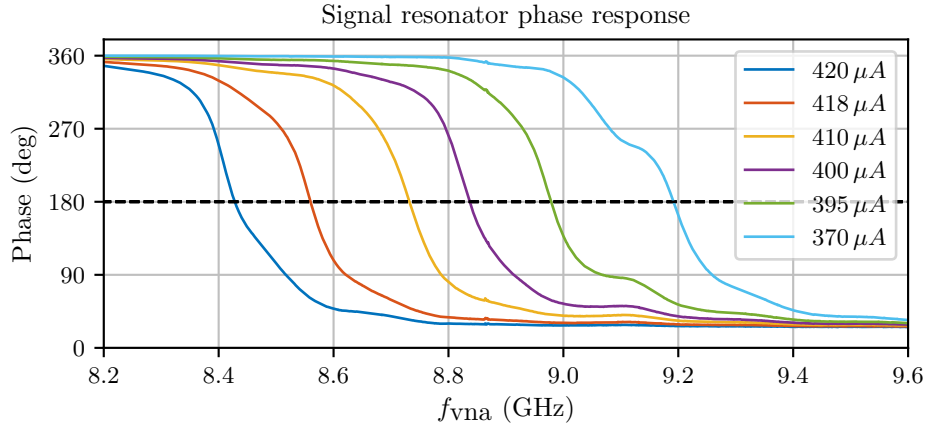


Figure 32: Tuning the signal resonator of the JPC SN004. Phase response for different bias currents, measured with a VNA. The JPC was placed in line with a cavity, which has been calibrated out. It is still visible slightly below 8.9 GHz.

bias currents. At the lower end of the JPC’s frequency range, the resonator is a great deal more sensitive on changes in the bias current. Note how a change of $2\ \mu\text{A}$ causes a shift of more than 100 MHz. Consequently, the JPC is more susceptible to flux noise (and bias current noise) when operated at the lower end of its range.

The position of the resonators is a periodic function of the flux. With our current setup, a full period corresponds to a change in bias current of a little less than 2 mA. Fig. 33 shows a fluxmap of the resonator, where each column corresponds to a VNA phase measurement as described above, but with a the bias current changed by $2\ \mu\text{A}$ per step. When the device is cooled down and becomes superconducting, the magnetic flux through the circuit’s loops is trapped due to flux quantization. It remains constant until the device gets sufficiently warmed up to reach the normal conducting phase. As a consequence, the distribution is hardly ever centred around 0 current.

During one period, the resonator frequency increases and decreases twice in the form of a small and a large lobe. The lobes are separated by unstable regions. Amplification is possible only at the sides of the large lobes. It is not enough to only tune the resonator to the desired frequency. One always has to make sure to be in a bias region where the JPC can actually produce a significant gain. The simplest method to relate the applied bias current to the actual flux through the device is to measure a fluxmap as shown in fig. 33. A rough map of around 50 current steps per period is usually sufficient. The more experienced user can try to manually alter the bias current in steps of $10\ \mu\text{A}$ over a whole period. Monitoring the position of the resonator on the VNA and following the resonance



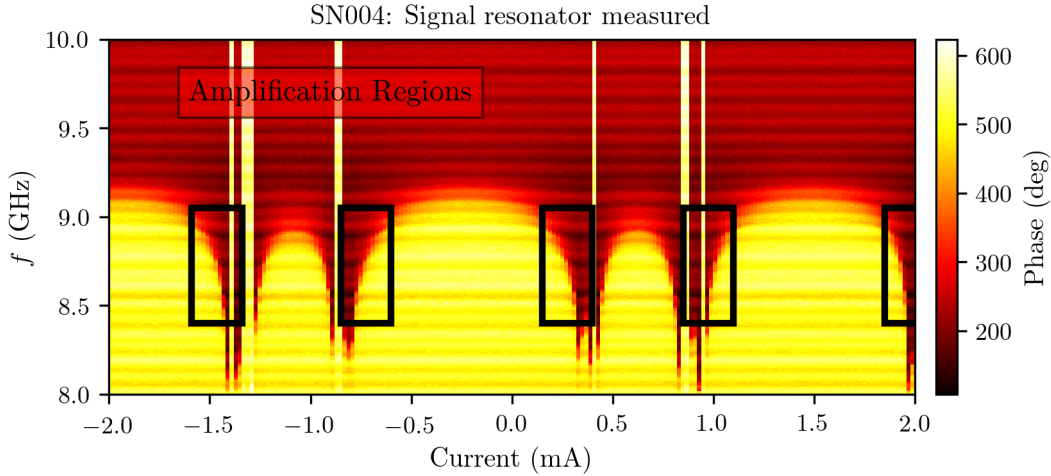


Figure 33: Measured fluxmap of the signal resonator of the **JPC SN004**. Amplification is only possible on the side of the large lobes marked in blue. The offset in the bias current is different each time the JPC is cooled down. It reflects the trapped flux in the Josephson ring modulator (JRM).

allows to distinguish between small and large lobes.

Let us assume one wants to amplify a signal with target frequency $\omega_s = 2\pi \times 8.8$ GHz. The resonator has to be tuned roughly 100 MHz above ω_s , as powering up the pump will push the resonance down to lower frequencies.

4.5.3 Step 2: The Pump

The signal generator providing the pump signal is connected without additional attenuation to the top of the cryostat. A total of -50 dB of attenuators are placed inside the cryostat. Typical pump powers at the generator output range from -15 dBm to 5 dBm. The correct pump frequency is determined as the sum of signal and idler resonance frequency at a given bias current. In most practical cases, only one of the resonators is connected to an output line and there is no way to actually measure the position of both resonators at the same time. However, the required information is provided in the data sheets. Figure 34 shows the fluxmap measured by the manufacturer for the JPCs SN004. The reference data for the JPC SN010 is found in fig. 64 in the appendix. The actual values of the current offset and the length of a period in units of electric current are not important - they depend on the trapped flux and the specific measurement setup. What is important, is the fact

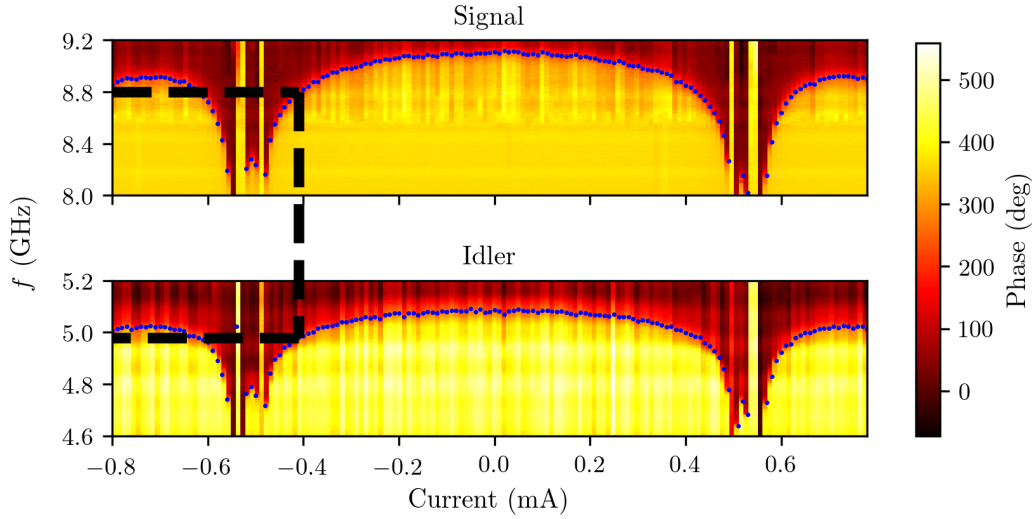


Figure 34: Excerpt of the **JPC SN004** reference fluxmaps as provided by the manufacturer. The full data is found in the users guide [51]. The pump frequency for a given target frequency is the sum of signal and idler frequency at that bias current. With the JPC SN004 a pump at 13.8 GHz can be used to either produce a gain centred at ~ 8.8 GHz with the signal resonator or at ~ 5 GHz using the idler resonator. The connection is indicated by the black dashed line. Resonance frequencies are determined by fitting an arctangent to the phase response (blue dots).

that both signal and idler resonator are coupled to the bias flux in the exact same way. They have the same periodicity and offset. This allows to extract a good starting value for the pump frequency ω_p from the reference data shown in the figures. For a given target frequency ω_s , the corresponding bias current of the signal resonator can be simply read off from the graph. The fluxmap of the idler resonator shows the frequency of the idler at that specific bias. The way the choice of a bias current determines both signal and idler frequency is indicated with black dashed lines in the graph in fig. 34.

Let us get back to the example of amplifying a $\omega_s = 8.8$ GHz signal. In order to produce a gain centred at ω_s the pump is set to $\omega_s + \omega_i = 13.8$ GHz. It has proven to be extremely helpful, to monitor both the phase and the amplitude of the JPC response with a VNA, while setting up the amplifier. This is done by activating two traces in the menu of the VNA and setting them to ‘log mag’ and ‘expanded phase’. Remember to add the right electrical delay in the ‘measure’ tab in order to display the phase in a meaningful way. To avoid saturation effects in the amplifier, the power at the input port of the JPC should not exceed -110 dBm. For a first try, the JPC’s signal resonator is tuned to ~ 8.9 GHz, which is 100 MHz higher than the target frequency ω_s . The process of gradually turning



on the pump is shown in fig. 35. Phase and amplitude are displayed separately in blue and red. The generator of the pump signal should be set to its minimal power output before turning it on. If activating the pump drastically changes the spectrum on the VNA, the pump power is already too high and additional attenuation is needed in the line. Slowly increasing the power in steps of 1 dB, the resonator begins to shift towards lower

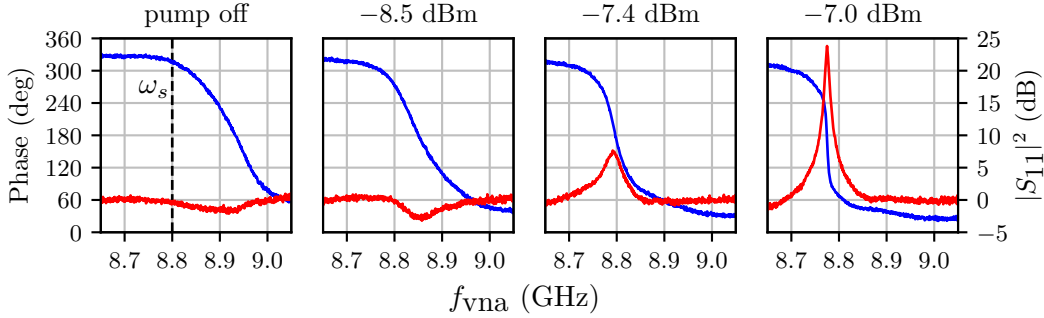


Figure 35: Turning on the pump. Phase (blue) and magnitude (red) of a VNA reflection measurement of the JPC. The resonator is initially tuned to about 8.9 GHz as seen in the leftmost graph. The pump is set to 13.8 GHz in order to amplify a signal at $\omega_s = 8.8$ GHz. Activating the pump and slowly increasing its power shifts the resonator to lower frequencies (left to right picture). When the gain appears in the magnitude, it can be optimized by adjusting the pump power in small steps of less than 0.1 dB. In this example the gain center frequency appears slightly below ω_s . The position can be changed by varying the pump frequency or changing the bias current. Both methods require the pump to be reset and re-swept from low to high power.

frequencies. When reaching a certain power, the gain appears in the amplitude. From here on the pump power should be adjusted in steps of 0.1 dB or even 0.01 dB trying to optimize the profile of the gain. A stable gain is characterized by a (relatively) symmetric gain curve that does not fluctuate. In that particular example, the gain lies slightly below the desired frequency ω_s . Small changes of the gain center frequency can be achieved by altering the pump frequency in steps of 5 MHz and re-sweeping the pump power from low to high. If the desired frequency cannot be reached that way, the pump has to be turned off and the tuning procedure repeated at a different current bias.

It is not beneficial to operate the JPC with an amplification of more than 20 dB, as there is typically no improvement in signal-to-noise-ratio beyond that point. Also, a strongly driven JPC can squeeze an incoming signal and amplify its quadratures differently. A closer analysis of these topics and the JPC's performance for various pump powers, pump frequencies and signal powers is presented in the next section.

5 Observing Quantum Jumps

5.1 Overview

As discussed in chapter 2.3.2, the quantum state of a transmon in a cavity can be determined via dispersively probing the cavity. In this experiment, the transmon state was monitored by means of continuously probing the cavity. After interacting with the system, this continuous probe beam is split into small parts. Each part is digitally processed resulting in one data point, representing the state of the transmon at that time. Using the JPC, this measurement can be done on the same timescale or even faster than the thermal transition rate of the system. The transitions or ‘quantum jumps’ are resolved in time and can be directly observed. Below follows a short recapitulation of the dispersive readout scheme with focus on the experimental realisation.

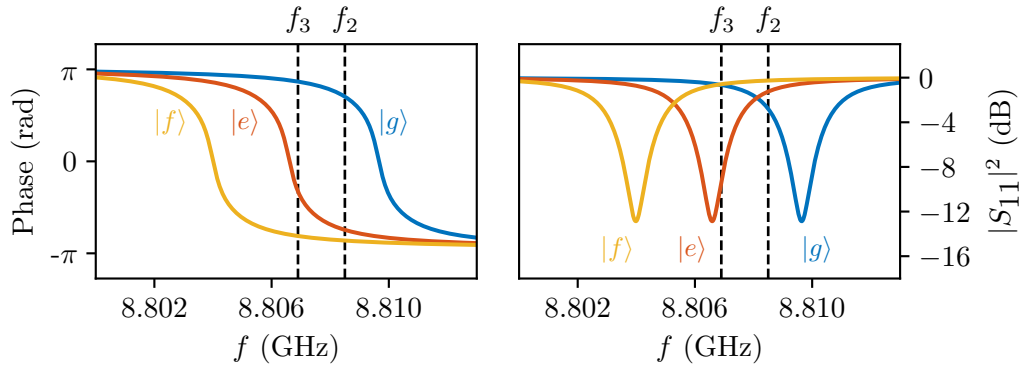


Figure 36: Calculated cavity phase (**left**) and amplitude (**right**) response for the transmon states $|g\rangle$, $|e\rangle$ and $|f\rangle$. Only the ground state cavity response can be measured accurately, see fig. 14. This result is numerically reproduced at the shifted cavity frequencies f_c^e and f_c^f that correspond to the excited transmon levels. Frequencies of the probe beams f_2 and f_3 are indicated with dashed black lines. Probing at f_2 allows to clearly identify the ground state as all the higher levels add a very different phase shift. A probe at f_3 can distinguish all three of the transmon’s states as they are well separated in phase.

In the regime of dispersive coupling, the transmon state is encoded in the position of the cavity resonance frequency. The problem of determining the transmon state reduces to the problem of finding the cavity resonance. This can be done by irradiating the cavity with a probe beam and recording the outgoing signal. Information about the state of the transmon gets imprinted in phase and amplitude of the reflected probe beam. Depending on the probe frequency, the dispersive readout is sensitive to different transmon states. The



following consideration helps to gain intuition about what to expect from the dispersive measurements of this specific system. Quality factors Q_{int} and Q_c are known from the low power cavity measurement (see fig. 14). Tab. 3 lists the measured cavity positions f_c^g , f_c^e and f_c^f for the three lowest transmon states. Fig. 36 shows a numeric reproduction (using eq. 34) of the low power cavity response at this frequencies, assuming no change in the quality factors. Expected amplitudes and phases for various probe frequencies can be estimated from this graph. Two main readout schemes have been used in this project. The different probe frequencies f_2 and f_3 are indicated in the graph.

	$ g\rangle$	$ e\rangle$	$ f\rangle$
Phase	0	264°	285°
Amplitude	75 %	90 %	100 %

Table 5: Expected phases and relative voltage amplitudes when probing at f_2 , extracted from the graph in fig. 36.

When probing at $f_2 = 8.8085$ GHz, two distinct measurement results are possible. They correspond to ‘transmon is in ground state’ and ‘transmon is not in ground state’. Choosing f_2 slightly above $(f_c^g + f_c^e)/2$ ensures, that e and f result in almost the same phase shift. As a consequence, the ground state is clearly distinguished from the higher levels. Two disks are visible in the IQ-plane, as shown in sec. 5.5. Expected phase shifts and amplitudes as derived from fig. 36 are listed in tab. 5.

A probe frequency close to the excited state resonance f_c^e allows to distinguish three transmon states. Probing exactly on resonance leads to a very low amplitude of the e state results. The contrast is increased by using a slightly higher value of $f_3 = 8.8085$ GHz. At this frequency, the power magnitude $|S_{11}|^2$ is still about -8 dB lower compared to the g and f state results. This corresponds to a voltage magnitude $|S_{11}|$ of -4 dB or 40 %. As seen in fig. 36, the three states g , e and f imprint a clearly distinct phase shift on the probe signal. Tab. 6 summarizes the expected phases and amplitudes for the three-state probe frequency f_3 . With a value of about 300° , the phase separation between g and f state is alarmingly close to a full circle. We succeeded in engineering the system close to

	$ g\rangle$	$ e\rangle$	$ f\rangle$
Phase	0	217°	305°
Amplitude	99 %	40 %	100 %

Table 6: Expected phases and relative voltage amplitudes when probing at f_3 , extracted from the graph in fig. 36.

the optimal readout configuration of $\kappa = \chi$ [18]. However, due to the ill-chosen second pin, the cavity ended up being almost critically coupled instead of over-coupled. Therefore the cavity's phase response looks different than a simple arctangent with FWHM f_r/Q_l (see sec. 2.3.1) and a loss of contrast has to be anticipated.

5.2 Experimental Setup

A schematic diagram of experimental setup is shown in fig. 37. The 4 K and 20 mK stage of the cryostat are indicated with dashed lines. The experiment required three RF input lines: one for the probe signal, one for driving the qubit and one pump as energy supply for the JPC. All RF input lines are connected to the cryostat via DC blocks in order to break ground loops. The input signals are attenuated at each temperature stage. This helps to have clear input signals in two ways. Firstly, the attenuators damp out the outside noise originating from room temperature cables and generators. Attenuation of the input signal is compensated by using accordingly high powers at the generator output. Secondly, the attenuators ensure a thermal connection between the lines and the cryostat. Well thermalized cables minimize the thermal noise and the heat power delivered to the experiment at the base stage. One signal generator provides the pump for the JPC. Two generators 'Transmon drives' are used to drive the transmon. The signals are added in a power combiner and sent to the 'in' port of the cavity, which is coupled very weakly compared to the 'out' port. Still, the coupling is sufficient for the drives to interact with the transmon. The third input line is used as main input of the probe signal. It is labelled with 'signal in'. After passing input filters and attenuators, the signal is routed to the cavity out port via a circulator. The cavity's output port is coupled a lot stronger than the input port. Therefore, it is safe to assume that after interacting with the cavity, the field is reflected back to the circulator. From there, the signal is directed to the JPC, where it is amplified and reflected once more. On the way out of the cryostat, the signal is filtered with a 12 GHz low-pass and amplified with a HEMT. Two isolators protect the JPC and the sample from interfering signals from outside. An isolator consists of a circulator with one of its ports terminated in a $50\ \Omega$ load. It serves as a optical diode, transmitting losslessly in one direction and providing an attenuation of $-20\ \text{dB}$ in the other. A DC block protects the HEMT from static discharges. This component should never be left out as the HEMT input stage is very sensitive and blows easily. Replacement is expensive and tedious.

When performing IQ-measurements the output signal is mixed down to an intermediate



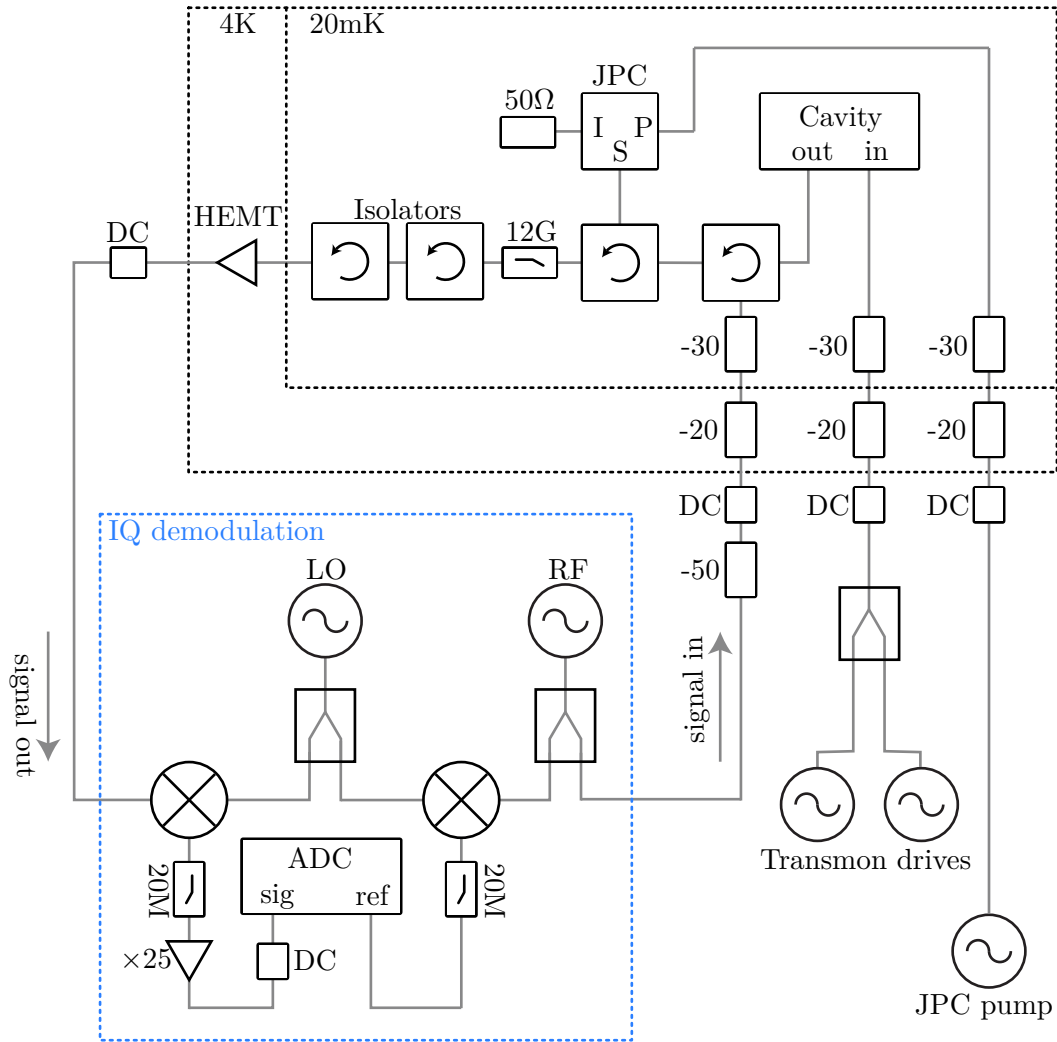


Figure 37: Experimental setup. RF signal paths are drawn in grey, electronic components in black. The IQ acquisition setup is indicated in blue. When performing spectroscopic measurements, this part of the setup is replaced by a VNA. Full description in the main text.

frequency. Signal and reference are separately recorded with a 2 channel analogue to digital converter (ADC) board. The down mixed signal is amplified further with a voltage gain of a factor of 25 in order to utilize the full dynamic range of the acquisition board. For the same reason, a -50 dB attenuator is placed as first element in the signal's input path. It allows to set the RF signal generator to macroscopic powers (0 dB to 20 dB), ensuring a strong reference signal at the ADC input port while at the same time sending the desired weak signal into the cryostat. The part of the setup that is responsible for the IQ-demodulation is marked with a blue dashed box. It is described in more detail in the following section. The setup shown here was slightly modified for some of the experiments. For example, the cavity characterisation measurements presented in section 3.1 did not require the IQ-demodulation circuit. Instead, 'signal in' and 'signal out' were simply connected to a VNA.

For the sake of clarity, a few components are not shown in the wiring diagram. These include the current source and connection to the JPC bias coil via a superconducting DC loom. All the signal generators are connected to a common frequency standard to ensure phase and frequency stability. Power supplies are also excluded.

5.3 Heterodyne Detection

The cavity is probed continuously with a probe beam at frequency $\omega_p = 2\pi f_p$. Changes in amplitude and phase of the reflected signal can be efficiently determined via heterodyne detection. In this method the probe is split up into two parts - signal and reference. The signal passes through the experiment, whereas the reference runs in a separate undisturbed path. Subsequent comparison of the two allows to decompose the signal into its quadrature components I and Q . This method of detection is very sensitive to changes that appear during the signal path.

Performing a heterodyne measurement in the GHz regime using only analogue electronics is technically very demanding. The challenge is simplified by using a combination of analogue and digital signal processing techniques. In this experiment, signal and reference are both mixed down to an intermediate frequency that can be readily recorded with an analogue to digital converter (ADC). The actual IQ demodulation is done digitally after acquisition. Analogue and digital part of the signal processing are described below.



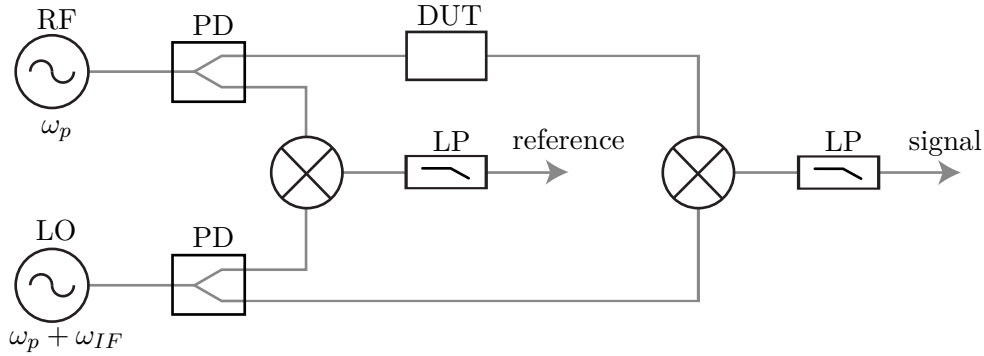


Figure 38: Heterodyne detection setup. Changes in amplitude and phase of the signal are detected via comparison to a reference. Both signal and reference are down-converted to an intermediate frequency ω_{IF} . This is done by mixing the probe signal (RF) oscillating at ω_p with a local oscillator (LO) running at $\omega_p + \omega_{IF}$. A low pass filter damps out the fast oscillating component, leaving behind the desired intermediate frequency. Down-converted signal and reference are recorded with a 2-channel ADC (not shown).

5.3.1 Analogue Down Conversion

Both signal and reference are down-converted to an intermediate frequency $\omega_{IF} = 2\pi \times 12.5$ MHz that can be resolved easily with an ADC. The conversion requires two signal generators. The first one (RF) is set to the probe frequency ω_p . The ‘local oscillator’ (LO) is operated at $\omega_p + \omega_{IF}$. Both signals are split up right after generation with power dividers (PD). One path of the RF signal passes through the ‘device under test’ (DUT). After traversing the experiment, it is mixed with the LO signal. The mixer multiplies its inputs, producing an output signal with components oscillating at the sum $\omega_p + \omega_{IF} + \omega_p$ and difference $\omega_p + \omega_{IF} - \omega_p$ frequencies. A subsequent 20 MHz low-pass filter suppresses the fast oscillating part, leaving behind the main signal with the intermediate frequency ω_{IF} . The reference is obtained in the same way by mixing LO and RF right after generation.

The down-converted reference and signal can be written as

$$\text{ref}_0(t) = A_{\text{ref}} \cos(\omega_{IF}t + \theta_{\text{ref}}) \quad (92)$$

and

$$\text{sig}(t) = A_{\text{sig}}(t) \cos(\omega_{IF}t + \theta_{\text{sig}}(t)) \quad (93)$$

both oscillating at the intermediate frequency. The reference amplitude A_{ref} is constant. The same goes for the phase, which can be set to $\theta_{\text{ref}} = 0$ without loss of generality. Signal

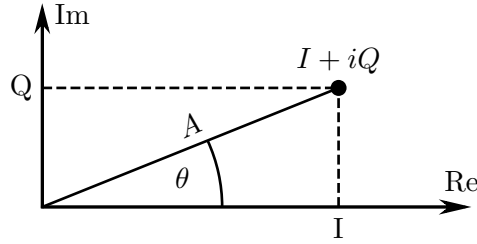


Figure 39: Signal depicted in the IQ plane. A signal with known frequency can be equivalently described either via amplitude and phase or via quadratures I and Q .

amplitude $A_{\text{sig}}(t)$ and phase $\theta_{\text{sig}}(t)$ however, contain the information about the state of the transmon. Both signal and reference are individually recorded with an ADC acquisition board, the IQ-demodulation is done in digital post-processing.

5.3.2 Digital IQ Demodulation

The acquisition is done with a Teledyne SP devices SDR14 [54] 2-channel ADC using a sampling rate of $f_s = 200$ MHz. Signal and reference are recorded individually. Both signals oscillate at the down-mixed carrier frequency $f_{\text{IF}} = 12.5$ MHz. The recorded signals are thus resolved in time with

$$N = \frac{200 \text{ MHz}}{12.5 \text{ MHz}} = 16 \quad (94)$$

points per period. The signal defined in eq. 92 can be rewritten as

$$\text{sig}(t) = I(t) \cos(\omega_{\text{IF}}t) + Q(t) \sin(\omega_{\text{IF}}t) \quad (95)$$

using the in-phase and out-of-phase quadratures I and $Q \in \mathbb{R}$. A signal is fully described by the single complex number $I(t) + iQ(t)$. Definition via quadratures is equivalent to the amplitude-phase notation. The amplitude corresponds to the absolute value

$$A_{\text{sig}}(t)^2 = |I(t) + iQ(t)|^2 = I(t)^2 + Q(t)^2 \quad (96)$$

and the phase to argument $\theta_{\text{sig}}(t) = \arg(I(t) + iQ(t))$. Quadratures allow for a clear depiction of signals in the IQ plane. An example is shown in fig. 39. IQ demodulation is based on the assumption that I and Q vary slowly and stay constant during one oscillation period of the carrier

$$\begin{aligned} I(t) &\longrightarrow I, \\ Q(t) &\longrightarrow Q. \end{aligned} \quad (97)$$



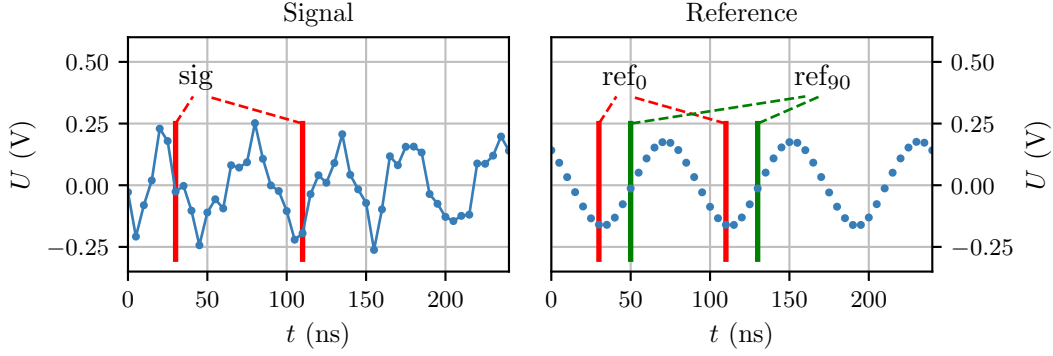


Figure 40: Measured signal (**left**) and reference voltages (**right**) illustrating the digital IQ-demodulation scheme. One period of $T = 80$ ns contains 16 samples separated by 5 ns. The lines connecting the noisy signal data are drawn to guide the eye. Point-wise multiplication and summation of signal and (shifted) reference allows to extract the (Q) I quadrature.

At first, signal and reference are multiplied

$$\begin{aligned} \text{sig}(t) \times \text{ref}_0(t) &= \underbrace{\left(I \cos(\omega t) + Q \sin(\omega t) \right)}_{\text{sig}} \times \underbrace{A_{\text{ref}} \cos(\omega t)}_{\text{ref}_0} \\ &= \left(I \cos^2(\omega t) + Q \frac{\cos(2\omega t)}{2} \right) \times A_{\text{ref}}. \end{aligned} \quad (98)$$

Integrating this expression over one oscillation period T leads to

$$\frac{1}{A_{\text{ref}}} \int_0^T \text{sig}(t) \times \text{ref}_0(t) dt = I \int_0^T \cos^2(\omega t) dt + Q \int_0^T \frac{\cos(2\omega t)}{2} dt. \quad (99)$$

The term proportional to Q averages out to 0. The integral in the first term simply evaluates to π . Rearranging leads to an expression for the I quadrature

$$I = \frac{1}{\pi A_{\text{ref}}} \int_0^T \text{sig}(t) \times \text{ref}_0(t) dt. \quad (100)$$

An analogous derivation starting with the 90° shifted reference results in

$$Q = \frac{1}{\pi A_{\text{ref}}} \int_0^T \text{sig}(t) \times \text{ref}_{90}(t) dt. \quad (101)$$

In digital signal processing, the continuous time signals are replaced by discrete samples denoted with square brackets

$$\begin{aligned}\text{sig}(t) &\longrightarrow \text{sig}[i], \\ \text{ref}(t) &\longrightarrow \text{ref}[i]\end{aligned}\tag{102}$$

with the sample index $i \in \mathbb{N}$. The time between two consecutive records $\text{sig}[i]$ and $\text{sig}[i+1]$ is the inverse sampling rate $1/f_s = 5$ ns. The integrals are replaced by a discrete sum

$$\int_0^T dt \longrightarrow \sum_0^{N-1} \Delta t\tag{103}$$

where $\Delta t = T/(N-1)$. Considering the chosen intermediate frequency the period is $T = 1/f_{\text{IF}} = 80$ ns. Fig. 40 shows three periods (240 ns) of actual recorded signal and reference voltages. The reference is recorded directly after generation, resulting in a negligible SNR. The signal however, is passing through the cryostat. It is strongly attenuated in order to reach single photon powers at the base stage, only to be amplified by a number of noisy amplifiers before arriving at the room temperature acquisition board. Due to the JPC, the recorded signal is still recognizable with the naked eye. One period of each signal, reference and shifted reference are indicated in the graph in fig. 40. Each period allows the extraction of (I, Q) data point, corresponding to an averaging time of $t_{\text{avg}} = 80$ ns per point. Equations 100 and 101 are simply replaced by their discrete versions

$$I = \frac{1}{\pi A_{\text{ref}}(N-1)} \sum_0^{N-1} \text{sig}[i] \times \text{ref}_0[i]\tag{104}$$

and

$$Q = \frac{1}{\pi A_{\text{ref}}(N-1)} \sum_0^{N-1} \text{sig}[i] \times \text{ref}_{90}[i].\tag{105}$$

The fluctuations in the computed quadratures can be easily reduced by averaging over more than one period and replacing N by $2N, 3N \dots$. A maximum of 16 periods are used in this experiment, which is equivalent to $T_{\text{avg}} = 1280$ ns.

5.4 Probe Power Calibration

The continuous IQ-probe beam generates a steady state field in the cavity with a constant mean photon number n . The average cavity population is different for probe frequencies f_2 and f_3 . Calibration of the input power is possible by looking at the qubit's AC stark shift caused by the cavity field. In the dispersive regime, one cavity photon is expected to



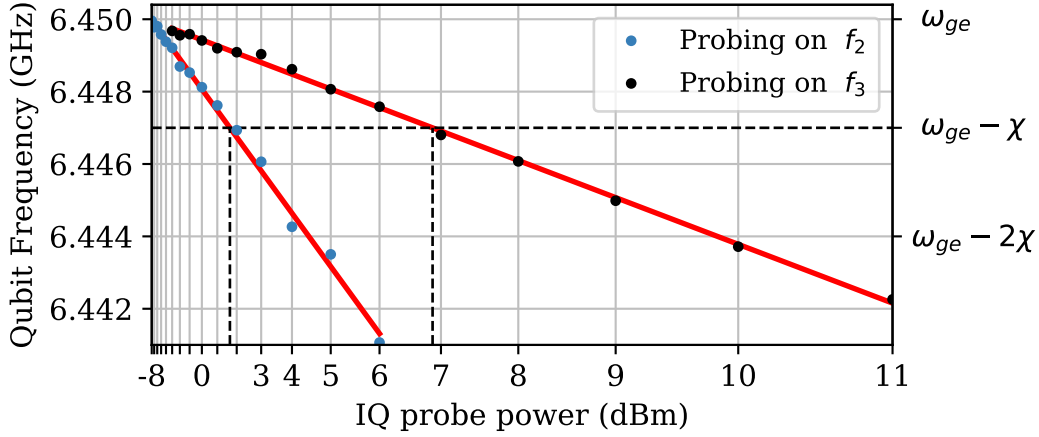


Figure 41: Qubit stark shift for the two IQ probe frequencies f_2 and f_3 . Each photon in the cavity shifts the qubit transition frequency by χ . The labels on the right indicate the expected frequency for 0, 1 and 2 cavity photons. A drive at f_2 occupies the cavity with one photon on average at a power of 1.8 dBm. At f_3 a power of almost 7 dBm is needed to produce the same mean field in the cavity. The one-photon input powers for both drive frequencies are indicated with black dashed lines. A linear fit of the data (red) allows to extract a calibration factor to convert from generator output powers to mean cavity photon numbers.

shift the qubit transition frequency by χ_e from its original value ω_{ge} . The linear relation

$$\omega_{ge}(n) = \omega_{ge} - \underbrace{\lambda p_{in}}_n \chi_e \quad (106)$$

holds for low photon numbers n . The calibration factor λ connects the cavity photon number to the input IQ probe power p_{in} at the generator output. The dispersive shift $\chi_e \approx 3$ MHz and the unshifted transition frequency $\omega_{ge} = 6.450\,08(3)$ GHz are known from previous measurements, see tab. 3.

In order to determine the calibration factor, the qubit transition frequency is measured for various IQ probe powers. The results for both frequencies f_2 and f_3 are shown in fig. 41. Determination of the qubit frequency is described in sec. 3.1.2. Clearly, an input signal at f_2 causes a higher cavity field. At that frequency, an input power of ~ 2 dBm already populates the cavity with a mean photon number of 1. At f_3 , as much as 7 dBm are needed to put a photon in the cavity. The one-photon input powers are indicated in the graph as black dashed lines. This imbalance is explained well by the observed low temperature of the qubit-cavity-system. Without drives, the transmon is for the most part found in the ground state (compare fig. 16). As a consequence, the cavity absorbs less power at f_3 as

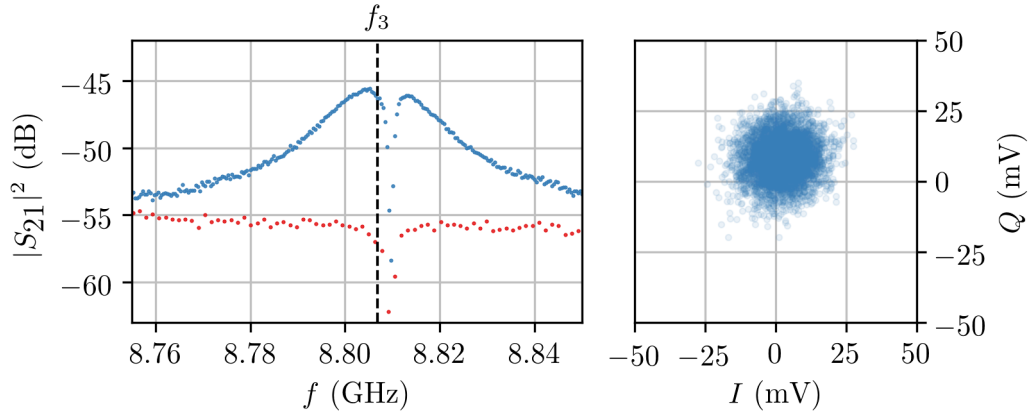


Figure 42: **Left:** VNA traces of the cavity with JPC on (blue) and off (red). The gain is set up to 12 dB centred at the IQ probe frequency f_3 . **Right:** 5000 IQ-data points, measured with the JPC turned off. The signal-to-noise ratio is too low to resolve the transmon states.

the detuning to the ground state cavity resonance is larger.

Fitting the linear model from eq. 106 to the data allows to extract the calibration factors $\lambda_2 = 0.76(1)$ and $\lambda_3 = 0.211(1)$ (uncertainties are the standard deviations from the fits). As a reminder, the actual power at the input port of the cavity is about -119 dBm lower than the generator output power shown on the x-axis of the graph in fig. 41.

5.5 First Measurements

This section presents the first measurement where the transmon's states are resolved in the IQ-plane. Considering amplitude and phase allows to map the IQ-data to the states $|g\rangle$, $|e\rangle$ and $|f\rangle$. This assignment is further verified in sec. 5.6.3 via relating the distribution of the data to a temperature. The right panel of fig. 42 shows the results of an IQ measurement without using the JPC. Clearly, the signal amplitude (displacement from the IQ plane's origin) is too low compared to the noise (spread of the results). The transmon states can not be distinguished. In order to perform a successful IQ-measurement, the JPC has to be set up accordingly. The tuning process is monitored with the VNA - measured traces with pump on and off are shown in the left panel of fig. 42. The graph shows the set-up for the three-state-measurement, using a gain of approximately 12 dB centred at f_3 .

When the experiment is repeated with the JPC turned on, the transmon states are clearly



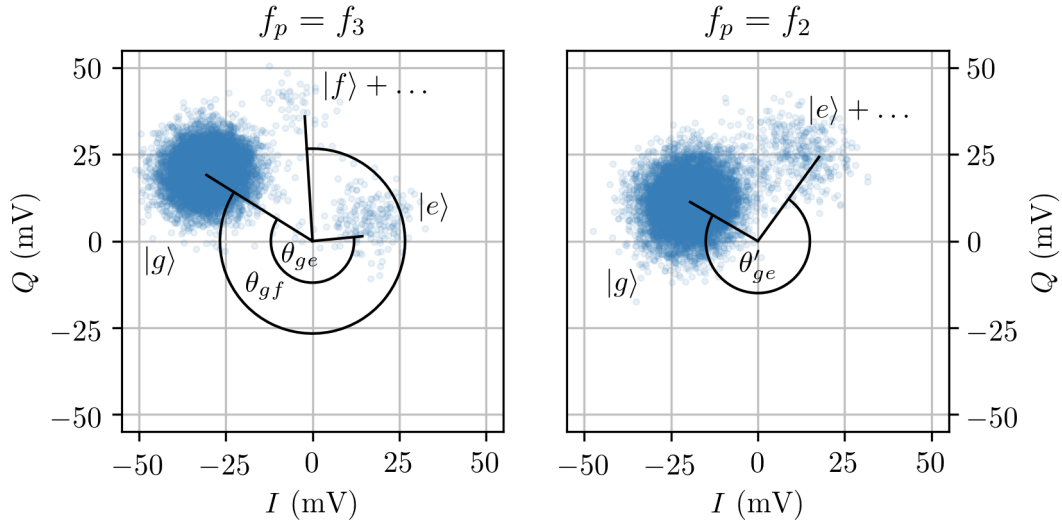


Figure 43: IQ measurements with probe frequencies f_3 (**left**) and f_2 (**right**). Showing 5000 data points measured with a probe power of $n \approx 4$ resonator photons and an averaging time of $T_{\text{avg}} = 1280$ ns per point. Gain was set to 12 dB centred at f_3 , resulting in a slightly lower signal amplitude in the right plot. The results are clustered around three centres of attraction (‘disks’), corresponding to $|g\rangle$, $|e\rangle$ and $|f\rangle$. Expected phase shifts and relative amplitudes (compare tab. 5 and 6) are indicated in black. They allow to assign the disks in IQ plane to the associated transmon state.

resolved in the IQ plane. The displacement from the origin is significantly increased, whereas the variance remains almost unchanged. Fig. 43 presents two sets of IQ data measured with probe frequencies f_2 and f_3 . The plot shows 5000 data points acquired with an averaging time of 1280 ns per point. Probe power was set corresponding to an average cavity photon number of 4. JPC gain was about 12 dB at the three-state probe frequency and about 5 dB lower at the two-state experiment, resulting in a proportionally lower amplitude.

The IQ data points accumulate in two respectively three ‘disks’ in the IQ-plane. Following the considerations presented in sec. 5.1, the clusters can be assigned to the transmon states. The expected relative angles and amplitudes are drawn in the graphs. Due to the almost critically coupled cavity, the phase shift between ground- and final-state is almost a full circle. As a consequence, the disks are located relatively close to each other. This slight design flaw leaves some room for improvement in terms of contrast or equivalently measurement speed. Most of the results appear to end up in the $|g\rangle$ cluster, as one would expect for a cold system close to its ground state. This observation is confirmed in sec. 5.6.3.

The next section deals with the analysis of IQ-data. Various figures of merit are defined, which allow to quantify the distribution of the IQ-data in terms of separation, width and number of results in the disks. Logarithmic 2D-histograms are introduced as an alternative visualization method. They provide a simple way of getting a quick overview of a large set of IQ-data.

5.6 Analysing IQ-data

This section relates how the probability distribution underlying a set of IQ-data is found by binning the data into two-dimensional histograms and subsequently fitting the sum of two or three Gaussians to the data.

5.6.1 2D Histograms

In the previous section each individual IQ-record was represented as one point in a scatter plot. This method of display quickly becomes incomprehensible when dealing with large sets of data. An alternative approach is, to divide the IQ-plane in tiles of equal width and height $\Delta I = \Delta Q = \Delta x$. Counting the results that end up in each bin creates a two-dimensional histogram. The left panel of fig. 44 shows the histogram of an IQ-measurement containing 330000 IQ data points using 50×50 bins. The drawback of this depiction method is revealed immediately. As the transmon is for the largest part in the ground state, the bins in the area of the $|e\rangle$ and $|f\rangle$ disk contain only a very small number of events. However, using a logarithmic scale and plotting $\log(N)$ instead of the bare number of events N , creates a meaningful plot allowing for a quick overview of the data quality and distribution, see fig. 44 (right panel). The following section describes, how the underlying probability distribution of the IQ measurements is extracted by fitting the 2D histograms with a sum of Gaussian profiles.

5.6.2 Gaussian Fits

The transmon states $|g\rangle$, $|e\rangle$ and $|f\rangle$ correspond to unique points in the IQ-plane with coordinates (I_i, Q_i) for $i \in \{g, e, f\}$. Various noise sources lead to a Gaussian spread of the



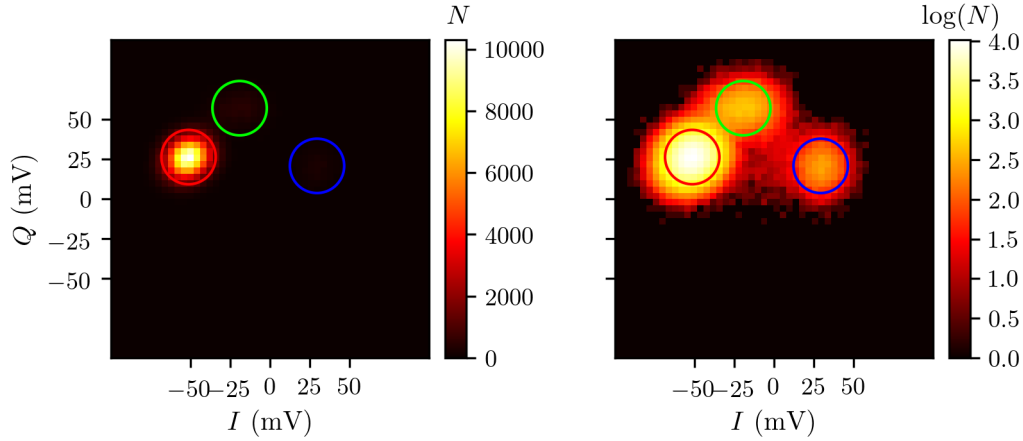


Figure 44: Linear and logarithmic histogram of 162000 IQ records using 50×50 bins. Measured at $f_p = f_3$ with a probe power of ~ 4 photons, an averaging time of $t_{avg} = 1280$ ns and $G_{JPC} = 12$ dB. The circles represent 4σ of the fitted Gaussian profiles.

measurement results around these central points. The quantum fluctuations as well as the noise added by the amplifiers get amplified along the measurement chain. Fitting the data with a sum of Gaussian profiles allows to extract the underlying probability distribution. A single two-dimensional Gaussian centred at (I_i, Q_i) with amplitude A_i and width (standard deviation) σ is described by

$$f_i(I, Q) = A_i \frac{1}{\sqrt{2\pi}\sigma^2} e^{-\frac{(I-I_i)^2 + (Q-Q_i)^2}{2\sigma^2}}. \quad (107)$$

Note that a common width σ is assumed for the profiles. Depending on the type of measurement (probing on f_2 or f_3) the appropriate fitting function is either the sum of two

$$F(I, Q) = \sum_{i \in \{g, e\}} f_i(I, Q) \quad (108)$$

or three

$$F(I, Q) = \sum_{i \in \{g, e, f\}} f_i(I, Q) \quad (109)$$

Gaussian profiles. $F(I, Q)$ contains either 8 or 12 free parameters. The fit is performed in *python* using the *curve_fit* method of the *scipy* library. The uncertainty of the counts in each bin is assumed to be $\Delta N = \sqrt{N+1}$. A minimal error of 1 is important for the stability of the numeric fitting routine. Otherwise empty bins would have an uncertainty of $\Delta N = 0$, causing the algorithm to fail. Adding a pseudocount of one is in accordance with Laplace's stochastic rule of succession [55]. It justifies a minimum miscount of 1 with

the argument that, if one more additional data point was measured it might end up in the previously empty bin.

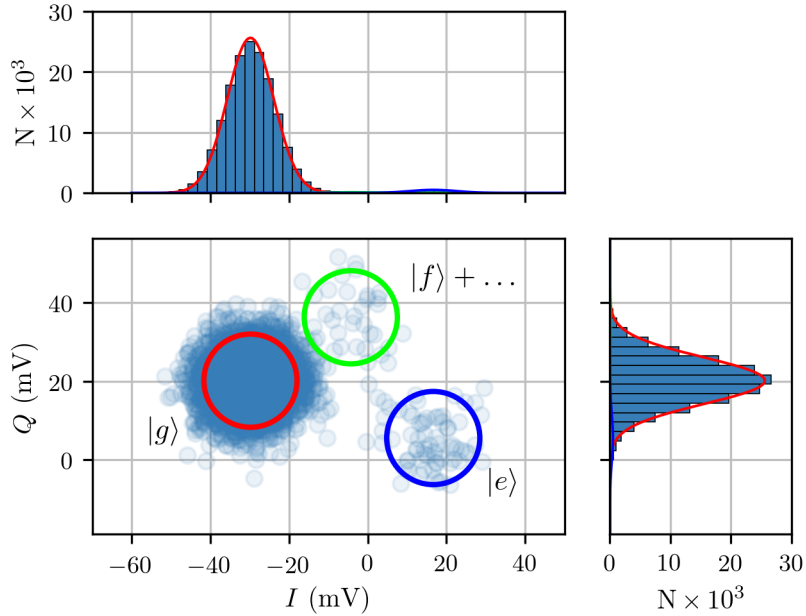


Figure 45: IQ-measurement with $n_p = 4$ probe photons, $t_{avg} = 1280$ ns, 162000 points and $G_{JPC} = 12$ dB. The scatter plot shows the first 10000 data points, plotted with a transparency of 0.1. The circles represent 4σ of the gaussian profiles obtained by the fit. The projected histograms are computed by binning the I - respectively the Q -components of the full data set into 50 intervals of equal width. The coloured lines show the Gaussian profiles integrated along the projection axis.

An example of the fit is shown in fig. 45. The data is the same as shown above in fig. 44. Bin width was $\Delta I = \Delta Q = 4$ mV. The circles are centred at the positions (I_i, Q_i) as determined with the fit. Their diameter equals to 4σ . Top and side panel show a projection of the histogram on the I - and Q -axis respectively. A projection of the fitted 2D-Gaussians is indicated with the color convention g (red), e (blue), f (green). The resulting fit parameters are listed in tab. 7. The graph is reproduced in fig. 58 in the appendix with the histograms plotted on a logarithmic scale, allowing for an easier comparison of data and fit.

Visually, the fit appears to agree quite well. The coefficient of determination R^2 allows to



	$A \times 2\pi\sigma^2/(\Delta x)^2$	I (mV)	Q (mV)	σ (mV)
$ g\rangle$	158 100(250)	-29.92(1)	20.07(1)	5.830(4)
$ e\rangle$	3034(26)	16.71(5)	5.60(50)	5.830(4)
$ f\rangle$	693(13)	-4.4(1)	36.2(1)	5.830(4)

Table 7: Fit parameters for the data shown in fig. 45 (and fig. 44). The occupation $A \times 2\pi\sigma^2/(\Delta x)^2$ corresponds to the volume of the respective Gaussian profile and is equivalent to the number of events registered in that disk. Roughly 97.7% of the events are attributed to the ground state.

evaluate how well the data is described by the model. It is defined as

$$R^2 = 1 - \frac{\sum_j (y_j - F_j)^2}{\sum_j (y_j - \bar{y})^2} \quad (110)$$

with data points y_j , data average \bar{y} and the model F_j evaluated at position j . In a 50×50 bin histogram j takes on the integer values from 0 to 2500. Intuitively, R^2 compares the prediction quality of the model to the arithmetic mean, which is one of the simplest measures to describe a set of data. Values close to unity indicate a good match of model and data. Fitting the sum of three Gaussian profiles to the data shown in fig. 45 results in a coefficient of determination of $R^2 = 0.998$.

It is possible that the system undergoes an abrupt transition from one state to another (quantum jump) during the averaging time of a single IQ point. Consequently, that data point ends up somewhere in the middle of the disks that correspond to the two states. These intermediate points are clearly not described by a simple sum of 2D Gaussians. However, as the JPC allows for averaging times that are faster than the system's transition rates, this deviation from the model can be neglected. The influence of averaging time on the fit quality is analysed in sec. 5.7.3.

5.6.3 Temperature

A natural question of interest is, whether the number of events g , e , and f follows a thermal distribution. The average occupation of each state is easily derived from the fitted Gaussian model. Integrating the amplitude along both dimensions I and Q results in the 'peak volume' $V_i = A_i 2\pi\sigma^2/(\Delta x)^2$ with $i \in g, e, f$, which directly corresponds to the number of events in that disk. Fig. 46 shows the occupation derived from the data shown in fig. 45. The state's energies are $(E_g, E_e, E_f)/\hbar = (0, \omega_{ge}, 2\omega_{ge} - \alpha)$. Assuming a thermal distribution, the relative occupation is expected to be proportional to the Boltzmann factor.

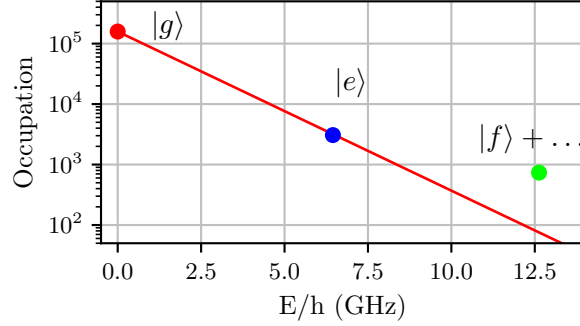


Figure 46: Occupation $A_i 2\pi\sigma^2 / (\Delta x)^2$ of each peak $i \in g, e, f$ as derived from fitting the IQ histograms. Errors are much smaller than the points. The underlying 162000 points are measured at $n_p = 4$, $t_{avg} = 1280$ ns and $G_{JPC} = 12$ dB. The temperature is derived via minimization of eq. 112, taking into account the additional f state counts stemming from the higher transmon levels. A Boltzmann factor with the resulting temperature 78.7(3) mK is drawn in red.

The model

$$p(E) = V_0 \exp^{-E/(k_B T)}. \quad (111)$$

has two free parameters - the ground state occupation V_0 and the temperature T . At very cold temperatures, photons actually obey Bose-Einstein statistics. However, at energy scales of 6 GHz and temperatures on the order of 50 mK, the Bose-Einstein-distribution is modelled well by eq. 111 as $E \approx 3k_B T$. The fit was done using *numpy*'s *scipy.optimize.minimize* method, assuming that the states above f end up as counts in the f state. The sum of squared residuals used for the optimisation reads

$$\frac{(p(E_g) - V_g)^2}{\Delta V_g^2} + \frac{(p(E_e) - V_e)^2}{\Delta V_e^2} + \frac{(p(E_f) + p(E_h) + p(E_i) + p(E_j) - V_f)^2}{\Delta V_f^2}, \quad (112)$$

taking into account three higher excited states (h, i, j) with estimated energies $\hbar(3\omega_{ge} - 2\alpha, 4\omega_{ge} - 3\alpha, 5\omega_{ge} - 4\alpha)$. Following [56], the residuals are weighted with the standard deviations ΔV_i which are determined from fitting the IQ data. The minimization routine calculates a Hessian variance matrix, which allows to derive the standard deviation of the fit parameters. The fit converges with an R^2 of 0.9999 and results in a temperature of 78.7(3) mK. Ignoring the transmon's higher excited states and simply fitting the occupations V_g, V_e, V_f with eq. 111 results in a slight overestimation of the temperature by 0.5 mK.



An alternate approach in determining the relative occupation of states g, e and f is to count the events occurring within one or two standard deviations around the disk centres. For data that is well modelled by a sum of Gaussians ($R^2 > 0.98$) the resulting temperature agrees with the value derived from the fit parameters within 2 mK. The following section shows data sets that deviate strongly from the Gaussian distribution due to squeezing and other effects. In such measurements the observed difference in the methods of temperature calculation was up to 10 mK.

5.7 Improving the Contrast

This section relates how the contrast of the dispersive readout scheme depends on the key experimental parameters, readout power, averaging time and JPC gain. The IQ-data is binned into two-dimensional histograms and fitted with Gaussian profiles as described above. Width and separation of the fitted profiles are used as quantitative measures of the measurement contrast. In addition, the contrast is quantified by the overlap of the fitted Gaussians. It is calculated as the integrated product of the individual profiles

$$\text{overlap} = \frac{1}{A_g A_e A_f} \int_{-\infty}^{\infty} \int_{-\infty}^{\infty} f_g(I, Q) f_e(I, Q) f_f(I, Q) dI dQ \quad (113)$$

Identical Gaussians result in an overlap of 1, whereas separate peaks result in a quick decrease towards 0. In order to visualize the trends, the overlap is plotted using a logarithmic scale in the following considerations. The quality of the model is monitored with the coefficient of determination R^2 as defined in eq. 110. Finally, the temperature is evaluated for each IQ-data set. The temperature is derived from the volume of the fitted Gaussians, even when the e and f state populations deviate from the expected thermal population (compare fig. 59). Together, these five quantities provide an overview about what to expect from a dispersive IQ-measurement for a particular choice of parameters. Below, the IQ-data is displayed in form of logarithmic histograms. Circles with a diameter of 4σ indicate position and width of the fitted Gaussians. Statistically, roughly 95% of the measurement results can be expected to lie within the 4σ circles. The states are encoded in the color of the circles - g, e and f are represented by red, blue and green respectively. All the quantities presented in this section, are derived from Gaussian fits of the binned IQ data containing a large number of samples. The statistical uncertainties of the parameters resulting from the fit are much less than 1% (compare tab. 7). As a consequence, the uncertainties of the derived quantities presented in this section are small. Errors are not shown in the plots as they are below point-size.

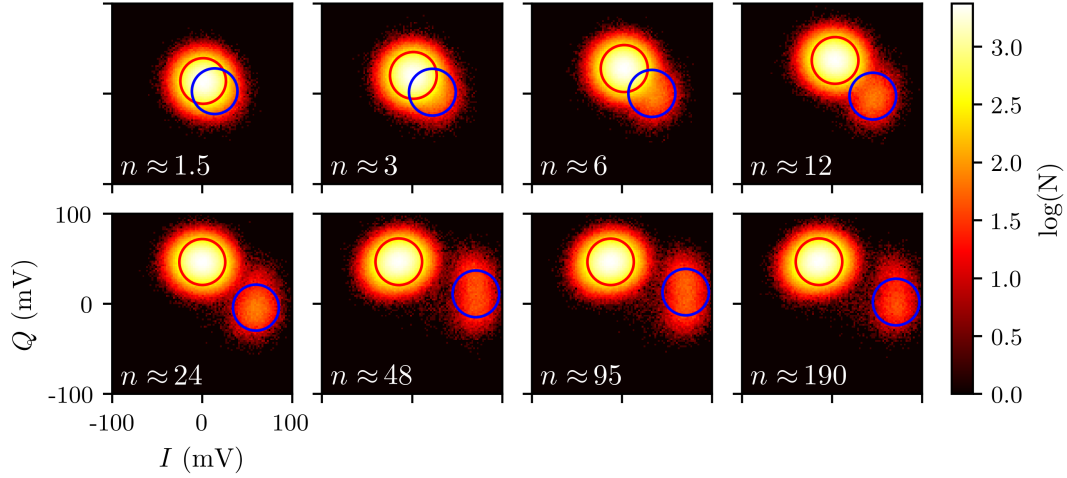
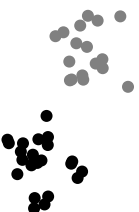


Figure 47: IQ-probe power sweep. 160000 data points measured at f_2 with $t_{avg} = 320$ ns and $G_{JPC} = 15$ dB are displayed in each logarithmic histogram. The diameter of the circles corresponds to 4σ of the fitted Gaussian profiles. Separation of the g and e disk goes up with increasing probe power. As the JPC begins to saturate, the disks become more and more ‘squeezed’, deviating from the symmetric Gaussians.

5.7.1 Readout Power Sweep

Fig. 47 shows eight IQ-data sets measured with increasing probe power. The power is altered in steps of 3 dB from 1.5 to 190 photons. Data is taken at the two-state probe frequency f_2 with an averaging time of $t_{avg} = 320$ ns. JPC gain is set to 15 dB. The analysis is shown in fig. 48.

With increasing probe power, the distribution of the IQ-records begins to deviate from the model of symmetric Gaussian profiles, indicated by the decreasing R^2 . At a probe power of $n \approx 12$ cavity photons, a slight asymmetry becomes visible in the plotted histograms. This ‘squeezing’ is due to the saturation of the JPC, which provides linear amplification only up to powers corresponding to a few photons in the JPC resonator. Separation rises with increasing power. The separation in units of voltage is expected to be proportional to the square root of the power (photon number). A fit $\sim \sqrt{n}$ including powers up to 25 photons is indicated in the graph (red dashed line). The saturation of the JPC becomes obvious at higher powers as the separation evens out at a maximum of roughly 10σ . In accordance with the increasing separation, the overlap calculated with eq. 113 is declining. The peak width σ is independent of the probe power, reflecting the fact that the main noise contributions are the transmon’s quantum fluctuations. Temperature also remains constant



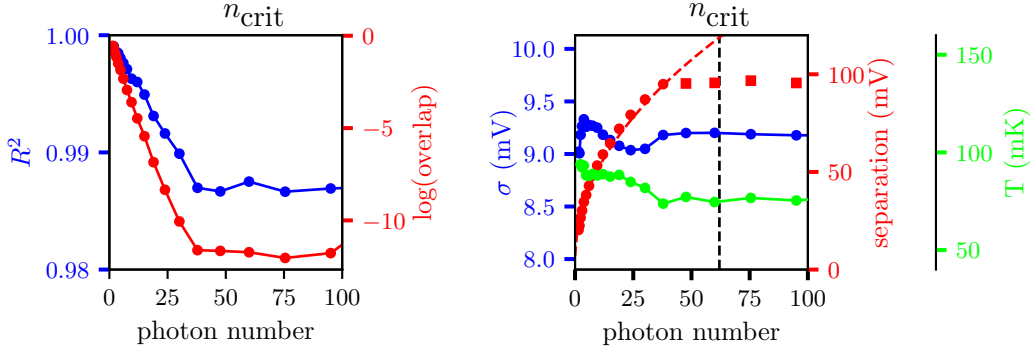


Figure 48: Probe power sweep analysis. Higher probe power results in a stronger contrast, as seen by the increasing separation and decreasing overlap. Temperatures are not calculated for powers below 5 photons. The reason is the large uncertainty in the state population when σ is on the order of the separation. The dashed red line indicates a \sqrt{n} fit to illustrate the connection between readout power and voltage separation. Only powers up to 45 photons are included in the fit, as the saturation of the JPC causes the separation to flatten out at higher photon numbers. Solid lines serve as guides to the eye. Statistical errors for the temperature, separation and width σ as derived from the fits are too small to be recognised in the graph.

across the measured range. Non-thermal states (deviating from the fitted Boltzmann factor) have been observed for probe powers above 10 photons. In some cases, the f state population equals or even exceeds the excited state population (compare fig. 45 and fig. 59). Consequently, the Boltzmann minimization converges with a lower R^2 . The resulting temperatures remain almost unchanged, as they depend mostly on the ratio A_e/A_g which only varies slightly.

5.7.2 JPC Gain Sweep

The raw data of the JPC gain sweep is plotted in fig. 49. The gain was increased in irregular steps from 7 dB to 29 dB. Averaging time was set to $t_{avg} = 320$ ns. A relatively high probe power of 21 readout photons was chosen, in order to be able to resolve the states even for low JPC gains. Data was measured at the three-state probe frequency f_3 .

The separation is calculated as the arithmetic mean of the individual distances between the g , e and f disks. Derived parameters are collected in fig. 50. Not surprisingly, the separation increases with higher JPC gains in agreement with the decreasing overlap. The peak width σ also rises with increasing gains, reflecting the JPC's amplification of the quantum fluctuations and the noise added by the JPC. Increasing gains cause the JPC to

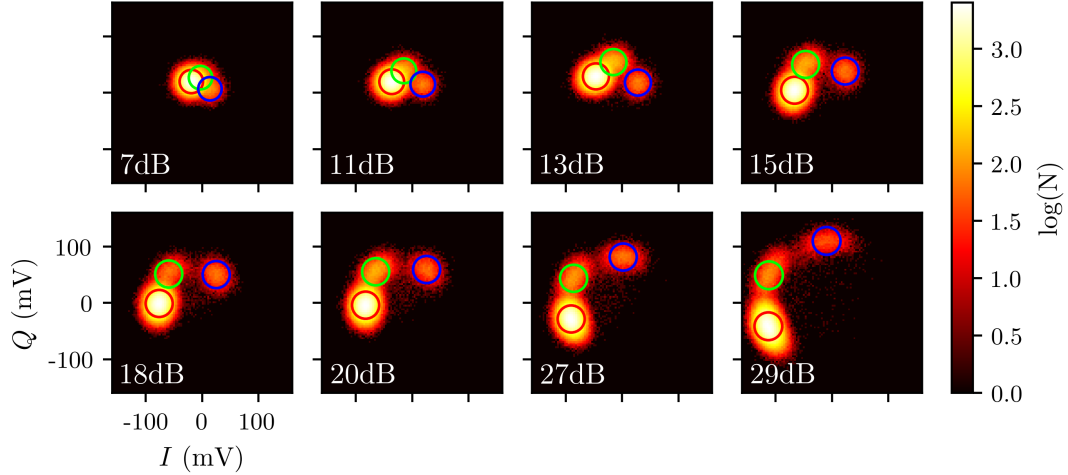


Figure 49: JPC gain sweep with 4σ circles from the Gaussian fit. Measured at f_3 with $t_{avg} = 320$ ns and a readout power of 21 photons. 160000 data points per measurement. At this probe power, the JPC begins to saturate at around 20 dB, causing squeezing and rotation in the IQ-plane.

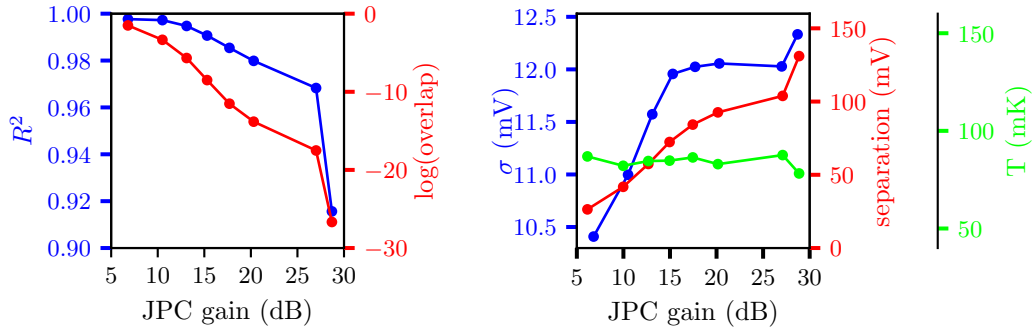


Figure 50: Characteristic parameters of the JPC gain sweep. Lines present a guide to the eye. As expected, the separation increases while width and temperature are unaffected by the amplifier. R^2 and the overlap are decreasing as the JPC squeezes and deforms the IQ data with increasing saturation. Point sized errors are not displayed in the graph.



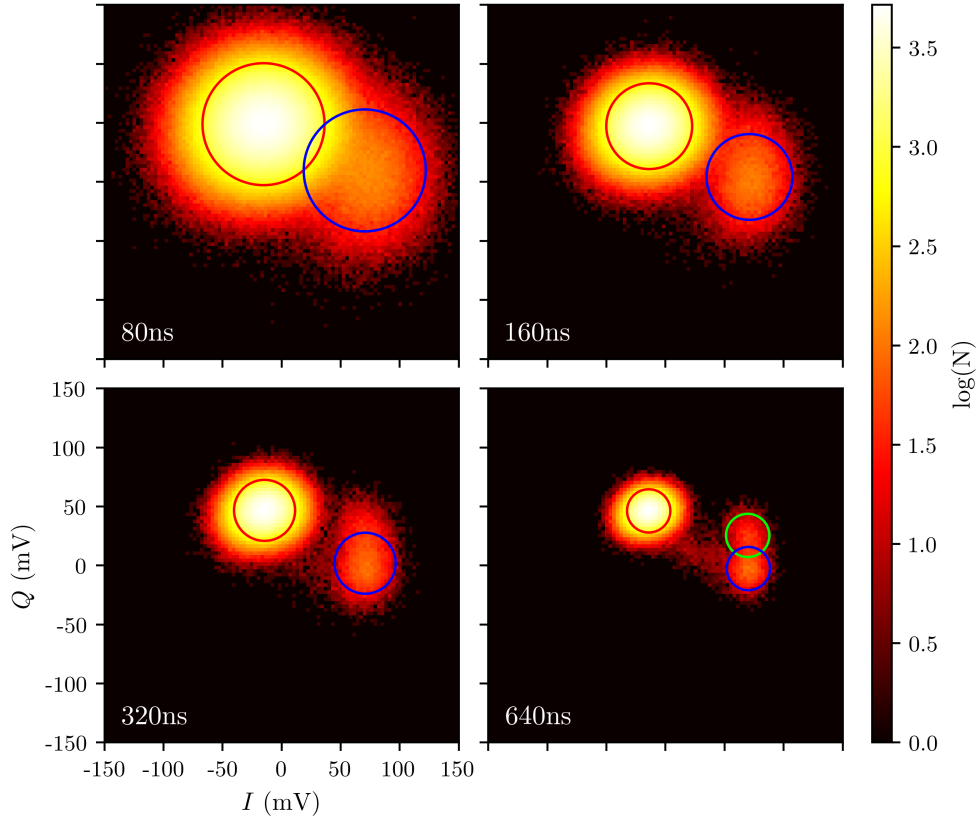


Figure 51: Sweep of the IQ integration time t_{avg} . Measured at f_2 with $n_p = 190$ photons and a JPC gain of 15 dB. At such a high probe power, two states are resolved at averaging times as fast as $t_{avg} = 80$ ns. Circles represent 4σ of the Gaussian fit.

saturate, resulting in a drastic drop of R^2 . The JPC loses its phase preserving quality, causing squeezing and rotations in the IQ-plane. As expected, the temperature appears to be independent of JPC gain. After being reflected by the JPC, the amplified signal is routed away from the cavity using a circulator with a cross-port isolation of more than 20 dB. Thus, the signal's effect on the experiment after the round trip to the JPC can be safely neglected.

5.7.3 Readout Time Sweep

Fig. 51 shows the raw data of the readout time sweep. IQ-demodulation was done averaging over 1, 2, 4 and 8 periods, corresponding to averaging times $t_{avg} = (80 \text{ ns}, 160 \text{ ns}, 320 \text{ ns}, 640 \text{ ns})$. The evaluation is plotted in fig. 52. As expected, the width of the disks decreases

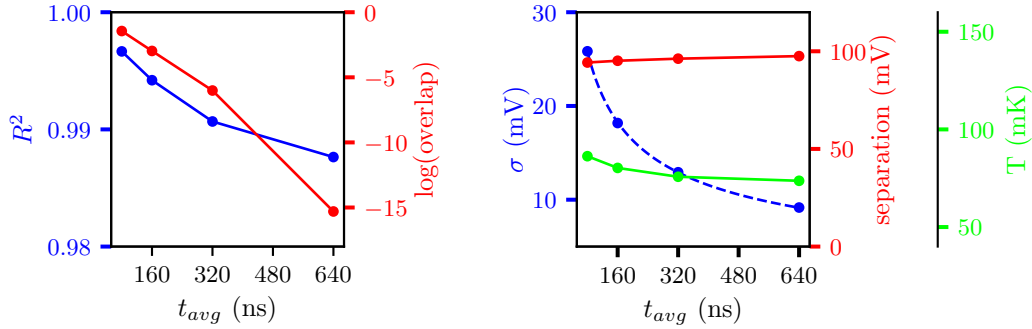


Figure 52: Readout time t_{avg} sweep analysis. Measured at f_2 with $n_p = 190$ photons and a JPC gain of 15 dB. The separation is calculated between g and e , also for the fourth plot in fig. 51, where three states are already resolved. Solid lines serve as a guide to the eye. The width σ (signal noise) decreases proportional to $\sqrt{1/t_{avg}}$, as indicated with the fit (blue dashed line). Point sized errors are not displayed.

with $1/\sqrt{t_{avg}}$. The respective fit is drawn in the graph (blue dashed line). With increasing t_{avg} , events where the system undergoes a quantum jump during the integration time occur at a higher rate. These events appear in between the g , e and f disks and are most prominent at $t_{avg} = 640$ ns. For this reason, the R^2 of the Gaussian fit decreases for higher averaging times. For large averaging times, the f state is resolved even at the two-state probe frequency f_2 . The small phase difference of $\sim 20^\circ$ (compare fig. 36) is enough to distinguish the states. It is interesting to note, that most of the intermediate events occur between the ground state and the excited state (intermediate events between e and f are not resolved). One photon transitions are strongly preferred. In fact, direct transitions between g and f state are dipole forbidden, and therefore strongly suppressed.

5.7.4 Summary

The JPC assisted dispersive IQ readout depends strongly on the experimental parameters of the measurement setup. The key observation of this section is, that the various parameters influence each other. Paying attention to this interplay is crucial for the choice of an appropriate experimental configuration. For example, both the JPC gain and the readout probe power have the tendency to increase the separation. However, these two parameters have different side effects. While higher JPC gain causes squeezing and rotations in the IQ plane, higher probe power is suspected to interfere with the system in a increasingly not QND way (e.g. causing deviations from thermal population distributions for powers $n >$



10.) The separation is not increased by the IQ integration time t_{avg} . Contrast is improved regardless as the noise of the signal decreases with $1/\sqrt{t_{\text{avg}}}$. Longer averaging times result in a higher number of quantum jump events that happen during the integration time. These points end up in between the disks in the IQ plane, causing a strong deviation of the Gaussian model distribution when t_{avg} becomes comparable to the system's transition rates.

A straightforward way to determine a suitable readout configuration seems to begin with a JPC gain of about 20 dB, promising the highest gain in SNR (compare sec. 4.4.5). Then, the choice of probe power and t_{avg} becomes a trade-off in contrast, measurement time and 'QNDness' of the measurement. In some cases, squeezing and JPC gains of up to 25 dB might be acceptable, as the increased separation can result in a higher fidelity in the identification of the states.

When distinguishing two states, the contrast can be nicely quantified by the miscount probability p_{mis} as defined in eq. 114. When working on this project, I found $n_p = 6$, $t_{\text{avg}} = 640 \text{ ns}$ and $G_{\text{JPC}} = 15 \text{ dB}$ a convenient configuration. It provides a miscount probability of only 1% while introducing a negligible amount of squeezing. The main limiting factor of the contrast in this setup was clearly the low Q_{int} of the cavity. Adapting the readout resonator would be a simple and quick way to improve the readout scheme.

5.8 Quantum Jumps

This section investigates the temporal evolution of the transmon state. Measurements are done probing at f_2 , distinguishing whether the transmon is in the ground state or not. The JPC is operated at a gain of 15 dB. A probe power of 6 photons is sufficient to reach a detection fidelity of 99% (at averaging times of $t_{avg} = 640$ ns). Analysis of how long the systems remains in the same state allows to estimate the excited state lifetime T_1 . Assuming a negligible e state population, the system is treated as an effective two-level-system (qubit) in this section.

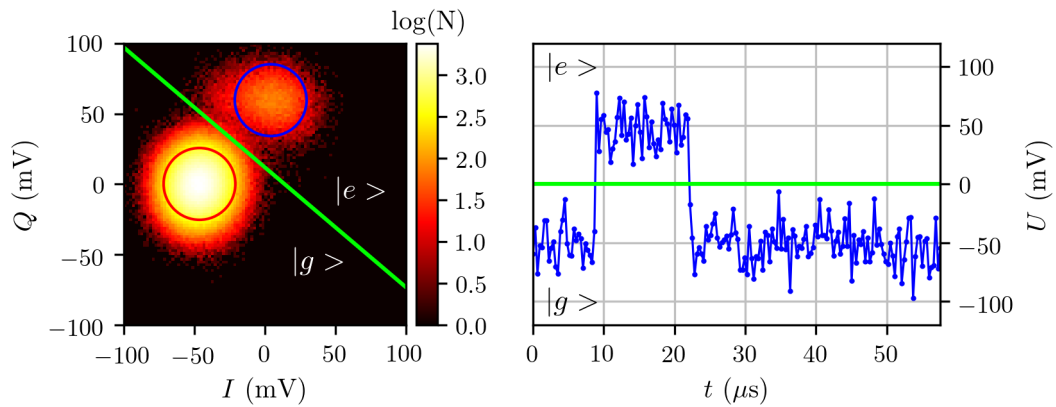


Figure 53: IQ data taken with $n \approx 24$, $t_{avg} = 320$ ns and a JPC gain of 15 dB. **Left:** Histogram (100×100 bins) of the full set of 1300000 records. Gaussian fits are indicated with circles of 4σ diameter. The separation line is drawn in green. **Right:** Jumptrace. Distance from the separation line over time for 180 IQ-records. Quantum jumps are clearly resolved in time. This section of the trace features a thermal excitation and subsequent decay after $\sim 14 \mu$ s.

5.8.1 Jump Traces

As observed in sec. 5.7, high readout power allows for well resolved IQ-measurements with short averaging times. Fig. 53 (left) shows 1300000 IQ records measured at a power of $n \approx 24$ photons and $t_{avg} = 320$ ns. The separation line (green) is drawn in equal distance from the centres of the fitted Gaussians, crossing the connection line (not shown) in a right angle. The right panel of fig. 53 shows the distance between that separation line and the individual IQ-records over time. 180 data points are displayed in the graph, corresponding to a duration of 58μ s. Each measurement result is assigned to one of the qubit states $|g\rangle$



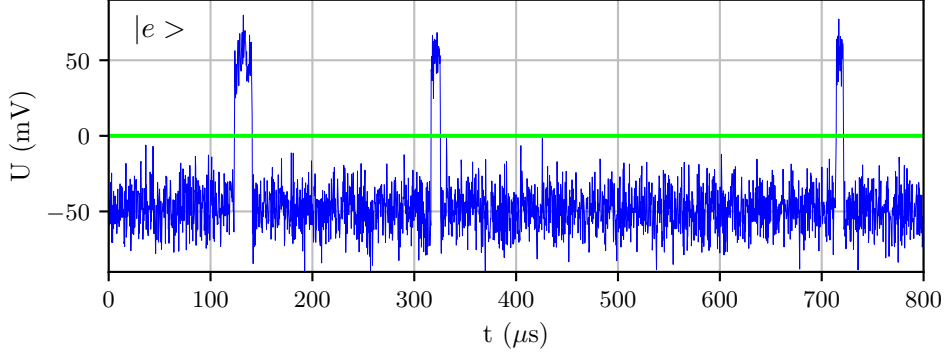


Figure 54: Long jumtrace with even higher separation due to high readout power $n \approx 190$. Averaging time and JPC gain as above $t_{avg} = 320$ ns and 15 dB. Three transitions to the excited state appear in the depicted section. Dwell times in $|e\rangle$ are on the order of tens of μs .

and $|e\rangle$, depending on whether it ends up below or above the separation line. Two sudden transitions (quantum jumps) are visible in the trace. A presumably thermal excitation is followed by a decay back into the ground state. A second example of a quantum jump trace is depicted in fig. 54. A longer trace of $800 \mu\text{s}$ was measured at high power $n \approx 190$. Three quantum jumps back and forth to the excited state occur in the plotted section. Although the separation is large in comparison to the data variance, there is still a finite probability of an assignment error. Following [57], the miscount probability can be calculated as the probability of actual ground state results to end up above the separation line

$$p_{\text{mis}} = \int_{d_{ge}/2}^{-\infty} \frac{1}{\sigma\sqrt{2\pi}} e^{x/(2\sigma^2)} dx. \quad (114)$$

Variance σ and separation $d_{ge} = \sqrt{(I_g - I_e)^2 + (Q_g - Q_e)^2}$ are taken from the fitted Gaussians. With my assumption of equal widths the miscount probability is the same for ground and excited state. The fidelity is simply defined as

$$F = 1 - p_{\text{mis}}. \quad (115)$$

A fidelity of one corresponds to a perfectly faithful measurement, whereas a $F = 0$ corresponds to a completely random measurement that extracts no information. Fig. 55 illustrates the integration scheme of the miscount probability (left) and calculated values for various probe powers (right). The power sweep is derived from the same data as shown in fig. 47. A probe power of 6 photons is sufficient to reach $p_{\text{mis}} \leq 1\%$. The power dependence of p_{mis} will become important when analysing the statistics of the quantum jumps

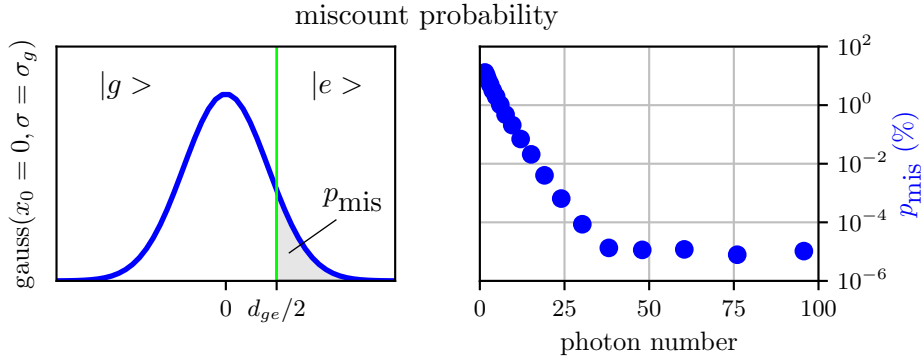


Figure 55: **Left:** The miscount probability p_{mis} describes the probability of a measurement result to end up on the wrong side of the separation line. It can be calculated by integrating the Gaussian probability distribution from the position of the separation line to ∞ . **Right:** Power sweep for p_{mis} measured at $t_{\text{avg}} = 640$ ns and $G_{\text{JPC}} = 15$ dB.

in the next section.

5.8.2 Qubit Lifetime Estimation

Investigating the distribution of the quantum jumps, allows to give an estimate of the qubit lifetime T_1 . Looking at the high power measurement shown in fig. 54, typical durations of excited state events are on the order of tens of μs . Ground state events can easily extend up to several hundreds of μs . The full trace containing 1300000 data points was filtered numerically, extracting the event durations for ground and excited state. Events of an extent of only time step (320 ns) are considered noise and neglected in the filtering, corresponding to a rejection count $N_{\text{rej}} = 1$. The distribution of the event durations are depicted in fig. 56 in the form of histograms. Its exponential shape reflects the probability of events of a certain extent. Fitting the data with an exponential model $\sim \exp(-t/T)$ results in a qubit lifetime of $T_1 = 1/\gamma_1 = 6.1(3) \mu\text{s}$. The typical duration of a ground state event is $T_{\uparrow} = 1/\gamma_{\uparrow} = 257(8) \mu\text{s}$. The ratio $T_1/T_{\uparrow} \approx 2.3\%$ agrees well with the calculated temperature (compare population distributions listed in tab. 7).

Even longer lifetimes are observed in jump traces measured with lower IQ probe power. Fig. 57 (left) shows a T_1 power sweep, as derived from fitting the histograms of jump traces with various probe powers. The results of this method should be treated with caution. Lower IQ probe powers result in a reduced separation (compare fig. 47) and a higher chance of falsely assigned noise events distorting the event statistics. At low probe powers, the histograms become top-heavy with a large number of noise events with a duration of one timestep,



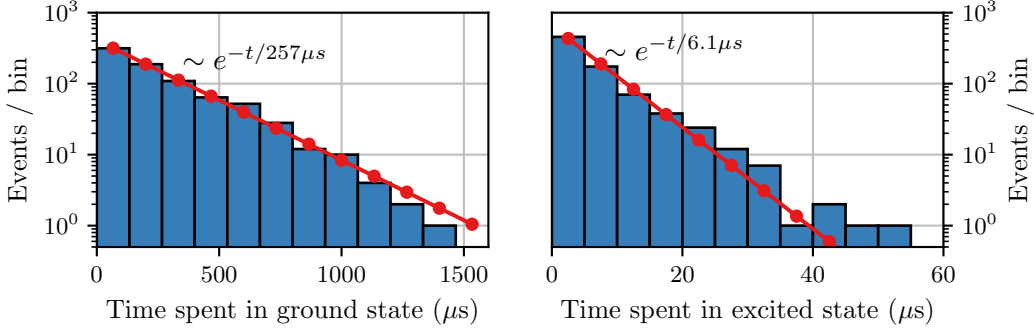


Figure 56: Histograms of the event durations for ground (**left**) and excited state (**right**.) Derived from the full high power jump trace measured with $n_p = 190$ photons. An excerpt of that trace is shown in fig. 54. Exponential fits (red) allow to estimate the excited and ground state lifetimes $T_1 \approx 6.1(3) \mu s$ and $1/\gamma_{\uparrow} = 257(8) \mu s$.

deviating strongly from the expected exponential distribution. This problem is addressed by using a power dependent rejection count N_{rej} when filtering the jump traces. For each probe power, N_{rej} is chosen such, that the resulting histogram follows an exponential shape while still rejecting as few events as possible. Rejection counts N_{rej} start at 3 and quickly drop to 0 following roughly the distribution of the miscount probability plotted in fig. 55. The qubit lifetime is stable up to a readout power of approximately 20 photons, before dropping abruptly to about half its value. It is clearly Purcell-limited as it never exceeds $1/\gamma_P = 18.9(1) \mu s$. The complementary data showing the ‘ground state lifetime’ T_{\uparrow} is shown in the appendix in fig. 61. The low power lifetime of about $T_1 = 16 \mu s$ agrees well with $T_1^{\text{ref}} = 18 \mu s$ as determined in an independent measurement on the same transmon qubit. T_1^{ref} is measured by exciting the qubit with a $\pi/2$ pulse followed by a readout pulse after a varying delay time [34]. The measurement was done by group member Oscar Gargiulo.

The right panel of fig. 57 shows the relative occupations of the $|e\rangle$ and $(|f\rangle + \dots)$ state results. At probe powers of more than ~ 5 photons, non thermal distributions, where the f state population significantly exceeds the e state population are observed (compare sec. 5.6.3). Together with the power dependent T_1 decrease, this indicates an increasing impact of the dispersive IQ readout scheme on the measured system. Both effects are observed at lower powers than anticipated, as the dispersive approximation is expected to be valid up to a power of $n_{\text{crit}} \approx 60$ photons. The temperatures, that are derived from the distribution of the $|g\rangle$, $|e\rangle$ and $(|f\rangle + \dots)$ state population is only slightly affected by the unexpectedly high counts of f state results. The reason for this is, that the temperature

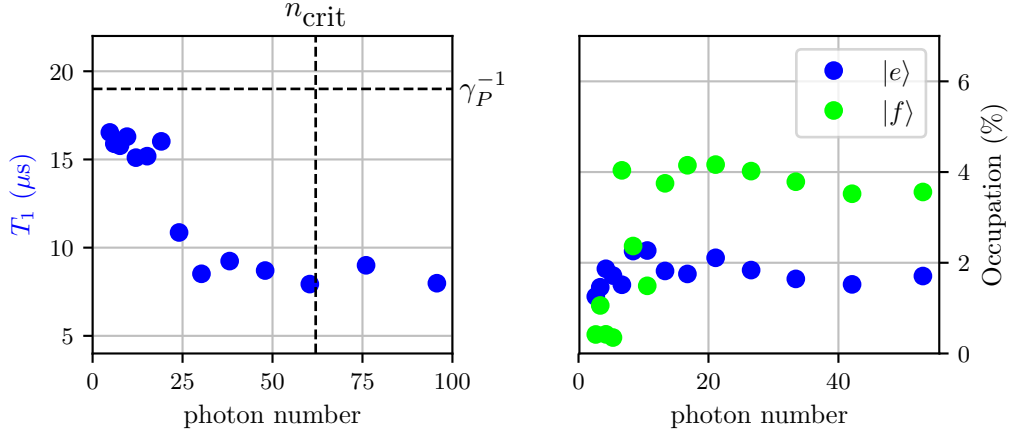


Figure 57: T_1 power sweep and relative e and f state population illustrating the breakdown of ‘QNDness’. **Left:** T_1 is derived from quantum jump traces measured at f_2 with $t_{\text{avg}} = 640$ ns and $G_{\text{JPC}} = 15$ dB. An abrupt drop in T_1 is observed at about 20 photons. The observed lifetimes appear to be Purcell-limited with $1/\gamma_P = 18.9(1)$ μs . **Right:** Relative $|e\rangle$ and $|f\rangle$ state populations are extracted from IQ measurements taken at f_3 with $t_{\text{avg}} = 1280$ ns and $G_{\text{JPC}} = 15$ dB. Statistical uncertainties are smaller than the size of the points. Stronger population of the ($f + \dots$) state compared to e for probe powers exceeding ~ 10 photons is surprising. Note that the relative population of the excited state stays roughly constant, in agreement with the observed power independence of the temperature (compare fig. 48).

which minimizes the ‘cost function’ (sum of weighted squared residuals eq. 112) of the fitting routine is for the largest part defined by the ratio between ground and excited state results. This ratio being roughly constant at 2% leads to the observed power independent transmon temperature, regardless of the relative population of $|f\rangle$ and higher states. A less thermal distribution is solely reflected in a slight decrease of the R^2 of the temperature calculation. Considering this obvious interaction of the measurement beam with the qubit-cavity-system, the ‘QNDness’ of the continuous dispersive readout scheme appears to be already compromised at powers as low as ~ 5 photons, corresponding to only 10% of n_{crit} . A similar behaviour in a pulsed readout scheme still needs to be investigated. A raw IQ data set of such a non-thermal measurement is presented in fig. 59 of the appendix.

5.9 Summary

In this chapter, the realization of the continuous dispersive readout scheme is demonstrated. Experimental results with three clearly resolved transmon states are presented. IQ con-



trast, data quality and temperature are evaluated for various JPC gains, probe powers and averaging times. As expected, a higher readout power was found to increase the separation, while causing only a slight increase in the disk width due to the amplified quantum fluctuations and JPC noise. The temperature is independent of the readout power, as the ratio of ground and excited state population stays constant. Deviation from the Gaussian shapes (‘squeezing’) caused by saturation of the JPC was observed at a probe power of ~ 20 photons at a JPC gain of 18 dB. When distinguishing three transmon states, non-thermal population distributions with the e state population exceeding the f state population are observed for readout powers > 5 photons. This surprising result suggests a breakdown of the ‘QNDness’ of the continuous dispersive measurement at powers far below the critical photon number $n_{\text{crit}} \approx 60$. This assumption is confirmed further by looking at the temporal evolution of the measured transmon state. With the use of the JPC, it is possible to measure the qubit faster than its internal transition rates. Two examples of quantum jump traces are shown. Analysis of the traces allows to estimate the qubit lifetime T_1 . For probe powers exceeding 20 photons, the observed lifetime quickly decreases, again indicating that the measurement is only QND for powers below 5 to 10 photons. The actual T_1 values derived from binning the quantum jump traces should be treated with care, as a power dependent pre-selection (rejecting noise events, see sec. 5.8.2) is used when evaluating the jump traces. An accurate method to determine the qubit lifetime would be a T_1 experiment using pulsed probe signals.

6 Conclusion & Outlook

The main goal of this thesis was to improve the SNR of the measurement chain by integrating a Josephson parametric amplifier (**JPC**) into the existing experimental setup. The functionality of the amplifier was tested thoroughly in various configurations, confirming its specifications. A shift of the amplification range towards lower frequencies by about 100 MHz was observed after a year in the cryostat and about 20 cooling cycles. Re-measuring the fluxmaps of both the JPC’s signal and idler resonator at least once per year seems advisable. Even though the JPC is not always easy to use, it definitely pays off. An SNR increase of up to 12 dB was observed in the optimal operation range $G_{\text{JPC}} = 15$ dB to 20 dB.

The capabilities of the JPC were tested experimentally on a transmon artificial atom strongly coupled to a 3D microwave resonator. After determining the relevant system parameters in spectroscopic measurements, a protocol for dispersive readout using contin-

uous probe signals was developed. With the use of the JPC, the transmon state can be measured faster than the internal transition rates. Quantum jumps are directly visible in the continuously measured traces. In this setup, a 1% ground state detection fidelity was achieved at a readout power of 6 resonator photons, an integration time of $t_{avg} = 640$ ns and a low JPC gain of $G_{JPC} = 15$ dB (no accepted squeezing). The contrast was limited by the large phase shift of 264° between ground and excited state results, which was close to a full circle. Even though we succeeded in engineering the system close to the optimal readout condition $\kappa = \chi_e$, the contrast was compromised by a lower than anticipated internal quality factor. Improved contrast would allow for measurements at even lower readout powers or with even shorter averaging times. The quantum jump traces even allow to examine the temporal evolution of the system. An unconventional and simple method of deriving an estimate about the qubit lifetime T_1 is presented in this thesis. Evaluation of the statistical distribution of the quantum jump events results in $T_1 = 16 \mu s$ at low powers. The lifetime in the investigated setup is clearly Purcell-limited as $1/\gamma_P = 19 \mu s$.

The next step in the development of the continuous readout scheme presented in this thesis will be to move from continuous probe signals to pulsed signals. Pulsed measurements populate the cavity only for a short time. Integrating the signal leaking out of the cavity (including ring-up and decay) allows for high contrast readout with minimal back action on the system [58] [59]. Being able to perform a series of high fidelity manipulation and readout operations is a indispensable prerequisite for succesfull quantum simulation and computation experiments [5].



Appendices

A Additional Plots

A.1 Logarithmic projected histograms

In comparison to fig. 45 of the main text, fig. 58 shows a fitted IQ data set with a logarithmic scale of the projected histograms. The individual Gaussian peaks are indicated with the usual color coding where (g, e, f) correspond to (red, blue, green). The actual fitting function (sum of the three Gaussians with equal width) is drawn in orange. Both the visual agreement and the high R^2 of 0.998 suggest that the data is described well by the Gaussian model. (as long as the JPC is not saturated).

A.2 Non thermal transmon population at high readout powers

At readout powers above roughly 20 photons, non thermal distributions of the state population have been observed. A typical example of such a measurement is shown in fig. 59. The f state population clearly exceeds the e state population. The presumed reason is the breakdown of the QND interaction between drive and measured system. Calculating the temperature via the minimizing routine discussed in sec. 5.6.3 still converges reasonably well, resulting in $T = 84(1)$ K with an R^2 of 0.998.

A.3 Reject counts for T_1 power sweep

As discussed in sec. 5.8.2, the qubit lifetime T_1 was determined for various IQ probe powers by binning the quantum jump traces into histograms. However, in the low power traces, the ground and excited state are not separated that well and the probability of falsely assigned events is higher. In order to compensate for those ‘noise events’, quantum jumps shorter than $N_{rej} = 1, 2, 3$ timesteps have been ignored when computing the histograms. The rejection counts used for each power are plotted in fig. 60. They roughly follow the miscount probability shown in fig. 55 of the main text.

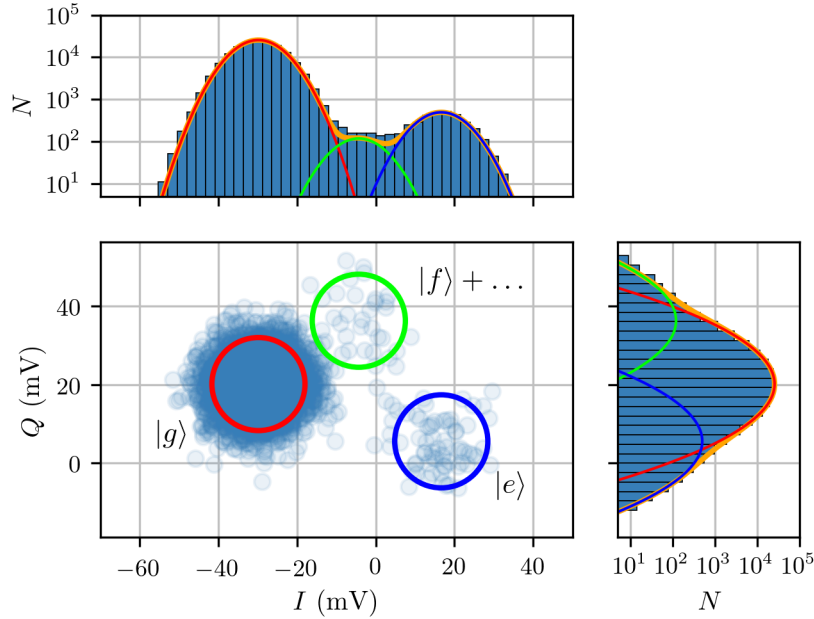


Figure 58: Same plot as in fig. 45, but with logarithmic histograms to allow an easier visual comparison of fit and data. IQ-measurement with $n_p = 4$ probe photons, $t_{avg} = 1280$ ns, 162000 points and $G_{JPC} = 12$ dB. The scatter plot shows the first 10000 data points with a transparency of 0.1. The circles represent 4σ (diameter) of the Gaussian profiles obtained by the fit.

A.4 Ground state lifetimes vs. power

For completeness, fig. 61 depicts the inverse excitation rate (or ‘ground state lifetime’) derived from quantum jump traces with various powers as discussed in sec. 5.8.2.

A.5 Resolving four states in the IQ plane

A high-power IQ measurement with long integration time reveals the signature of the transmon’s third excited state $|h\rangle$, see fig. 62. The measurement was conducted at the three state probe frequency f_3 , resulting in a small phase shift between f and h . The fourth disk is clearly visible in the data, along with a large number of intermediate events indicating jumps during the IQ integration time.



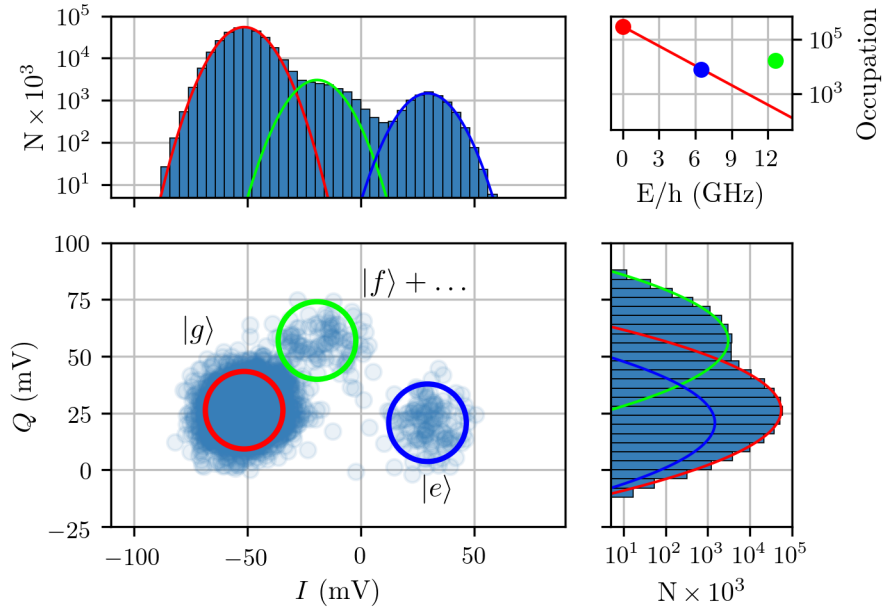


Figure 59: Example of non-thermal state population for high IQ-probe powers $n_p \gg n_{\text{crit}}$. Same plot as in fig. 45, but with a readout power of ~ 70 photons and $t_{\text{avg}} = 640$ ns. State occupation (volume of the fitted Gaussians) vs. energy is shown in the top right graph. The parameters for the exponential fit (red) are calculated with the usual minimizing scheme, taking into account the contributions of the higher transmon states.

A.6 Linear and logarithmic plot of squeezed data

Fig. 63 shows the 2D histogram of a set of IQ data in linear and logarithmic depiction. The disks (attraction centres) in the IQ plane are slightly squeezed due to the comparatively high readout power and JPC gain. The graph compares directly to fig. 44 of the main text which displays a measurement with little to no squeezing.

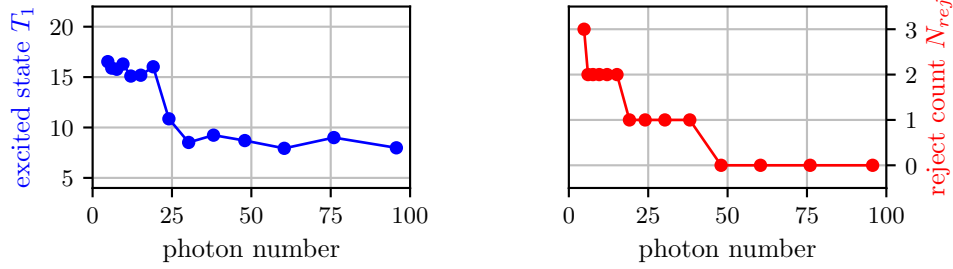


Figure 60: T_1 power sweep (same data as shown in the main text) and rejection counts N_{rej} used for filtering the quantum jump histograms. The N_{rej} roughly follow the miscount probability and are chosen such, that the resulting histograms agree with the expected exponential decrease of the probability of longer events.

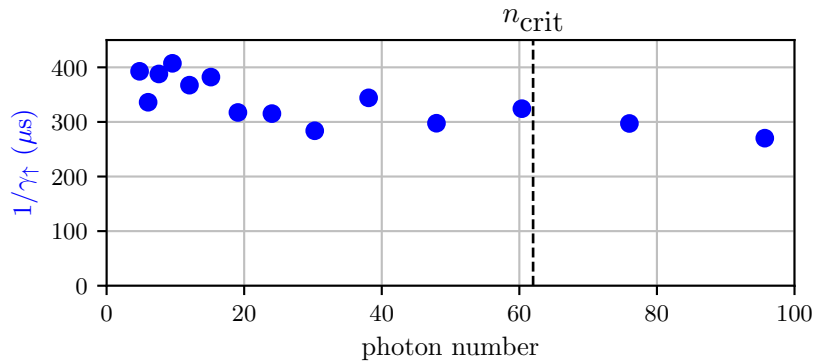


Figure 61: Power sweep of the ground state decay time $1/\gamma_{\uparrow}$. A slight drop at an IQ probe power of ~ 20 photons appears, in agreement with the observed drop in T_1 at the same photon number.



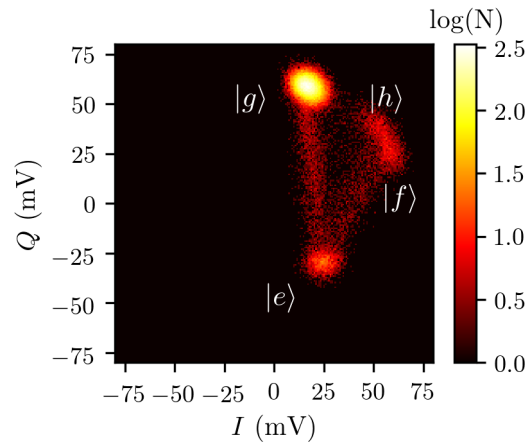


Figure 62: IQ measurement while strongly driving both the transmons $g \leftrightarrow e$ and the $e \leftrightarrow f$ transitions. Recorded at f_3 with a power of 10 photons with a high JPC gain of 25 dB. Averaging times of $t_{avg} = 1280$ ns allow to have a glance at the third excited state. A fit of four Gaussian profiles did not converge due to the large amount of intermediate events in between the disks.

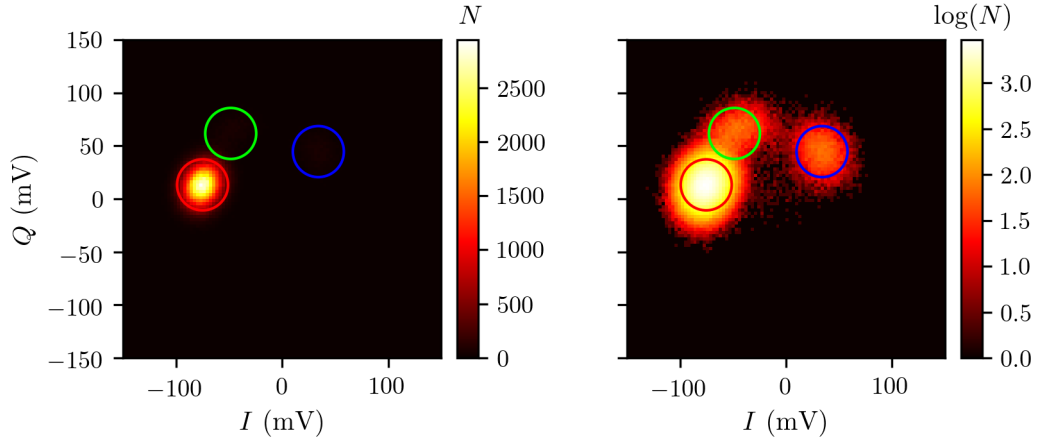


Figure 63: Another comparison of linear and logarithmic IQ histograms with 100×100 bins. The disks show a slight squeezing due to high gain of $G_{\text{JPC}} = 18$ dB and readout power of 21. Measured at f_3 with $t_{\text{avg}} = 320$ ns. In the logarithmic depiction, the squeezing appears to be more drastic.

A.7 JPC SN010 Fluxmaps

Fig. 64 shows the reference ‘fluxmaps’ for signal and idler resonator of the JPC SN010. Note that the depicted resonances are suspected to shift towards lower frequencies due to Junction aging. Still, this image provides a valuable starting guess for the pump frequency when working with the JPC SN010.

A.8 Flip book full image

Fig. 65 shows the full graph of the flip book images plotted at the bottom right corner of the odd pages of this thesis. Ground and excited state results are drawn in black and grey respectively. Scrolling through the flip book gives an intuitive idea about the continuous monitoring of the transmons quantum state. Each page adds a new measurement record corresponding to one timestep $t_{\text{avg}} = 160$ ns. The final image contains 51 points taken in a total monitoring time of roughly $8 \mu\text{s}$. A quantum jump occurs in chapter 4 after approximately $4 \mu\text{s}$. Finding the exact page is left to the reader.



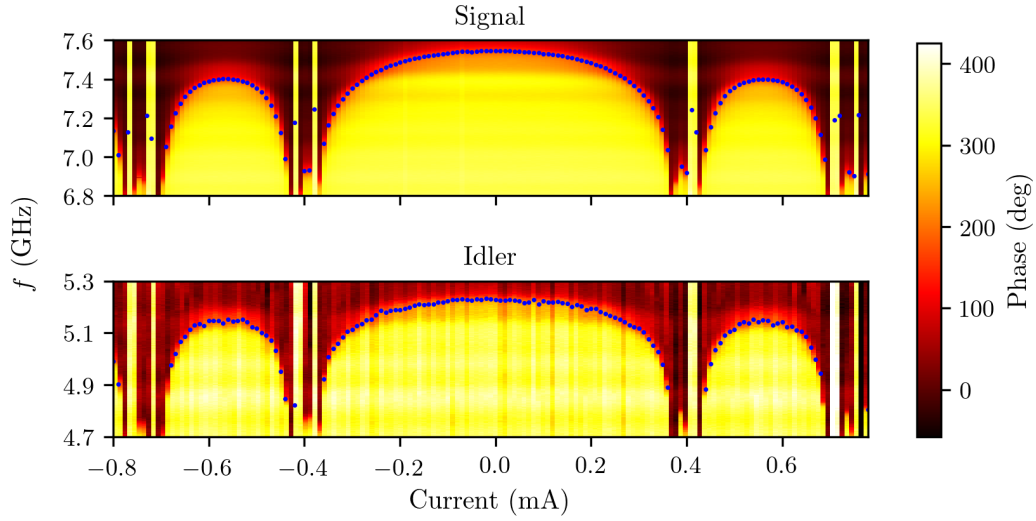


Figure 64: Signal and idler reference fluxmaps for the **JPC SN010** as provided by the manufacturer [52]. Blue dots indicate the position of the resonance frequencies. Amplification is possible only at the sides of the large lobes. In the experiment, the current axis is typically offset (due to trapped flux) and scaled differently.

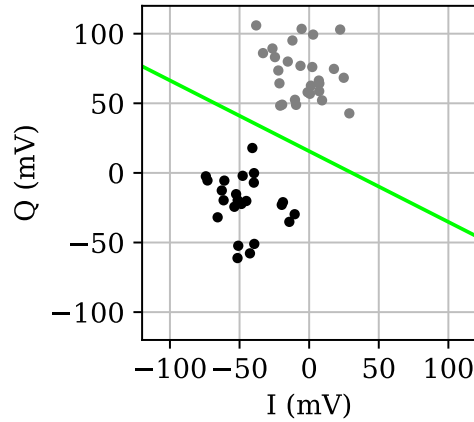


Figure 65: Full image of the flip book from the right bottom of the even pages. Measured at the two-state probe frequency f_2 at high probe power of $n_p = 190$ resonator photons with $t_{avg} = 160$ ns and $G_{JPC} = 18$ dB. The squeezing is not evident in the selected sample showing just 51 data points. Separation line calculated from the full data set as described in sec. 5.8.

B JPC Pictures

A photograph of the assembled JPC SN010 without protection shield is shown in fig. 66. The housing of the Josephson ring modulator (JRM) is seen at the bottom. Two hybrids ensure the correct addressing of the JRM modes as discussed in sec. 4.2. They are connected to the main chip via four two inch minibend rf cables. When the mu metal shield of the JPC is closed, only the main ports ‘signal’ ‘idler’ and ‘pump’ are accessible for the user. They are labelled accordingly (see top part of left image). The coil which is providing the magnetic flux for the tunability of the amplifier is also obscured by the housing on the bottom. The black coated wire (‘DC coil bias’) connects the coil to an outside DC source. As the connection to the coil is quite fragile, the wire is stabilized with adhesive aluminium tape (right image). Nevertheless, any stress on that cable should be strictly avoided as any damage would critically compromise the functionality of the JPC. Fixing a damaged cable isolation close to the coil inside the chip housing involves the risk of opening the protective enclosure.

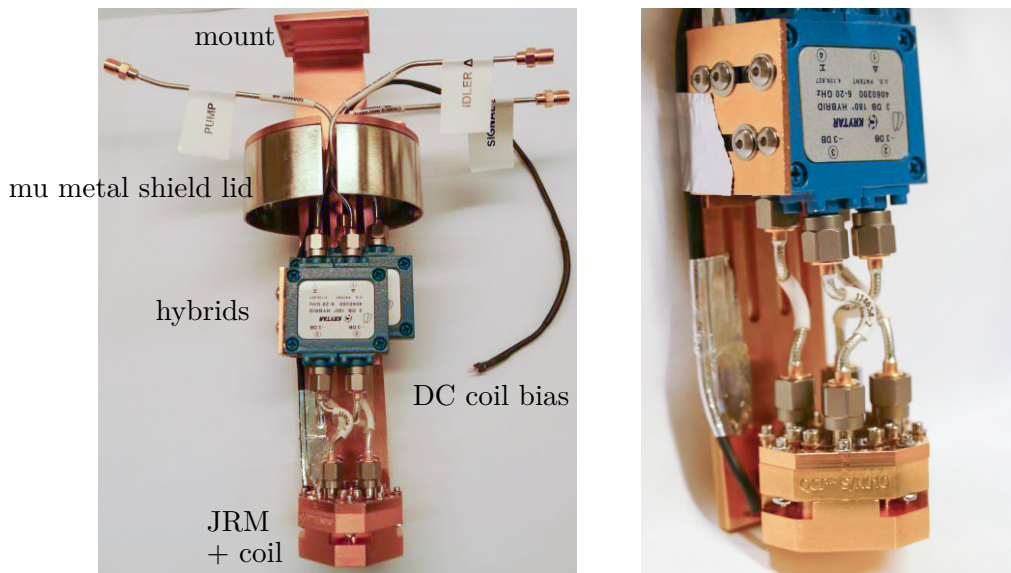


Figure 66: Photograph of the JPC SN010 without mu metal shield. Full view (**left**) and enlarged section of the internal wiring (**right**). Description in the text.



References

- [1] M. H. Devoret and R. J. Schoelkopf. “Superconducting Circuits for Quantum Information: An Outlook”. In: *Science* 339.6124 (2013), pp. 1169–1174.
- [2] Lucas Lamata et al. “Digital-analog quantum simulations with superconducting circuits”. In: *Advances in Physics: X* 3 (2018), p. 1457981.
- [3] Y. Nakamura, Yu A. Pashkin, and J. S. Tsai. “Coherent control of macroscopic quantum states in a single-Cooper-pair box”. In: *Nature* 398 (1999), pp. 786–788.
- [4] Hanhee Paik et al. “Observation of High Coherence in Josephson Junction Qubits Measured in a Three-Dimensional Circuit QED Architecture”. In: *Phys. Rev. Lett.* 107 (24 2011), p. 240501.
- [5] G Wendin. “Quantum information processing with superconducting circuits: a review”. In: *Reports on Progress in Physics* 80.10 (2017), p. 106001.
- [6] D. I. Schuster et al. “ac Stark Shift and Dephasing of a Superconducting Qubit Strongly Coupled to a Cavity Field”. In: *Phys. Rev. Lett.* 94 (12 2005), p. 123602.
- [7] A. Wallraff et al. “Strong coupling of a single photon to a superconducting qubit using circuit quantum electrodynamics”. In: *Nature* 431 (2004), pp. 162–167.
- [8] Baleegh Abdo et al. “Josephson amplifier for qubit readout”. In: *Applied Physics Letters* 99.16 (2011), p. 162506.
- [9] Philip Krantz et al. “Single-shot read-out of a superconducting qubit using a Josephson parametric oscillator”. In: *Nature Communications* 7 (2016).
- [10] Z. R. Lin et al. “Single-shot readout of a superconducting flux qubit with a flux-driven Josephson parametric amplifier”. In: *Applied Physics Letters* 103.13 (2013), p. 132602.
- [11] R. Vijay, D. H. Slichter, and I. Siddiqi. “Observation of Quantum Jumps in a Superconducting Artificial Atom”. In: *Phys. Rev. Lett.* 106 (11 2011), p. 110502.
- [12] E. M. Purcell. “Proceedings of the American Physical Society”. In: *Phys. Rev.* 69 (11-12 1946), pp. 674–674.
- [13] Daniel Kleppner. “Inhibited Spontaneous Emission”. In: *Phys. Rev. Lett.* 47 (4 1981), pp. 233–236.
- [14] Serge Haroche and Daniel Kleppner. “Cavity Quantum Electrodynamics”. In: *Physics Today* 42.1 (1989), pp. 24–30.
- [15] M. Brune et al. “Quantum nondemolition measurement of small photon numbers by Rydberg-atom phase-sensitive detection”. In: *Phys. Rev. Lett.* 65 (8 1990), pp. 976–979.

-
- [16] D.F. Walls and G.J. Milburn. *Quantum Optics*. Springer Study Edition. Springer Berlin Heidelberg, 2012.
- [17] E. T. Jaynes and F. W. Cummings. “Comparison of quantum and semiclassical radiation theories with application to the beam maser”. In: *Proceedings of the IEEE* 51.1 (1963), pp. 89–109.
- [18] David Isaac Schuster. “Circuit Quantum Electrodynamics”. PhD thesis. Yale University, 2007.
- [19] Romeo Alessandro Bianchetti. “Control and readout of a superconducting artificial atom”. PhD thesis. ETH Zürich, 2010.
- [20] Uri Vool and Michel Devoret. “Introduction to quantum electromagnetic circuits”. In: *International Journal of Circuit Theory and Applications* 45.7 (2016), pp. 897–934.
- [21] R. Gross and A. Marx. *Festkörperphysik*. Oldenbourg Wissenschaftsverlag, 2012.
- [22] B.D. Josephson. “Possible new effects in superconductive tunnelling”. In: *Physics Letters* 1.7 (1962), pp. 251–253.
- [23] C. A. Hamilton et al. “A 24-GHz Josephson array voltage standard”. In: *IEEE Transactions on Instrumentation and Measurement* 40.2 (1991), pp. 301–304.
- [24] Jens Koch et al. “Charge-insensitive qubit design derived from the Cooper pair box”. In: *Phys. Rev. A* 76 (4 2007), p. 042319.
- [25] Matthew James Reagor. “Superconducting Cavities for Circuit Quantum Electrodynamics”. PhD thesis. Yale University, 2015.
- [26] D.M. Pozar. *Microwave Engineering, 4th Edition*. Wiley, 2011.
- [27] T. Brecht et al. “Demonstration of superconducting micromachined cavities”. In: *Applied Physics Letters* 107.19 (2015), p. 192603.
- [28] C. Poole and I. Darwazeh. *Microwave Active Circuit Analysis and Design*. Elsevier Science, 2015.
- [29] Augusting Palacious-Laloy. “Superconducting qubit in a resonator: test of the Leggett-Garg inequality and single-shot readout”. PhD thesis. Quantronics Group SPEC - CEA Saclay, 2010.
- [30] Jay Gambetta et al. “Qubit-photon interactions in a cavity: Measurement-induced dephasing and number splitting”. In: *Phys. Rev. A* 74 (4 2006), p. 042318.
- [31] D. I. Schuster et al. “Resolving photon number states in a superconducting circuit”. In: *Nature* 445 (2007), pp. 515–518.
- [32] Maxime Boissonneault, J. M. Gambetta, and Alexandre Blais. “Improved Superconducting Qubit Readout by Qubit-Induced Nonlinearities”. In: *Phys. Rev. Lett.* 105 (10 2010), p. 100504.



- [33] Jay Gambetta et al. “Quantum trajectory approach to circuit QED: Quantum jumps and the Zeno effect”. In: *Phys. Rev. A* 77 (1 2008), p. 012112.
- [34] G. Ithier et al. “Decoherence in a superconducting quantum bit circuit”. In: *Phys. Rev. B* 72 (13 2005), p. 134519.
- [35] R. M. Lutchyn, L. I. Glazman, and A. I. Larkin. “Kinetics of the superconducting charge qubit in the presence of a quasiparticle”. In: *Phys. Rev. B* 74 (6 2006), p. 064515.
- [36] Eyob A. Sete, John M. Martinis, and Alexander N. Korotkov. “Quantum theory of a bandpass Purcell filter for qubit readout”. In: *Phys. Rev. A* 92 (1 2015), p. 012325.
- [37] David Zöpfl. “Characterisation of stripline resonators in a waveguide”. MA thesis. Universität Innsbruck, 2017.
- [38] A. Bruno et al. “Reducing intrinsic loss in superconducting resonators by surface treatment and deep etching of silicon substrates”. In: *Applied Physics Letters* 106.18 (2015), p. 182601.
- [39] A. A. Houck et al. “Controlling the Spontaneous Emission of a Superconducting Transmon Qubit”. In: *Phys. Rev. Lett.* 101 (8 2008), p. 080502.
- [40] Rajamani Vijayaraghavan. “Josephson Bifurcation Amplifier: Amplifying quantum signals using a dynamical bifurcation”. PhD thesis. Yale University, 2008.
- [41] Flavius Dietrich Octavian Schackert. “A Practical Quantum-Limited Parametric Amplifier Based on the Josephson Ring Modulator”. PhD thesis. Yale University, 2013.
- [42] N. Bergeal et al. “Analog information processing at the quantum limit with a Josephson ring modulator”. In: *Nature Physics* 6 (2010). Article, pp. 296–302.
- [43] Baleegh Abdo, Archana Kamal, and Michel Devoret. “Nondegenerate three-wave mixing with the Josephson ring modulator”. In: *Phys. Rev. B* 87 (1 2013), p. 014508.
- [44] N. Roch et al. “Widely Tunable, Nondegenerate Three-Wave Mixing Microwave Device Operating near the Quantum Limit”. In: *Phys. Rev. Lett.* 108 (14 2012), p. 147701.
- [45] Daniel A. Steck. *Quantum and Atom Optics*. 2017. URL: <http://steck.us/teaching>.
- [46] C. Gardiner and P. Zoller. *Quantum Noise: A Handbook of Markovian and Non-Markovian Quantum Stochastic Methods with Applications to Quantum Optics*. Springer, 2004.
- [47] Ananda Roy and Michel Devoret. “Introduction to parametric amplification of quantum signals with Josephson circuits”. In: *Comptes Rendus Physique* 17.7 (2016), pp. 740–755.
- [48] P.D. Drummond, Z. Ficek, and Z. Spicsek. *Quantum Squeezing*. Physics and Astronomy Online Library. Springer, 2004.

-
- [49] Carlton M. Caves. “Quantum limits on noise in linear amplifiers”. In: *Phys. Rev. D* 26 (8 1982), pp. 1817–1839.
- [50] N. Bergeal et al. “Phase-preserving amplification near the quantum limit with a Josephson ring modulator”. In: *Nature* 465 (2010), pp. 64–68.
- [51] Quantum Circuits, Inc. *JPC SN004 Users Guide*. <http://quantumcircuits.com>. Accessed 20-May-2018.
- [52] Quantum Circuits, Inc. *JPC SN010 Users Guide*. <http://quantumcircuits.com>. Accessed 20-May-2018.
- [53] G. Liu et al. “Josephson parametric converter saturation and higher order effects”. In: *Applied Physics Letters* 111.20 (2017), p. 202603.
- [54] Teledyne SP devices. *SDR14 DAC Datasheet*. <https://spdevices.com/documents/datasheets/8-sdr14-datasheet/file>. Accessed 14-June-2018.
- [55] W. Feller. *An Introduction to Probability Theory and Its Applications, Ed. 3*. Wiley series in probability and mathematical statistics. Wiley India Pvt. Limited, 2008.
- [56] Peter H. Richter. “Estimating Errors in Least-Squares Fitting”. In: 1995.
- [57] Jay Gambetta et al. “Protocols for optimal readout of qubits using a continuous quantum nondemolition measurement”. In: *Phys. Rev. A* 76 (1 2007), p. 012325.
- [58] I. Siddiqi et al. “Dispersive measurements of superconducting qubit coherence with a fast latching readout”. In: *Phys. Rev. B* 73 (5 2006), p. 054510.
- [59] Francois Mallet et al. “Single-shot qubit readout in circuit quantum electrodynamics”. In: *Nature Physics* 5 (2009), pp. 791 –795.

